First-principles design of magnetic anisotropy in nanostructures by electric-field, strain, and metal alloying

メタデータ	言語: eng
	出版者:
	公開日: 2020-01-08
	キーワード (Ja):
	キーワード (En):
	作成者:
	メールアドレス:
	所属:
URL	http://hdl.handle.net/2297/00056468

First-principles design of magnetic anisotropy in nanostructures by electric-field, strain, and metal alloying

電界、ひずみ、合金化によるナノ構造磁気異方性の第一原理設計

A thesis submitted in fulfilment of the requirements
for the degree of Doctoral of Science

Author:

Indra Pardede

1624012010

Supervisor:

Prof. Tatsuki Oda

Division of Mathematical and Physical Science

Graduate School of Natural Science and Technology

Kanazawa University

June 2019

KANAZAWA UNIVERSITY

Abstract

Division of Mathematical and Physical Science
Graduate School of Natural Science and Technology

Doctoral of Science

**First-principles design of magnetic anisotropy in nanostructures by
electric-field, strain, and metal alloying**

by Indra Pardede

Magnetic anistropy energy (MAE) is one of the important property in the field of
magnetism, which determines the prefered orientation of the magnetization. In the
nanostructure scale, it has been succesfully controlled by magnetic field or current.
In a basis of that concept, the application in electronic device also can be realized,
such as magnetic random acces memory (MRAM). The magnetization switching
corresponds to the switching of binary "0" and "1". Recently, a new mechanism to
control MAE by using electric field (EF) has been proposed. This new concept has
advantages such as lower energy consumption. However, up to now, this research
field still remaining a great challenge. In the real application, materials with high
EF coefficient are reqired. To fulfill this requirement, a comphrehensive study to
investigate the origin of MAE, mechanism of EF control MAE and search for the
new materials is strongly needed.

In this dissertation, the first topic keep focused on the investigation of the al-
loying, strain, and EF effect to the MAE in the system which contains Fe/MgO
interface with Cr underlayer in the basis of a first-principles electronic structure
calculations. In the calculations, we considered two kinds of contribution to MAE,
namely magnetocrystalline anisotropy energy (MCAE) originating from spin-orbit
coupling (SOC) and shape magnetic anisotropy energy (SMAE) originating from
magnetic dipole-diole interaction (MDI). The MCAE was calculated using the
methods of the total energy (TE) and grand canonical force theorem (GCFT). In
the GCFT scheme, we performed the atom-resolved and k-resolved contributions
to the MCAE. For the SMAE contribution, we used a continuum approach (CA),

discrete approach (DA), and spin density approach (SDA). In the SDA, we investigated components from atomic multipole spin-density, such as the quadrupole component.

We found that alloying Fe/Cr can promote the perpendicular MAE (PMAE) in the Cr/Fe/MgO structure. Furthermore, different alloying condition can lead to an opposite sign in the EF coefficient (γ). The alloying effect can induce a substantial rearrangement in the electronic structure due to proximity effect of Fe and Cr. The proximity effect is associated with Cr-Fe hybridization and electrons transfer from Cr to Fe atoms due to a smaller electronegativity of Cr. Consequently, the number of $3d$ electrons on the Fe at Fe/MgO interface may increase. By introducing strain effect in the alloying system, the enhancement of MAE and γ were achieved. From the atom-resolved MCAE calculation, we found that the positive contribution to the MCAE mainly comes from Fe at Fe/MgO interface. From k-resolved MCAE calculation, we found that positive and negative contributions are observed only at certain regions in the two dimensional first Brillouin zone. That contribution can be related to the certain pair coupling of states above and below the Fermi energy by considering the second-order perturbation theory.

The second topic studied was an investigation of SMAE in the ferromagetic slabs Fe/MgO and antiferromagnetic MnX with (X: Pt, Ir, Pd, Ni) L1$_0$ structure. We found that a quadrupole component of Fe atomic spin density suppresses SMAE in the ferromagnetic slabs with Fe/MgO interface. In the antiferromagnetic MnPt slabs, which have a perpendicular favor originating from the crystalline magnetic dipole interaction, a surface effect at the Mn edge appears as an enhancement of SMAE.

Acknowledgements

Contents

List of Figures

List of Tables

Chapter 1

Introduction

1.1 Research Background and Motivation

Magnetic anisotropy (MA) is one of the important properties of magnetic materials. MA quantifies a preferred orientation of magnetization i.e either perpendicular-to-plane or in-plane. Experimentally, MA is determined from the information provided by a field-dependent measurement along two orthogonals directions of magnetic field relative to the sample. In bulk materials, MA tends to be relatively small, but it can markedly change in thin film or multilayer. This is due a the present of symmetry breaking elements such as surfaces and interfaces [5].

Microscopically, there are two main origins of MA. The first one is magnetic dipolar interaction. Due to its property of long range, the dipolar interaction generally results in shape-dependent contribution to the anisotropy, which is of particular importance in thin films and is largely responsible for an in-plane magnetization that is usually observed. This kind of origin can not explain a perpendicular MA (PMA). The second one is spin-orbit interaction. This origin can be interpreted as a coupling between the electron spin and the magnetic field created by its own orbital motion around the nucleus. As the orbital motion itself is directly coupled to the lattice via electric potential of the ion (nucleus), this term provides a contribution to a magnetocrystalline anisotropy (MCAE).

Technology to grow a thin film of nanostructure has lead to materials with novel magnetic properties. At a nanoscale region, control of magnetization direction by magnetic field was demonstrated. By controlling magnetization direction in the

thin film, a large change in the resistance was observed. This discovery is called giant magnetoresistance (GMR) invented by Albert Fert [6] and Peter Grünberg [7], which was awarded with the Nobel prize for physics in 2007. Due to the discovery, a real application has been made as a magnetic storage hard disk drive (HDD) [8, 9]. The binary information "0" and "1" is recorded on the two opposite orientations of the magnetization.

The stability of written information in HDD is determined by energy barrier ΔE ($\Delta E = K_u V$), where K_u is anisotropy energy and V is volume. Energy barrier ΔE should be high enough to overcome thermal fluctuation ($k_B T$). For example, typical HDD for 10-years retention, $\Delta E = K_u V > 54 k_B T$ must be fullfilled [10]. The next generation in term of storing data by magnetism is using solid state memories known as magnetic random access memory (MRAM). It start by observed of tunnelling magnetoresistance (TMR) phenomenon in magnetic tunnel junction (MTJ) at room temperature [11, 12] which was originally discovered for the first time by Julliere in 1975 [13]. Later, it became a kicked off new and ongoing research on TMR, followed by result in giant TMR MgO-based MTJ [14–17]. A MTJ consists of a thin insulating layer (tunnel barrier) sandwiched between two ferromagnetic (FM) metal layers (the electrode). For the insulator layer, materials such as MgO, Al_2O_3, HfO_2, ZrO_2, and $MgAl_2O_4$ are commonly used, while for the FM layer magnetic metals or alloys are used, such as Fe, Co, Ni, Co/Ni, Co/Pd, Fe-Ga, FePt, FePd, CoFe, CoPd, NiFe, and CoFeB. Electron can tunnel through the barrier when a bias voltage is applied between the two ferromagnetic layers. The resistance of MTJ depends on relative alaligment of the magnetic moment of electrodes, which can be control either by pulse of magnetic field or by using spin transfer torque (STT) phenomenon [18–20]. To date, STT-MRAM is already commercialized, for example by Everspin in 2012 with capacity 64-Mbit and in 2016 PMTJ STT-MRAM with capacity 256-Mbit. Even recently, Hynix/Toshiba announced for 4-Gbit STT-MRAM chip, but still in preparation for fully commercial. STT-MRAM has an advantage compared to the first generation MRAM (Stoner-Wolfrath and toggle MRAM) which need large current to generate field-induced magnetization switching.

Nowadays, in STT-MRAM device memory, two critical issues have indeed discussed in detail due to a better performance, i.e critical current and thermal stability. To these issues, later, PMA STT-MRAM became more acceptable in

application. The property of perpendicular STT-MRAM can be discussed as follows. The critical current for switching is define by

$$I_{C0} = \frac{2e}{\hbar} \frac{\alpha A t \mu_0 M_s}{\eta} H_{\text{eff}}, \tag{1.1}$$

where A is the area of magnetic element, e is the electron charge, $\hbar$ is the reduced Planck constant, μ_0 is the vacuum permeability, α is the Gilbert damping coefficient, M_s and t are the saturation magnetization and thickness of storage layer, η is the STT efficiency that depends on the relative orientation of the magnetization (θ=0 or π) and the polarization P, and H_{eff} is the effective switching field. In magnetic junction with out-of plane magnetization, the effective field acting on the storage layer magnetization is define by

$$H_{\text{eff}} = H_{K\perp} - M_s, \tag{1.2}$$

where $H_{K\perp}$ is the perpendicular anisotropy field which pulls the magnetization out of plane. Therefore, the critical switching current can be reduced to much smaller compared to in-plane STT-MRAM [21].

In the past six years, a new scheme for STT-MRAM based on spin-orbit torque (SOT) has been developed [22–26]. The additional heavy metal (HM) such as Pt, Ta, Hf, W, which has a large spin hall angle, will generate a spin polarized current near the HM/FM interface. The spin current will produce a damping torque and induce a magnetization switching [27, 28].

Although remarkable applications have been achieved by controlling magnetization direction, a remaining challenge to reduce a power consumptions still needed. Especially, the recent initiative in internet of things (IoT), artificial intelligence (AI), big data, cloud computing, and advanced safety vehicle (ASV) require a high density, high speed, and low power storage device.

One of solutions to overcome this problem is to use electric field (EF) instead of current. The new type of MRAM controlled by EF called Magnetoelectric (ME)-RAM. In the ME-RAM, EF can be generated by voltage, therefore unwanted energy consumption due to ohmic dissipation of the electric-current flow can be reduced. First observation of the EF control magnetic properties (magnetization saturation and Curie temperature) have been done in ferromagnetic semiconductor [(In,Mn)As] [29, 30]. Later, the voltage control magnetic anisotropy (VCMA)

in a magnetic metal for the first time was reported by Wesheit et al [31]. They demontrated that magnetocrytalline anisotropy of ordered FePt and FePd can be reversibly modified by an applied EF when they immersed in the system in an electrolyte. Inspired by this observation, a large number of experimental works and theoretical investigations on EF control magnetism has been devoted, driving both an urge to understand the mechanism and demand for better peformance. The VCMA effect with a whole all solid state structure was soon reported [32], and extended to full MTJ structure [33–38]. The anisotropy changes were observed around 8.4 μJ/m^2 [32], 15 μJ/m^2 [33], and 50 μJ/m^2 [37]. The mechanism of VCMA here was discussed along a charge-doping induced anisotropy change. Several early theoretical results also proposed possible microscopic origins such as EF induced charge density change on the surface of the film [39], EF induced change in band structure (p orbitals coupled to the d orbital) [40], and modification in the electron filling of each $3d$ orbital by EF, resulting in the accumulated charge at the magnetic layer [41]. Later, another theoretical group also proposed possible origin that includes a modulation of Rasbha parameter [42, 43] and EF induced orbital hybridization changes [44].

The VCMA coefficient (the change of MA respect to the EF) is one of the most important paramater in the design of ME-RAM. For example, in the case of PMA in the range of 0.6 mJ/m^2 to 1.5 mJ/m^2, the required VCMA coeficient is in the range of 600 fJ/Vm to 1500 fJ/Vm. Due to this request, many effort have been devoted from both experiment and theory. Since the EF is screened at the metal/oxide layer, the most effective way to enchance the VCMA coefficient is to make enggineering of the interface. But, in the same time, there are some disadvantages such as reductions in PMA and TMR ratio. Another choices is to use alloying effect [45], underlayer effect [46, 47], and strain effect [48, 49]. Nozaki *etal* showed that such alloying between Fe/Cr in the underlayer region of Cr/Fe/MgO, which possibly happens when an annealing is used during the deposition process, makes a large effect on the quantities of PMA and VCMA coefficient. In this experiment, the PMA and VCMA coefficient reach the values of 2.1 mJ/m^2 and 290 fJ/Vm, respectively [2]. Furthermore, for the $3d$/$5d$-multilayer FM metal, for example, $L1_0$-FePt, the discussion of possible origin of VCMA was extended to a modification of electric quadrupole mechanism [50]. Recently, VCMA in antiferromagnetic (AFM) materials also reported [51, 52]. AFM materials with spin moments in antiparallel configuration produce no stray field and are insensitive to external magnetic field perturbations. Another advantage is a ultrafast dynamics,

which is an ideal property for future candidate memory, storage, and spintronics applications [53].

Although large amount significant works have been done in the area of VCMA, it is still a developing and energetic research topic and with a lot of open questions in fundamental mechanism, performance, and practical application. Further experimental and theoretical investigations may be strongly needed to accelerate the development of ME-RAM based on VCMA.

1.2 Research Objectives

By taking advantage of first-principles approach, associated with a deeper insight and an extended understanding of the underlying mechanisms of magnetic anisotropy and electric field (EF) effect on magnetic anisotropy, this research will focus on two main goals. The first goal of is to investigate the effect of electric field, strain, and alloying to the magnetic anisotropy energy (MAE) in metal/oxide heterostructure. The MAE originating from spin-orbit interaction and magnetic dipolar interaction will be involved in the calculation. The possible origin of the enhancement of MAE and EF control MAE will be discussed with details of the electronic structure. The second goal is to investigate the shape magnetic anisotropy energy (SMAE) in the structure with ferromagnetic and antiferromagnetic spin magnetic configuration. In the evaluation of SMAE, several methods will be used and compared to each other.

1.3 Research Outline

This dissertation is structured as follows:

Chapter 2 contains a theoretical background of magnetic anisotropy energy (MAE). In particular, two main origin of MAE introduced, namely, spin-orbit coupling and magnetic dipole-dipole interaction. The general introduction to density functional theory is briefly discussed. Chapter 3 explains the computational method that we used in the calculation. The detail of MAE and EF effect on MAE calculation will be described. In Chapter 4, the results followed by discussions are reported. It will start by the result and discussion on MAE Cr/Fe/MgO structure. The alloying,

strain, and EF effect on MAE will be presented simultaneously. Next, we continue to discuss the results on magnetic dipole-dipole interaction in ferromagnetic and antiferromagnetic systems. Finally, in Chapter 5, we summarize all results and an outlook how this work can be continued is given to expected future problems (issues).

Chapter 2

Theoretical Background

This chapter gives a basic theory appearing in this disertation. In Sec. 2.1, we briefly explain the theory of spin-orbit coupling. Two main origin contributions to the magnetic anisotropy energy (MAE) will be summarized in Sec. 2.2.1 and Sec. 2.2.3. A brief review of density functional theory will be introduced in Sec. 2.2.4.

2.1 The spin-orbit coupling

The spin-orbit coupling in atom arises as follows. In the classical picture, it arises from the orbital motion around the nucleus. Consider that electron has a circular motion around the nucleus as in the Bohr model of atom shown in the Fig. 2.1(a). In the electron rest frame, the nucleus also has a circular motion with the same periode as shown in Fig. 2.1(b) . As a nucleus carries a positive charge $+Ze$ on its circular orbit, it represents a current $\boldsymbol{I}$. The magnetic field generated by current I seen by electron is

$$\boldsymbol{B} = -\frac{1}{c^2}\boldsymbol{v} \times \boldsymbol{E},\tag{2.1}$$

where

$$\boldsymbol{E} = -\nabla V(r) = -\frac{\mathbf{r}}{r}\frac{dV(r)}{dr}\tag{2.2}$$
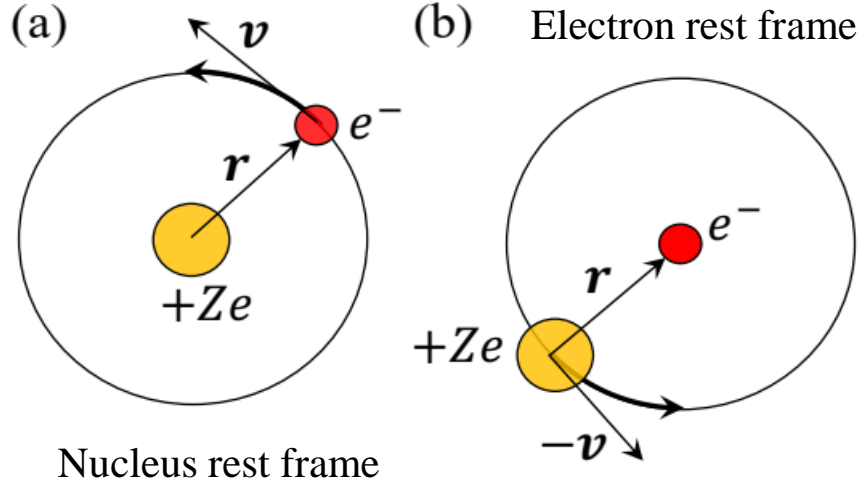
FIGURE 2.1: (a) Orbital motion of an electron in the nucleus rest frame, and (b) Orbital motion of nucleus in the electron rest frame.

is the electric field created by nucleus and $V(r)$ is the corresponding potential energy. c is the speed of light ($c = (\epsilon_0\mu_0)^{-1/2}$, where ϵ_0 and μ_0 are vacuum permittivity and vacuum permeability, respectively).

The equation (2.1) comes from the transformation of electric and magnetic fields in the special relativity. The electron has an intrinsic magnetic moment due to its spin, $\boldsymbol{\mu}_e = -\frac{e\hbar}{2m}\boldsymbol{\sigma}$, where $\boldsymbol{\sigma}$ is the vector of Pauli matrices and m is the mass of the electron. This magnetic moment interacts with a magnetic field through the Zeeman interaction,

$$
\begin{aligned}
E_{SOC} &= -\boldsymbol{\mu}_e \cdot \mathbf{B} \\
&= -\frac{e\hbar}{2m^2c^2}\boldsymbol{\sigma} \cdot (\mathbf{p} \times \mathbf{E}),
\end{aligned}
\tag{2.3}
$$

where we introduce the momentum of the electron $\mathbf{p} = m\boldsymbol{v}$. By substituting the expression of electric field in Eq. 2.2 together with the classical definition of the angular momentum $\boldsymbol{L} = \boldsymbol{r} \times \boldsymbol{p}$, finally we can get

$$
E_{SOC} = \frac{e}{m^2c^2}\frac{1}{r}\frac{dV(r)}{dr}\boldsymbol{S} \cdot \boldsymbol{L},
\tag{2.4}
$$

with $\boldsymbol{S} = \frac{\hbar}{2}\boldsymbol{\sigma}$ is the electron spin. Eq. (2.4) clearly shows that the spin couples to the angular momentum of the electron due to its orbital motion, and hence, E_{SOC} is named spin-orbit coupling (SOC).

2.2 Magnetic Anisotropy Energy

For theoretical description of the basic properties of ferromagnetic materials, it is sometimes sufficient to use non-relativistic quantum mechanics. Non-relativistic quantum mechanics leads to a description of ferromagnetism in which the free energy of the system is independent of the direction of the magnetization (isotropic). However, this contradics with the experience, that the magnetization generally lies in some preferred directions with respect to the crystalline axes and/or to external shape of the body. This property is known as magnetic anisotropy. Rotating the magnetization from the direction of lower energy (easy axis) to a high energy (hard axis) is typically of the order in energy 10^{-6} to 10^{-3} eV/atom. This anisotropy energy is thus very small corection to the total energy, which usually arise from relativistic corecction to the Hamiltonian. The main contribution is taking account from magnetic dipole-dipole interaction and spin-orbit coupling (SOC).

2.2.1 Magnetocrystalline Anisotropy: arise from spin-orbit coupling (SOC)

In the section 2.1, we introduce the SOC from the classical picture point of view. However, SOC is purely relativistic effect, and therefore not inherent in the frame of the non-relativistic Schrodinger equation or even the scalar relativistic effect. The SOC effect can be included automatically by solving the fully relativistic effect. In the limit of low velocities (order of $\frac{v^2}{c^2}$), the Dirac equations is reduce to the Pauli equation, which is essentially a Schrödinger equation with the relativistic correction. The Pauli Hamiltonian can be written as

$$H_{\text{Pauli}} = \frac{\mathbf{p}^2}{2m} - e\Phi - \frac{\mathbf{p}^4}{8m^3c^2} + \frac{e\hbar^2}{8m^2c^2}\boldsymbol{\nabla}\cdot\mathbf{E} + \frac{e\hbar}{4m^2c^2}\boldsymbol{\sigma}\cdot(\mathbf{E}\times\mathbf{p}). \qquad (2.5)$$

In Eq. (2.5), the first two terms are the non-relativistic kinetic energy and the electrostatic potential energy, respectively. These two terms form the non-relativistic Hamiltonian. The third term is the relativistic mass-velocity correction. The fourth term is the Darwin correction, which accounts for the fact that, within the relativistic theory, the electron is sensitive to the electric field $\mathbf{E}$ over a length-scale of the order of the Compton wavelength $\lambda_C = \hbar/(mc)$. The third and fourth terms are independent of the spins $\mathbf{S} = \boldsymbol{\sigma}/2$. The combination of this two terms with non-relativistic terms is called scalar-relativistic Hamiltonian. The last part is the spin-orbit coupling Hamiltonian, H_{SOC}. This term can be interpreted as the subsection 2.1.

The electric field $\mathbf{E}$ in H_{SOC} term is created by nucleus and can be written as,

$$\mathbf{E} = -\frac{\mathbf{r}}{r}\frac{dV(r)}{dr}, \tag{2.6}$$

then the spin-orbit Hamiltonian can be expresses as

$$H_{SOC} = -\frac{e\hbar}{4m^2c^2r}\frac{d\Phi}{dr}\boldsymbol{\sigma}\cdot(\mathbf{r}\times\mathbf{p}) \tag{2.7}$$

$$= -\frac{e\hbar}{2m^2c^2r}\frac{d\Phi}{dr}\mathbf{S}\cdot\mathbf{L} \tag{2.8}$$

$$= \xi(r)\mathbf{S}\cdot\mathbf{L}, \tag{2.9}$$

where $\mathbf{L} = \mathbf{r}\times\mathbf{p}$ is the orbital angular momentum operator and

$$\xi(r) = -\frac{e\hbar}{2m^2c^2r}\frac{dV(r)}{dr} \tag{2.10}$$

is the spin-orbit coupling constant. For the spherical potential $V(r) = \frac{eZ}{4\pi\epsilon_0 r}$ of a hydrogen like atom, the expectation value of the SOC constant, with respect to the non-relativistic eigenstates $|n, l\rangle$, is

$$\xi_{n,l} = \langle\xi(r)\rangle = |\langle n, l|\xi(r)|n, l\rangle| = \frac{Z^4\alpha^4mc^2}{2n^3l(l+\frac{1}{2})(l+1)}, \tag{2.11}$$
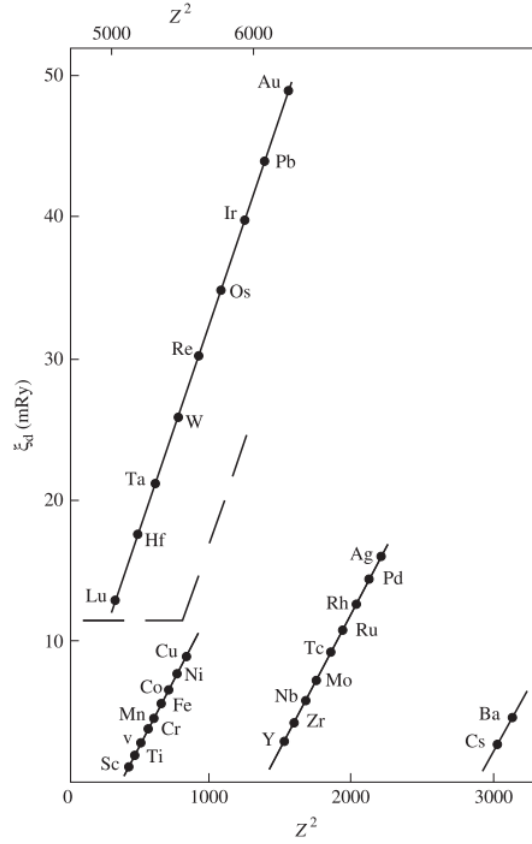
FIGURE 2.2: Spin-orbit coupling constant, ξ, for d electrons as a function of the square of the atomic number Z [1].

where Z is the atomic number, $\alpha = \frac{1}{4\pi\epsilon_0} \frac{e^2}{\hbar c}$ is the fine structure constant and n and l denote principle and angular momentum quantum numbers, respectively. From this expression it is clear that SOC becomes particularly important for states with low angular momentum in heavy atoms with large Z. The calculated spin-orbit coupling constants of transition metal are shown in Fig. 2.2. It can be seen that ξ increases with Z and the increment is approximately proportional to Z^2.

2.2.2 SOC: perturbation theory analysis

As described in the section 2.2.1, the spin-orbit Hamiltonian is H_{SOC} is $\xi\mathbf{L} \cdot \mathbf{S}$. The term $\mathbf{L} \cdot \mathbf{S}$ can be decomposed according to

$$\mathbf{L} \cdot \mathbf{S} = L_x S_x + L_y S_y + L_z S_z. \tag{2.12}$$

By using the definition of ladder operators

$$L_{\pm} = L_x \pm iL_y \tag{2.13}$$

$$S_{\pm} = S_x \pm iS_y, \tag{2.14}$$

the Eq. (2.12) can be written as

$$\mathbf{L} \cdot \mathbf{S} = \frac{1}{2}(L_+S_- + L_-S_+) + L_zS_z. \tag{2.15}$$

The z-component of the spin operator measures along a strength the direction of spin, thus

$$S_z \ket{\uparrow} = +\frac{1}{2}\hbar \ket{\uparrow} \tag{2.16}$$

$$S_z \ket{\downarrow} = -\frac{1}{2}\hbar \ket{\downarrow}, \tag{2.17}$$

where $\ket{\uparrow}$ and $\ket{\downarrow}$ represent the eigenstates of the spin operator with the spin oriented in 'up'-direction and 'down' direction, respectively. Different from S_z, the operators S_+ and S_- change the spin state according to

$$S_- \ket{\uparrow} = \ket{\downarrow}, \tag{2.18}$$

$$S_- \ket{\downarrow} = 0, \tag{2.19}$$

$$S_+ \ket{\downarrow} = \ket{\uparrow}, \tag{2.20}$$

$$S_+ \ket{\uparrow} = 0. \tag{2.21}$$

$$\tag{2.22}$$

In matrix form, the Eq. (2.15) can be rewritten as

$$
\begin{pmatrix} (\mathbf{L} \cdot \mathbf{S})^{\uparrow\uparrow} & (\mathbf{L} \cdot \mathbf{S})^{\uparrow\downarrow} \\ (\mathbf{L} \cdot \mathbf{S})^{\downarrow\uparrow} & (\mathbf{L} \cdot \mathbf{S})^{\downarrow\downarrow} \end{pmatrix} = \frac{1}{2} \left[\begin{pmatrix} 0 & 0 \\ L_+ & 0 \end{pmatrix} + \begin{pmatrix} 0 & L_- \\ 0 & 0 \end{pmatrix} \right] + \frac{1}{2} \begin{pmatrix} L_z & 0 \\ 0 & -L_z \end{pmatrix}
$$

$$
= \frac{1}{2} \begin{pmatrix} L_z & L_- \\ L_+ & -L_z \end{pmatrix}, \tag{2.23}
$$

where, in the basis set of spherical harmonics, L_+, L_- and L_z are the matrices of the size $2l + 1$.

In the case of the transition metal $3d$-electron magnetism, the SOC constant ξ is less than 100 meV. This value is much smaller than the band width (several eV). As a consequence, one can treat the SOC in subsection. 2.2.1 as a perturbation. A study based on the perturbation theory has been done long time ago, for example, the seminal work by Brooks [54], Kondorskii and Straube [55], Bruno [56], and Wang *et al* [57].

Considering the perturbation theory, the energy shift of eigenvalue E_n up to second order term due to SOC can be written as

$$
\delta E_n = \xi \langle n | \mathbf{L} \cdot \mathbf{S} | n \rangle + \xi^2 \sum_{k \neq n} \frac{|\langle n | \mathbf{L} \cdot \mathbf{S} | k \rangle|^2}{E_n - E_k}, \tag{2.24}
$$

where $|n\rangle$ and $|k\rangle$ represent eigenstates of the unperturbed Hamiltonian and E_n and E_k are the associated energy eigenvlaues. The unperturbed states have a well defined spin character (in contrast to the perturbed ones) and it is suitable to consider states such as

$$
|n\rangle = \sum_i c_{n,i} |\mathbf{k}, d_{n,i}, \sigma_n\rangle, \tag{2.25}
$$

where σ denotes the spin, the index i runs over the d-orbitals ($d_{3z^2-r^2}, d_{xz}, d_{yz}, d_{xy}$, and $d_{x^2-y^2}$) and in the case of a periodic system k denotes a point in the 1st Brillouin zone. In the ten-dimensional space which is a direct product of the two dimensional spin space and the five-dimensional space of d-states, the spin-orbit

coupling operator is a 10×10 hermitian matrix with elements which are evaluated and listed in Table 2.1. The angles θ and ϕ are the angular spherical coordinates describing the spin quantisation axis and this dependence on magnetization direction of the spin-orbit coupling matrix is the source of the magnetocrystalline anisotropy energy. All diagonal elements in Table 2.1 are zero, as well as that $\langle d_i | L_z | d_i \rangle = 0$ ($i = xy, x^2 - y^2, xz, yz, and 3z^2 - r^2$), one finds that the first order perturbation contribution of the SOC is zero. Consequently, the spin-orbit coupling is at least a second order perturbation, and it can be writtten as

$$\delta E_n = \xi^2 \sum_{k \neq n} \frac{| \langle n | \mathbf{L} \cdot \mathbf{S} | k \rangle |^2}{E_n - E_k}. \tag{2.26}$$

In the Eq. 2.26, the contribution can be separated in to two parts, that is SOC between the parallel spin states and SOC between the opposite spin states. In the case of strong exchange splitting that the spin-up band almost fully occupied and all empty states belong to spin-down bands, the only SOC between spin-down states will be considered. The approximation of MCAE from SOC between spin-down states can be written as

$$\mathrm{MCAE} \approx \xi^2 \sum_{\mathbf{k}o,u} \frac{| \langle \mathbf{k}_o | \hat{\ell}_z | \mathbf{k}_u \rangle |^2 - | \langle \mathbf{k}_o | \hat{\ell}_x | \mathbf{k}_u \rangle |^2}{\varepsilon_{\mathbf{k}u} - \varepsilon_{\mathbf{k}o}}, \tag{2.27}$$

where $\mathbf{k}_o$ and $\mathbf{k}_u$ indicate the occupied and unoccupied states with the wave vector $\mathbf{k}$ and $\hat{\ell}_z$, $\hat{\ell}_x$ are the angular momentum operators. $\varepsilon_{\mathbf{k}u}$ and $\varepsilon_{\mathbf{k}o}$ indicate the energies of unoccupied and occupied states. The SOC between occupied and unoccupied state with the same (different) in magnetic quantum number through to the $\hat{\ell}_z$ ($\hat{\ell}_x$ and $\hat{\ell}_y$) operators give positive (negative) contribution to MCAE. The nonvanishing angular momentum matrix elements between d states are listed in Table. 2.2.

TABLE 2.1: Matrix elements $\langle \sigma_i, d_i | \hat{\vec{l}} \cdot \hat{s} | \sigma_j, d_j \rangle$ of the spin-orbit coupling operator with respect to spin in the direction $\hat{n} = (\sin\theta\cos\phi, \sin\theta\sin\phi, \cos\theta)$ and d-orbitals, in unit of $\hbar^2$. Reproduced from Ref. [3, 4].

	$\lvert\uparrow, d_{xy}\rangle$	$\lvert\uparrow, d_{yz}\rangle$	$\lvert\uparrow, d_{z^2}\rangle$	$\lvert\uparrow, d_{xz}\rangle$	$\lvert\uparrow, d_{x^2-y^2}\rangle$
$\langle\uparrow, d_{xy}\rvert$	0	$\frac{1}{2}i\sin\theta\sin\phi$	0	$-\frac{1}{2}i\sin\theta\cos\phi$	$i\cos\theta$
$\langle\uparrow, d_{yz}\rvert$	$-\frac{1}{2}i\sin\theta\sin\phi$	0	$-\frac{\sqrt{3}}{2}i\sin\theta\cos\phi$	$\frac{i}{2}\cos\theta$	$-\frac{i}{2}\sin\theta\cos\phi$
$\langle\uparrow, d_{xz}\rvert$	$\frac{1}{2}i\sin\theta\cos\phi$	$-\frac{i}{2}\cos\theta$	$\frac{\sqrt{3}}{2}i\sin\theta\sin\phi$	0	$-\frac{1}{2}i\sin\theta\sin\phi$
$\langle\uparrow, d_{z^2}\rvert$	0	$\frac{\sqrt{3}}{2}i\sin\theta\cos\phi$	0	$-\frac{\sqrt{3}}{2}i\sin\theta\sin\phi$	0
$\langle\uparrow, d_{x^2-y^2}\rvert$	$i\cos\theta$	$-\frac{i}{2}\sin\theta\cos\phi$	0	$\frac{1}{2}i\sin\theta\sin\phi$	0
$\langle\downarrow, d_{xy}\rvert$	0	0	0	$-\frac{1}{2}(\sin\phi - i\cos\theta\cos\phi)$	$-i\sin\theta$
$\langle\downarrow, d_{yz}\rvert$	$\frac{1}{2}(\cos\phi - i\cos\theta\sin\phi)$	$-\frac{1}{2}(\cos\phi - i\cos\theta\sin\phi)$	$-\frac{\sqrt{3}}{2}(\sin\phi + i\cos\theta\cos\phi)$	$-\frac{i}{2}\sin\theta$	$-\frac{i}{2}(\sin\phi + i\cos\theta\cos\phi)$
$\langle\uparrow, d_{z^2}\rvert$	$\frac{1}{2}(\sin\phi + i\cos\theta\cos\phi)$	$\frac{\sqrt{3}}{2}(\sin\phi + i\cos\theta\cos\phi)$	$-\frac{\sqrt{3}}{2}(\cos\phi - i\cos\theta\sin\phi)$	$\frac{\sqrt{3}}{2}(\cos\phi - i\cos\theta\sin\phi)$	0
$\langle\downarrow, d_{xz}\rvert$	$i\sin\theta$	$\frac{i}{2}\sin\theta$	0	0	$\frac{1}{2}(\cos\phi - i\cos\theta\sin\phi)$
$\langle\downarrow, d_{x^2-y^2}\rvert$		$-\frac{i}{2}(\sin\phi + i\cos\theta\cos\phi)$		$-\frac{1}{2}(\cos\phi - i\cos\theta\sin\phi)$	0

TABLE 2.2: Nonvanishing angular momentum matrix elements between d states

Matrix elements	$\langle L_\sigma \rangle$ value
$\langle xz|L_z|yz\rangle$	1
$\langle x^2 - y^2|L_z|xy\rangle$	2
$\langle z^2|L_x|yz\rangle$	$\sqrt{3}$
$\langle xy|L_x|xz\rangle$	1
$\langle x^2 - y^2|L_x|yz\rangle$	1
$\langle z^2|L_y|xz\rangle$	$\sqrt{3}$
$\langle xy|L_y|yz\rangle$	1
$\langle x^2 - y^2|L_y|xz\rangle$	1

2.2.3 Magnetocrystalline Anisotropy: arise from magnetic dipole-dipole interaction (MDI)

Suppose m_i and m_j are two magnetic moments separated by a distance of r_{ij} in space, the magnetic dipole-dipole interaction contribution can be written as,

$$E_{\text{MDI}} = \frac{\mu_0}{8\pi} \sum_{i \neq j} \frac{1}{r_{ij}^3} [\mathbf{M}_i \cdot \mathbf{M}_j - 3\frac{(\mathbf{r}_{ij} \cdot \mathbf{M}_i)(\mathbf{r}_{ij} \cdot \mathbf{M}_j)}{r_{ij}^2}], \qquad (2.28)$$

where μ_0 is the magnetic constant and the magnetic moment is in units of the Bohr magneton (μ_B). If the magnetization distributions within each atomic cell is not spherical, then its expansion in multipoles includes not only dipolar moment, but also higher multipoles like quadropoles, octupoles, etc. The second term in dipolar contribution shows clearly that dipole energy depends on the orientation of the magnetic moments $\mathbf{M}_i$ and $\mathbf{M}_j$ with respect to r_{ij}. In the ferromagnetic case, which all magnetic moments are parallel, E_{dip} can be rewritten as,

$$E_{\text{MDI}} = \frac{\mu_0}{8\pi} \sum_{i \neq j} \frac{M_i M_j}{r_{ij}^3} (1 - 3\cos^2\theta_{ij}), \qquad (2.29)$$

where θ_{ij} is the angle between direction of the magnetic moment and vector conecting atoms i and j. Then, if the magnetization points parallel to r_{ij}, the E_{MDI} has the lowest energy. On the other hand, difficult to rotate the two dipole moments perpendicular to the r_{ij}.

2.2.4 System Many-Body Problem

Since our aim is to describe the properties of solid, so that first, we will define the Hamiltonian of interacting electrons and nuclei. In this derivation, the atomic unit will be used, that is $\hbar = m_e = e^2 = 1$, and energy will be given in the unit of Hartree. Hamiltonian of the system can be written as,

$$\mathcal{H} = \sum_i -\frac{1}{2}\nabla_i^2 - \sum_I \frac{1}{2M_I}\nabla_I^2 - \sum_{i,I} \frac{Z_I}{|\vec{r}_i - \vec{R}_I|}$$
$$+\frac{1}{2}\sum_{i \neq j} \frac{1}{|\vec{r}_i - \vec{r}_j|} + \frac{1}{2}\sum_{I \neq J} \frac{Z_I Z_J}{|\vec{R}_I - \vec{R}_J|} \tag{2.30}$$

In Eq. (2.30), the first and second term associated with the kinetic energy of electrons (T_e) and nuclei (T_{ion}), respectively. The third one, associated with the interaction between the electrons and nuclei (V_{e-ion}). The fourth and the last one, associated with the inter electronic (V_e) and inter nuclei (V_{ion}) interaction. $\vec{r}$ and $\vec{R}$ represented the position vector of electrons and nuclei, and Z_I is charge associated to the nuclei. To reduce the complexity in Eq. (2.30), the first approximation was proposed by Born and Oppenheimer which called Born-Oppenheimer approximation or adiabatic approximation. The consideration is raised in the following. Because mass of the nuclei much larger compared to the mass of electron, the nuclei moves much slowly compared to the electron movement. As a consequence, the kinetic energy of the nuclei can be neglected. Beyond this approximation, we can rewrite the Eq. (2.30) as

$$\mathcal{H} = T_e + V_{e-ion} + V_e, \tag{2.31}$$

where the term of inter-nuclei is omitted.

2.2.5 Density Functional Theory

Since the number of electrons in the solid is a huge number (N $\sim 10^{24} e^-/\text{cm}^3$), then solving the Schorodinger equation $\mathcal{H}\Phi_k = E_k\Phi_k$ whose $\mathcal{H}$ is given by the

Eq. (2.31) is a difficult task. The many body wavefunction Φ_k and many body eigenvalue E_k are difficult to obtained. The density functional theory (DFT) [58] changes the perspective from the wave function to the electron density. This is a huge simplification for a system with many body electrons, since it reduces the problem dealing with a wave function depending on $3N$ spatial coordinates, to a problem dealing with density depending on three spatial coordinates.

2.2.6 Hohenberg-Kohn Theorem

We rewrite again the Hamiltonian of many-body electron as,

$$\mathcal{H} = -\frac{1}{2}\sum_i \nabla_i^2 + \sum_i V_{\text{ext}}(\vec{r_i}) + \frac{1}{2}\sum_{i\neq j}\frac{1}{|\vec{r_i}-\vec{r_j}|}. \tag{2.32}$$

The first key ingredients of DFT to solve the Eq. (2.32) are the Hohenberg-Kohn theorems [59], which allow us to focus on electron densities, rather than wave functions. To establishing the DFT, they proposed two theorems.

Theorem 1 V_{ext} is determined uniquely, except for a constant, by $n_o(\vec{r})$ (the ground state particle density).

Proof Suppose two external potential $V_{ext}^{(1)}$ and $V_{ext}^{(2)}$ which differ more than a constant, and result in two different Hamiltonian H^1 and H^2 with the ground state wave function given by $\Psi(1)$ and $\Psi(2)$, respectively. Suppose that $\Psi(1)$ and $\Psi(2)$ lead to an equal density $n_0(\vec{r})$. In this case, we are assuming that these states are non-degenerate. From the definition of the ground state we have that,

$$E^{(1)} = \langle\Psi^{(1)}|H^{(1)}|\Psi^{(1)}\rangle < \langle\Psi^{(2)}|H^{(1)}|\Psi^{(2)}\rangle. \tag{2.33}$$

By defining $H^{(1)} = H^{(2)} + H^{(1)} - H^{(2)}$, we have

$$E^{(1)} = \langle \Psi^{(1)} | H^{(1)} | \Psi^{(1)} \rangle < \langle \Psi^{(2)} | H^{(1)} | \Psi^{(2)} \rangle + \langle \Psi^{(2)} | H^{(1)} - H^{(2)} | \Psi^{(2)} \rangle \qquad (2.34)$$

$$E^{(1)} < E^{(2)} + \int d^3r [V_{\text{ext}}^{(2)}(\vec{r}) - V_{\text{ext}}^{(1)}(\vec{r})] n_0(\vec{r}). \qquad (2.35)$$

By doing the same way, but starting with $E^{(1)}$, we will get

$$E^{(2)} < E^{(1)} + \int d^3r [V_{\text{ext}}^{(2)}(\vec{r}) - V_{\text{ext}}^{(1)}(\vec{r})] n_0(\vec{r}). \qquad (2.36)$$

If we add together Eq. (2.35) and (2.36), one can get

$$E^{(1)} + E^{(2)} < E^{(1)} + E^{(2)}, \qquad (2.37)$$

which leads to the contradiction, therefore denying the proposition and proving the theorem.

Theorem 2. A universal functional for the energy $E[n]$ in terms of the density $n(\vec{r})$ can be defined for any V_{ext}. The exact ground states of the system is the global minimum and the density that minimizes this functional is the exact ground state density.

Proof. Consider a system with ground state density $n^{(1)}(\vec{r})$ corresponding to the $V_{\text{ext}}^{(1)}(\vec{r})$, then the correspondent ground state energy can be written as

$$E^{(1)} = E[n^{(1)}] = \langle \Psi^{(1)} | H^{(1)} | \Psi^{(1)} \rangle. \qquad (2.38)$$

Now, consider a different density, $n^{(2)}(\vec{r})$, which necessarily corresponds to a different wave function, $\Psi^{(2)}$. It follows that the energy of this state, $E^{(2)}$ greater than $E^{(1)}$, since

$$E^{(1)} = \langle \Psi^{(1)} | H^{(1)} | \Psi^{(1)} \rangle < \langle \Psi^{(2)} | H^{(1)} | \Psi^{(2)} \rangle \,, \tag{2.39}$$

thus, the energy $E[n^{(1)}]$ is lower than the value for any other density. By applying a minimization procedure to the energy functional Eq. (2.39), one can obtain the ground state density.

The second theorem asserts the existence of the total energy functional of the density $E[n]$ which is minimizes, globally, by the ground state density

$$E[n] = F[n] + \int V_{\text{ext}}(\vec{r}) n(\vec{r}) d^3 r \tag{2.40}$$

where, $F[n] = T[n] + V_e[n]$. $F[n]$ was introduce being universal which is independent of the external potential $V_{\text{ext}}(\vec{r})$.

2.2.7 Kohn-Sham equations

Hohenberg and Kohn have transformed the tough problem of finding the minimum of $\langle \Psi | \hat{\mathcal{H}} | \Psi \rangle$ with respect to the $3N$-dimensional trial wave function Ψ into the problem of finding the minimum of $E[n]$. However, since the explicit form of the functional $E[n]$ in Eq. (2.46) is unknown, so in practical difficult to use. To solve this problem, Kohn and Sham [58] proposed the variational principle implied by the minimal properties of the energy functional to derive single-electron Schrodinger equations. Their basic idea is to introduce a fictitious auxilary system of non-interacting particles with an effective external potential $V_{\text{eff}}(\vec{r})$ constructs such as that the density of the auxiliary non-interacting system equals the density of the interacting system of interest. The one-to-one correspondence between the densities and the effective potentials is guaranteed by the Hohenberg-Kohn-theorems applied for V_{ee}=0. In this case, the universal functional $F[n]$ reduces to the single-particle kinetic energy functional $T_s[n]$, and the total-energy functional results in

$$E_s[n] = T_s[n] + \int V_{\text{eff}}(\vec{r})n(\vec{r})d^3r. \tag{2.41}$$

Application of the variational principle to Theorem 2 (Hohenberg-Kohn) in section 2.2.6, then leads to

$$\frac{\delta}{\delta n(\vec{r})}\left[E_s[n] + \mu\left[N - \int n(\vec{r})d^3r\right]\right] = \frac{\delta T_s[n]}{\delta n(\vec{r})} + V_{\text{eff}}(\vec{r}) - \mu = 0, \tag{2.42}$$

where we have introduced the Lagrange parameter μ so that conservation of the particles $\int n(\vec{r})d^3r = N$ is guaranteed.

Using single-particle wavefunction $\psi(\vec{r})$ allows to constract the density $n(\vec{r})$ as well as the kinetic energy functional $T_s[n]$ in the form:

$$n(\vec{r}) = \sum_{i=1}^{N}|\psi_i(\vec{r})|^2 \tag{2.43}$$

and

$$T_s[n] = \sum_{i=1}^{N}\int d^3r \nabla\psi_i^*(\vec{r}) \cdot \nabla\psi_i(\vec{r}). \tag{2.44}$$

The index i denotes both the orbotal (spatial) as well as the spin quantum numbers, and N is the number of electrons. Variation of $E[n]$ with respect to the single-particle wavefunctions $\psi_i(\vec{r})$ then give the N equations:

$$[-\frac{1}{2}\nabla^2 + V_{\text{eff}}(\vec{r})]\psi_i(\vec{r}) = \varepsilon_i\psi_i(\vec{r}), \tag{2.45}$$

which is often called the Kohn-Sham equation.

For solving the Kohn-Sham equations, it is necessary to find a useful expressionof the effective potential $V_{\text{eff}}(\vec{r})$, which is still unknown. Therefore, Kohn and Sham suggested the following splitting of the functional $E[n]$

$$E[n] = T_s[n] + \int d^3r V_{\text{ext}}(\vec{r})n(\vec{r}) + \frac{1}{2}\int\int d^3r d^3r' \frac{n(\vec{r})n(\vec{r}')}{\vec{r} - \vec{r}'} + E_{\text{xc}}[n], \quad (2.46)$$

where the third term represents the Hartree-functional and the fourth term is the so-called exchange-correlation energy functional. $E_{\text{xc}}[n]$ define as

$$E_{\text{xc}}[n] = F[n] - T_s[n] - \frac{1}{2}\int\int d^3r d^3r' \frac{n(\vec{r})n(\vec{r}')}{|\vec{r} - \vec{r}'|}. \quad (2.47)$$

Application of the variational principles to Eq. (2.46) results in

$$\frac{\delta T_s[n]}{\delta n(\vec{r})} + V_{\text{ext}}(\vec{r}) + \int d^3r' \frac{n(\vec{r}')}{|\vec{r} - \vec{r}'|} + \frac{\delta E_{\text{xc}}[n]}{\delta n(\vec{r})} - \mu = 0. \quad (2.48)$$

By comparing Eq. (2.48) with Eq. (2.42), one can find the expression of the effective potential $V_{\text{eff}}(\vec{r})$

$$V_{\text{eff}}(\vec{r}) = V_{\text{ext}}(\vec{r}) + \int d^3r' \frac{n(\vec{r}')}{|\vec{r} - \vec{r}'|} + V_{\text{xc}}(\vec{r}) \quad (2.49)$$

with

$$V_{\text{xc}}(\vec{r}) = \frac{\delta E_{\text{xc}}[n]}{\delta n(\vec{r})}. \quad (2.50)$$

The Kohn-Sham Eq. (2.45), (2.43) and (2.49) are probably the most important equations in density-functional theory. Although they are principally exact, their practical solution requires approximations, since the exchange-correlation potential is not known explicitly. The whole problem constitutes a self-consistent field

problem, since the effective potential depends on the density which, obviously, is directly connected to the wave functions (see Eq. (2.43)).

The Kohn-Sham equations can be solved iteratively, starting from a trial density which is inserted into Eq. (2.49) to obtain a first effective potential. This used to calculate the wave functions by using Eq. (2.45) and, finally, using Eq. (2.43), a new density. The procedure is repeated, until the difference between the starting density and the resulting one becomes sufficiently small.

After having solved the Kohn-Sham equations, the ground state density can be used to calculate the energy of the ground state. Considering that

$$T_s[n] = \sum_{i=1}^{N} \varepsilon_i - \int V_{\text{eff}}(\vec{r}) n(\vec{r}) d^3r, \tag{2.51}$$

the energy functional in Eq. (2.46) becomes

$$E[n] = \sum_{i=1}^{N} \varepsilon_i - \int V_{\text{eff}}(\vec{r}) n(\vec{r}) d^3r + \frac{1}{2} \int \int \frac{n(\vec{r})n(\vec{r}')}{|\vec{r} - \vec{r}'|} d^3r d^3r'$$
$$+ \int V_{\text{ext}}(\vec{r}) n(\vec{r}) d^3r + E_{\text{xc}}[n]. \tag{2.52}$$

The total energy consists of the sum over the eigenvalues ε_i minus the so-called double counting terms. Eq. (2.52) gives the ground state energy for the exact exchange-correlation functional, provided that the inserted values for the density and the effective potential are the results of the self-consistent solution.

2.2.8 Exchange and correlation functional

Although the density functional theory as presented in the last sections, i.e. the Hohenberg-Kohn theorems as well as the Kohn-Sham equations, is formally exact, its practical application requires to an approximation in the exchange-correlation functional $E_{\text{xc}}[n]$, which is not known explicitly. In the following section we will discuss the two most popular approximations for $E_{\text{xc}}[n]$.

2.2.9 Local density approximation

The local density approximation (LDA) was proposed by Kohn and Sham [58] in their original paper. It is defined as

$$E_{\mathrm{xc}}[n] = \int n(\vec{r}) \epsilon_{\mathrm{xc}}(n(\vec{r})) d^3 r, \tag{2.53}$$

where ϵ_{xc} is the exchange and correlation density of the homogeneous electron gas. The exchange-correlation (XC) functional for a given density, in volume V, is approximated by integrated XC density of the homogeneous electron density with the same density. The XC density $\epsilon_{\mathrm{xc}}(n(\vec{r}))$ can be written as a sum of exchange $\epsilon_{\mathrm{x}}(n(\vec{r}))$ and correlation $\epsilon_{\mathrm{c}}(n(\vec{r}))$:

$$\epsilon_{\mathrm{xc}}(n(\vec{r})) = \epsilon_{\mathrm{x}}(n(\vec{r})) + \epsilon_{\mathrm{c}}(n(\vec{r})). \tag{2.54}$$

For the homogeneous electron gas one can obtain the analytical solution for the exchange term. The more complicated correlation term can be computed by quantum Monte-Carlo (QMC) calculations and reacted in a parametrized form [60, 61]. One would expect that the LDA should not work for systems where the density is rapidly varying, but even in this regime the LDA has proven to give very good results. One can easily extend the above treatment for spin polarized systems, and obtain the local spin density approximation (LSDA) [62].

2.2.10 Generalized gradient approximation

Another approach is the so called generalized gradient approximation (GGA) where one includes non-local (semi-local) terms to take into account the inhomogeneity in the electronic density. The functional form of the GGA can be written as

$$E_{\mathrm{xc}}[n(\vec{r}), \vec{\nabla}(n(\vec{r})] = \int n(\vec{r}) f_{xc}((n(\vec{r}), |\vec{\nabla}(n(\vec{r})|) d^3 r. \tag{2.55}$$

There are various forms to construct such a functional, such as Perdew-Wang functional (PW91) [63] and Perdew-Burke-Ernzerhof functional (PBE) [64]. In this thesis, we are mainly interested in calculating the magnetic properties of $3d$ transition metals and their alloys and compounds. For these systems, the GGA tends to accurately describe the desired properties [65–68].

Chapter 3

Computational Methods

This chapter provides a brief description of the computational methods in this dissertation. Generally, we use spin density functional theory (SDFT) scheme implemented in house code [69], which employs scalar and fully relativistic ultrasoft pseudopotentials and planewave basis [70][71]. The generalized gradient approximation (GGA) is emploted for the exchange-correlation energy [72]. The detail of total energy calculation will be described in Sec. 3.1. Since we are interested in magnetic anisotropy energy (MAE), the scheme to evaluate the MAE is provided in Sec. 3.2. Two kinds of contribution to the MAE will be considered, namely magnetocrystalline anisotropy energy (MCAE) and shape magnetic anisotropy energy (SMAE). For the MCAE part will be evaluated on total energy (TE) difference and grand canonical force theorem (GCFT). The detail of the calculation will be described in Sec. 3.2.1 and Sec. 3.2.2, respectively. For the SMAE part, the spin density approach (SDA) and discrete approach (DA) will be employed as described in Sec. 3.2.3. Finally, the electric field effect on MAE calculation will be described in Sec. 3.2.4.

3.1 Total energy calculation

The total energy difference between two different magnetization directions is a magnetic anisotropy energy (MAE) of magnetic system. In addition to MDIE(E_{MDI}) in Eq. (2.28) , the SOC of electron provides a contribution in the MAE. This contribution has been called magnetocrystalline anisotropy energy (MCAE). These

two contributions of MDIE and MCAE may be important elements in MAE. In order to evaluate the total energy originating from SOI [71, 73, 74] , we use a spin density functional theory (SDFT)[75]. In SDFT, the total energy $E_{\text{SDFT}}[n(\mathbf{r}), \mathbf{m}(\mathbf{r})]$ is defined as a functional of electron density $n(\mathbf{r})$ and spin density $\mathbf{m}(\mathbf{r})$, where

$$n(\mathbf{r}) = \sum_i^{\text{occ.}} \Phi_i^*(\mathbf{r}) \sigma_0 \Phi_i(\mathbf{r}), \tag{3.1}$$

$$\mathbf{m}(\mathbf{r}) = \sum_i^{\text{occ.}} \Phi_i^*(\mathbf{r}) \boldsymbol{\sigma} \Phi_i(\mathbf{r}). \tag{3.2}$$

In these formula above, Φ_i is the i's bi-spinor eigenfunction, and $\boldsymbol{\sigma}$ and σ_0 is Pauli matrix and unit matrix. The index i is a short notation of (n, $\mathbf{k}$), where n and $\mathbf{k}$ are band index and wavevecotr in the two-dimensional Brillouin zone, respectively. The set of $n(\mathbf{r})$ and $\mathbf{m}(\mathbf{r})$ can be denoted as a density matrix; $\rho(\mathbf{r}) = n(\mathbf{r})\sigma_0 + \mathbf{m}(\mathbf{r}) \cdot \boldsymbol{\sigma}$. The densities are selfconsistently obtained by solving a Kohn-Sham eqation;[58]

$$\mathcal{H}_{\text{SDFT}} \Phi_i = \varepsilon_i \Phi_i, \tag{3.3}$$

where ε_i is the eigenvalue of energy band, and

$$\mathcal{H}_{\text{SDFT}} = -\frac{1}{2} \nabla^2 \sigma_0 + \hat{V}_{\text{eff}}. \tag{3.4}$$

$\hat{V}_{\text{eff}}$ is the effective electron potential which is determined self-consistently as a functional of ρ (n and $\mathbf{m}$). In $\hat{V}_{\text{eff}}$, the SOC potential can be included as a term $V_{\text{SOC}} = \xi \mathbf{L} \cdot \boldsymbol{\sigma}$, where ξ and $\mathbf{L}$ are a SOC constant and orbital angular moment vector, respectively. Disregarding the SOC, Φ_i and ε_i does not depend on the direction of magnetization vector. E_{SDFT} is given by

$$E_{\text{SDFT}} = \sum_i^{\text{occ.}} \int d\mathbf{r} \Phi_i^*(\mathbf{r}) \left(-\frac{1}{2} \nabla^2 \sigma_0 \right) \Phi_i(\mathbf{r}) + \int d\mathbf{r} n(\mathbf{r}) V_{\text{ext}}(\mathbf{r})$$
$$+ \frac{1}{2} \int \int d\mathbf{r} d\mathbf{r}' \frac{n(\mathbf{r})n(\mathbf{r}')}{|\mathbf{r} - \mathbf{r}'|} + E_{\text{XC}}[n, \mathbf{m}] + U, \tag{3.5}$$

where V_{ext} is a potential from nuclei and inner core states and E_{XC} is an exchange-correlation energy which is a functional of n and $\mathbf{m}$. U represents the interaction energy between nuclei and inner core states. The KS equation can be derived by minimizing Eq.(3.5) to the subject of orthonormal relation $\int d\mathbf{r} \Phi_i^*(\mathbf{r}) \Phi_j(\mathbf{r}) = \delta_{ij}$.

Using ε_i, E_{SDFT} is presented as follows:

$$E_{\text{SDFT}} = \sum_i^{\text{occ.}} \varepsilon_i + \Delta E[n, \mathbf{m}] + U. \tag{3.6}$$

$$\Delta E[n, \mathbf{m}] = -\frac{1}{2} \iint d\mathbf{r} d\mathbf{r}' \frac{n(\mathbf{r})n(\mathbf{r}')}{|\mathbf{r} - \mathbf{r}'|}$$
$$- \int d\mathbf{r} \left[\frac{\delta E_{\text{XC}}}{\delta n(\mathbf{r})} n(\mathbf{r}) + \frac{\delta E_{\text{XC}}}{\delta m(\mathbf{r})} m(\mathbf{r}) \right] + E_{\text{XC}}[n, \mathbf{m}]. \tag{3.7}$$

$\Delta E[n, \mathbf{m}]$ is a functional of electron density matrix (n and $\mathbf{m}$). E_{SDFT} and ε_i depend on the magnetization direction of system, while they are independent of the direction when neglecting the SOC (V_{SOC}).

Within the combination of E_{MDI} and E_{SDFT}, a new total energy functional E_{tot} is defined as

$$E_{\text{tot}}[n, \mathbf{m}] = E_{\text{SDFT}}[n, \mathbf{m}] + E_{\text{MDI}}[\mathbf{m}]. \tag{3.8}$$

This energy can be used in the evaluation of MAE.

3.2 Magnetic anisotropy energy calculation

We evaluated the MCAE in two schemes. First, the MCAE is calculated including spin-orbit interaction (SOI) based on the total energy (TE) difference between the magnetizations along in-plane and perpendicular to the plane. Second, we calculated the MCAE based on grand canonical force theorem (GCFT). The GCFT calculation involves two steps. At the first step, a density $\rho(\mathbf{r})$ is generated in self-consinstent field (SCF) calculation without taking into account SOI. At the second step, fixing $\rho(\mathbf{r})$ at the SCF, two calculations are performed, including SOI with the magnetizations pointing toward in-plane and perpendicular to the plane, respectively. The sets of resulting eigenvalues $\tilde{\varepsilon}_{n\mathbf{k}}^{\hat{\mathbf{m}}}$ are used as discussed in later part.

3.2.1 Total energy difference

The total energy (TE) depends on the magnetization direction. The direction is denoted by $\hat{\mathbf{m}}$ (presented as [001], [100] or [010]). In this thesis, we consider the

MAEs of total energy difference, as follows:

$$MAE = E_{tot}^{[100]} - E_{tot}^{[001]} = MCAE + MDIE, \tag{3.9}$$

$$MCAE = E_{SDFT}^{[100]} - E_{SDFT}^{[001]}, \tag{3.10}$$

$$MDIE = E_{MDI}^{[100]} - E_{MDI}^{[001]}. \tag{3.11}$$

[001] (z-direction) indicates the magnetization direction perpendicular to the slab plane. The direction [100] (x-direction) was taken to be perpendicular to a mirror plane forming by the directions of [001] and [010] (y-direction). Along the approach of TE difference, it may be difficult to separate the MCAE into atom-resolved or **k**-resolved contributions.

3.2.2 Grand-canonical force theorem

Alternatively, the MCAE can be estimated in a different procedure. That procedure is based on magnetic force theorem (FT) [76]. This approach has successfully been used in the evaluation of MAE, such as several cubic/tetragonal bulk systems. However, we need an additional treatment for an accurate MAE of 2D or 1D system [77]. That is based on a grand-canonical force theorem (GCFT). In this work we take an approach similar to the GCFT. As a result we may discuss the atom-resolved and **k**-resolved contributions of MCAE reasonably.

The total energy of simple FT is given by

$$E_{SDFT}^{f,\hat{\mathbf{m}}} = \sum_i^{occ.} \tilde{\varepsilon}_i^{\hat{\mathbf{m}}} + \Delta E[n, \mathbf{m}] + U, \tag{3.12}$$

$$E_{SDFT}^{f,0} = \sum_i^{occ.} \varepsilon_i^0 + \Delta E[n, \mathbf{m}] + U \tag{3.13}$$

$$E_{SDFT}^{f,\hat{\mathbf{m}}} = \sum_i^{occ.} \tilde{\varepsilon}_i^{\hat{\mathbf{m}}} - \sum_i^{occ.} \varepsilon_i^0, \tag{3.14}$$

$$\delta E_{SDFT}^{f,\hat{\mathbf{m}}} = \sum_i^{occ.} \tilde{\varepsilon}_i^{\hat{\mathbf{m}}} \tag{3.15}$$

where $\tilde{\varepsilon}_i^{\hat{\mathbf{m}}}$ and ε_i^0 are the eigenvalues for the potentials (V_{eff}) with and without SOC, respectively. $\Delta E[n, \mathbf{m}]$ employs the densities of $n(\mathbf{r})$ and $\mathbf{m}(\mathbf{r})$ which are determined self-consistently without the potential of SOC.

The MCAE is evaluated as the total energy difference between the different magnetizations. Considering the magnetization directions of $\hat{\mathbf{m}}_1$ and $\hat{\mathbf{m}}_2$, the MCAE is given by

$$\mathrm{MCAE} = \sum_i^{\mathrm{occ.}} \tilde{\varepsilon}_i^{\hat{\mathbf{m}}_1} - \sum_i^{\mathrm{occ.}} \tilde{\varepsilon}_i^{\hat{\mathbf{m}}_2}. \tag{3.16}$$

In the analysis of nanomaterials, atom-resolved or $\mathbf{k}$-resolved MCAE has been effective. However, it has been found that the simple procedure of FT give a physically unreasonable result in the system that we investigated before. For examples, in an atom-resolved analysis, a large atomic MCAE appears on the atom which may have a small SOC, and in a $\mathbf{k}$-resolved analysis, there is a $\mathbf{k}$-space local contribution which cannot be connected to the involving eigenvalues. This is basically caused by the fact that the physical quantity of MCAE is sensitive to the electron occupation around the Fermi level. In the previous work, it was found that the MCAE atomic contribution tends to deviate from a reasonable value at the material edges [77].

Let us consider effect of the electron occupation in the total energy. From Eq. (3.14), introducing a set of electron occupations, we may suppose the following extension:

$$E_{\mathrm{SDFT}}^{\mathrm{gf},\hat{\mathbf{m}}} = \sum_i f_i^{\hat{\mathbf{m}}}(\tilde{\varepsilon}_i^{\hat{\mathbf{m}}} - \mu^{\hat{\mathbf{m}}}) - \sum_i f_i^0(\varepsilon_i^0 - \mu^0), \tag{3.17}$$

where $f_i^{\hat{\mathbf{m}}}$ and f_i^0 are electron occupations with and without SOC, and $\mu^{\hat{\mathbf{m}}}$ and μ^0 are chemical potentials. f_i^0 and μ^0 may be determined self-consistently in a usual process when solving the KS equation. However, the relation between $f_i^{\hat{\mathbf{m}}}$ and $\mu^{\hat{\mathbf{m}}}$ is not determined a priori because $\tilde{\varepsilon}_i^{\hat{\mathbf{m}}}$ is evaluated not from a self-consistent potential, but from the potential calculated with using the densities (n and $\mathbf{m}$) determined self-consistently without the SOC. In this extension, $f_i^{\hat{\mathbf{m}}}$ and $\mu^{\hat{\mathbf{m}}}$ are assumed to be independent of each other and $f_i^{\hat{\mathbf{m}}}$ is a function of the set of $\{\tilde{\varepsilon}_i^{\hat{\mathbf{m}}}\}$ values.

In the present GCFT,

$$\mathrm{MCAE} = \sum_i f_i^{\hat{\mathbf{m}}_1}(\tilde{\varepsilon}_i^{\hat{\mathbf{m}}_1} - \mu^{\hat{\mathbf{m}}_1}) - \sum_i f_i^{\hat{\mathbf{m}}_2}(\tilde{\varepsilon}_i^{\hat{\mathbf{m}}_2} - \mu^{\hat{\mathbf{m}}_2}) \tag{3.18}$$

$$= \sum_i f_i^{\hat{\mathbf{m}}_1}\tilde{\varepsilon}_i^{\hat{\mathbf{m}}_1} - \sum_i f_i^{\hat{\mathbf{m}}_2}\tilde{\varepsilon}_i^{\hat{\mathbf{m}}_2} - N_{\mathrm{e}}\sum_i(\mu^{\hat{\mathbf{m}}_1} - \mu^{\hat{\mathbf{m}}_2}), \tag{3.19}$$

where N_e is the number of electrons in the system, resulting from $\sum_i f_i^{\hat{\mathbf{m}}_1} = \sum_i f_i^{\hat{\mathbf{m}}_2} = N_e$. Introducing a common chemical potential μ to $\mu^{\hat{\mathbf{m}}_1}$ and $\mu^{\hat{\mathbf{m}}_2}$, namely, $\mu^{\hat{\mathbf{m}}_1} = \mu + \delta\mu^{\hat{\mathbf{m}}_1}$ and $\mu^{\hat{\mathbf{m}}_2} = \mu + \delta\mu^{\hat{\mathbf{m}}_2}$. Substituting these and neglecting the δ terms,

$$\text{MCAE} = \sum_i f_i^{\hat{\mathbf{m}}_1}(\tilde{\varepsilon}_i^{\hat{\mathbf{m}}_1} - \mu) - \sum_i f_i^{\hat{\mathbf{m}}_2}(\tilde{\varepsilon}_i^{\hat{\mathbf{m}}_2} - \mu) \tag{3.20}$$

$$= \sum_i f_i^{\hat{\mathbf{m}}_1}\tilde{\varepsilon}_i^{\hat{\mathbf{m}}_1} - \sum_i f_i^{\hat{\mathbf{m}}_2}\tilde{\varepsilon}_i^{\hat{\mathbf{m}}_2} \tag{3.21}$$

From the last term of Eq. (3.19), the change in MCAE is sensitive to the difference between $\mu^{\hat{\mathbf{m}}_1}$ and $\mu^{\hat{\mathbf{m}}_2}$ due to a largeness of N_e. Thus, in the later practical application for atom-resolved MCAE and k-resolved MCAE, we assume these chemical potentials to be the same, as derived in Eq. (3.20).

In order to separate the total MCAE to atom-resolved or $\mathbf{k}$-resolved contributions, we consider a total energy related to Eq. (3.20):

$$\delta E_{\text{SDFT}}^{\text{gf},\hat{\mathbf{m}}} = \sum_i f_i^{\hat{\mathbf{m}}}(\tilde{\varepsilon}_i^{\hat{\mathbf{m}}} - \mu). \tag{3.22}$$

Using the explicit notation of $i = (n, \mathbf{k})$,

$$\delta E_{\text{SDFT}}^{\text{gf},\hat{\mathbf{m}}}(\mathbf{k}) = \sum_n f_{n\mathbf{k}}^{\hat{\mathbf{m}}}(\tilde{\varepsilon}_{n\mathbf{k}}^{\hat{\mathbf{m}}} - \mu), \tag{3.23}$$

$$\delta E_{\text{SDFT}}^{\text{gf},\hat{\mathbf{m}}}(I) = \sum_n \sum_{\mathbf{k}} \sum_a f_{n\mathbf{k}}^{\hat{\mathbf{m}}}(\tilde{\varepsilon}_{n\mathbf{k}}^{\hat{\mathbf{m}}} - \mu)|\langle\chi_{Ia}|\Phi_{n\mathbf{k}}\rangle|^2, \tag{3.24}$$

$$\delta E_{\text{SDFT}}^{\text{gf},\hat{\mathbf{m}}}(I, \mathbf{k}) = \sum_n \sum_a f_{n\mathbf{k}}^{\hat{\mathbf{m}}}(\tilde{\varepsilon}_{n\mathbf{k}}^{\hat{\mathbf{m}}} - \mu)|\langle\chi_{Ia}|\Phi_{n\mathbf{k}}\rangle|^2, \tag{3.25}$$

where χ_{Ia} is the a'th atomic orbital on the atom I. As indicated in Eqs. (3.23) – (3.25), the $\mathbf{k}$-resolved or atom-resolved contribution depends on μ and $f_{n\mathbf{k}}^{\hat{\mathbf{m}}}$ as well as $\tilde{\varepsilon}_{n\mathbf{k}}^{\hat{\mathbf{m}}}$. Both of the $\mathbf{k}$-space distribution $\delta E_{\text{SDFT}}^{\text{gf},\hat{\mathbf{m}}}(\mathbf{k})$ and the atomic distribution may be sensitive to μ. Nevertheless the main feature of these distributions may come from $\tilde{\varepsilon}_{n\mathbf{k}}^{\hat{\mathbf{m}}}$. Therefore, the $\mathbf{k}$-variation of $\delta E_{\text{SDFT}}^{\text{gf},\hat{\mathbf{m}}}(\mathbf{k})$ will has a symmetry of system.

The **k**-resolved or atom-resolved MCAE is given by the energy difference between the magnetization directions of $\hat{\mathbf{m}}_1$ and $\hat{\mathbf{m}}_2$ using Eq. (3.23) or Eq. (3.24):

$$\text{MCAE}(\mathbf{k}) = \delta E_{\text{SDFT}}^{\text{gf},\hat{\mathbf{m}}_1}(\mathbf{k}) - \delta E_{\text{SDFT}}^{\text{gf},\hat{\mathbf{m}}_2}(\mathbf{k}), \tag{3.26}$$

$$\text{MCAE}(I) = \delta E_{\text{SDFT}}^{\text{gf},\hat{\mathbf{m}}_1}(I) - \delta E_{\text{SDFT}}^{\text{gf},\hat{\mathbf{m}}_2}(I), \tag{3.27}$$

$$\text{MCAE}(I, \mathbf{k}) = \delta E_{\text{SDFT}}^{\text{gf},\hat{\mathbf{m}}_1}(I, \mathbf{k}) - \delta E_{\text{SDFT}}^{\text{gf},\hat{\mathbf{m}}_2}(I, \mathbf{k}). \tag{3.28}$$

In this thesis, results for $\hat{\mathbf{m}}_2 = [001]$ and $\hat{\mathbf{m}}_1 = [100]$ or $[010]$ will be presented.

3.2.3 Magnetic dipole interaction energy calculation

The magnetic dipole interaction energy (MDIE) among electrons, resulting in a shape magnetic anisotropy in magnetic materials, may be represented by the integral of the dipole-dipole interaction between the spin moment densities $\mathbf{m}(\mathbf{r}) = [m_x(\mathbf{r}), m_y(\mathbf{r}), m_z(\mathbf{r})]$ at different real-space positions. The energy can be written in the Hartree unit as follows [76, 78]:

$$E_{\text{MDI}}^{\text{SDA}} = \frac{1}{8c^2} \iint d\mathbf{r} d\mathbf{r}' \left[\frac{\mathbf{m}(\mathbf{r}) \cdot \mathbf{m}(\mathbf{r}')}{|\mathbf{r} - \mathbf{r}'|^3} - 3\frac{\{(\mathbf{r} - \mathbf{r}') \cdot \mathbf{m}(\mathbf{r})\}\{(\mathbf{r} - \mathbf{r}') \cdot \mathbf{m}(\mathbf{r}')\}}{|\mathbf{r} - \mathbf{r}'|^5} \right] \tag{3.29}$$

where $c = 137.0370$ and $\mathbf{m}(\mathbf{r})$ is given in the unit $\mu_{\text{B}}/a_{\text{B}}^3$ (μ_{B}: Bohr magneton, a_{B}: Bohr radius). The contribution to E_{MDI} at $\mathbf{r} = \mathbf{r}'$ should vanish due to the self-interaction of electrons, and the explicit treatment of this exclusion is usually necessary in a practical calculation. To evaluate E_{MDI}, one can use a spin density of electron, $\mathbf{m}$ determined by a non-empirical approach, such as a spin density functional approach.[75] In a slab system, the two-dimensional Ewald method is applied to evaluate E_{MDI} [79]. We also use the discrete (atomic moment) model approach (DA) for a purpose of comparison. The real-space distribution near the atomic site in $\mathbf{m}(\mathbf{r})$ tends to have spherical symmetry. The actual shape of the magnetic moment density distribution with such symmetry does not contribute to E_{MDI} or the MAE in the atomic region. Therefore, the simplified formula, given as follows, is considered [78]:

$$E_{\text{MDI}}^{\text{DA}} = \frac{1}{8c^2} \sideset{}{'}\sum_{\mathbf{R},\mathbf{t},\mathbf{t}'} \left[\frac{\mathbf{m}_{\mathbf{t}} \cdot \mathbf{m}_{\mathbf{t}'}}{|\mathbf{R} + \mathbf{t} - \mathbf{t}'|^3} - 3\frac{\{(\mathbf{R} + \mathbf{t} - \mathbf{t}') \cdot \mathbf{m}_{\mathbf{t}}\}\{(\mathbf{R} + \mathbf{t} - \mathbf{t}') \cdot \mathbf{m}_{\mathbf{t}'}\}}{|\mathbf{R} + \mathbf{t} - \mathbf{t}'|^5} \right] \tag{3.30}$$

where $\mathbf{R}$ indicates the translational lattice vector, $\mathbf{m_t}$ is the atomic magnetic moment integrated in a given atomic sphere with $\mathbf{m}(\mathbf{r})$, and the sum with the prime $\sum'$ means that the cases of $\mathbf{R} + \mathbf{t} - \mathbf{t}' = 0$ are excluded.

In addition to the SDA and DA approach, we also evaluated MDIE by using continuuum approach (CA) [80]. In CA calculation, data of total magnetization and a parameter of the slab thickness will be used. The MDIE from CA can be calculated as,

$$E_{\mathrm{MDI}}^{\mathrm{CA}} = \frac{\mu_0 M^2}{2\Omega} \tag{3.31}$$

where μ_0, M, and Ω are the vacuum permeability, total magnetic moment, and slab volume, respectively. In this formula, a uniform spin density is assumed in the magnetic slab.

3.2.4 Electric field effect on MAE calculation

In order to impose the electric field (EF), we have applied the scheme of effective screening medium (ESM) method along the z-axis ([001]) [81]. Here, a short summary about this method is explained as follows. The ESM method provides the electrostatic potential (Hartree potential V_{H}):

$$V_{\mathrm{H}}(\mathbf{r}) = \int G(\mathbf{r}, \mathbf{r}') n(\mathbf{r}') d\mathbf{r}', \tag{3.32}$$

where $G(\mathbf{r}, \mathbf{r}')$ and $n(\mathbf{r}')$ are Green's functions and charge density, respectively. The Fourier component of G is given by

$$G(\mathbf{g}_\parallel, z, \ z') = \frac{4\pi}{2g_\parallel} e^{-g_\parallel |z - \ z'|} - \frac{4\pi}{2g_\parallel} e^{-g_\parallel (2z_1 - z - \ z')}, \tag{3.33}$$

where the $\mathbf{g}_\parallel$ and $g_\parallel$ are the two-dimensional reciprocal vector and its modulus, and z_1 specifies the place of ESM. The first term of equation (2) means the kernel

function of simple Coulomb interaction and the second one is introduced for effects of the mirror charge raised by the ESM of ideal conductor. In addition, the boundary conditions are imposed as follows:

$$V_H(\mathbf{g}_\parallel, z)|_{z=z_1} = 0, \tag{3.34}$$

$$\frac{\partial}{\partial z} V_H(\mathbf{g}_\parallel, z) \mid_{z=-\infty} = 0. \tag{3.35}$$

In the application, the minus infinity ($z=-\infty$) of the z-coordinate is replaced by a finite practical value far from the other artificial surface in the slab model. The ESM, as shown in Fig. 4.1, is placed away from the slab system at the distance of 0.79 nm. Some tiny number of electrons is substracted from or added to the systems for the induction of positive and negative EF respectively. The strength of EF (ε) is estimated from the slope of the electrostatic potential at the front of ESM as seen in Fig. 3.1. The effective EF in the MgO layer was determined by dividing the above EF with dielectric constant ($\varepsilon_r = 9.8$). The Kohn-Sham equation, which contains the electrostatic potential given above, is solved in the framework of the slab model. The detail of similar application on ESM method can be found in the previous reports [41, 82, 83].
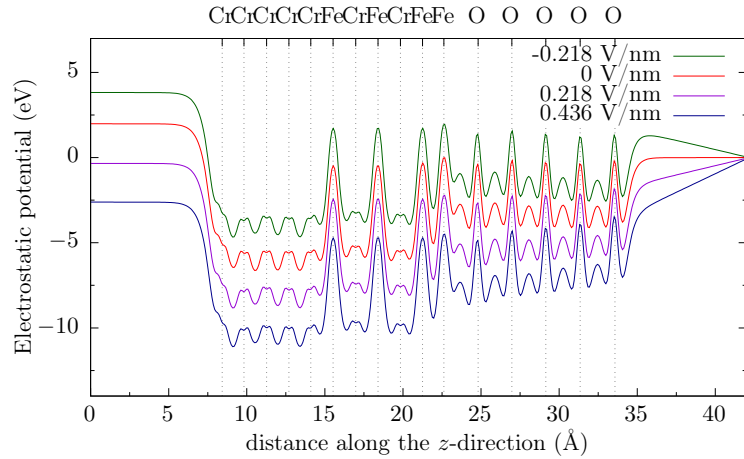
FIGURE 3.1: Electrostatics potential in slab system Cr (5ML)/Fe (1ML)/Cr (1ML)/Fe (1ML)/Cr (1ML)/Fe (2ML)/MgO (5ML). The blue, purple, red, and green colours indicating EF of 0.436 V/nm, 0.218 V/nm, 0 V/nm, and -0.218 V/nm correspond to electron depletions or accumulations in the slab of -0.02, -0.01, 0.0 and 0.01, respectively

Chapter 4

Results and Discussions

4.1 Magnetic Anisotropy and Electric Field Control Magnetic Anisotropy at Fe/MgO interface

4.1.1 MAE and EF effect on MAE in Fe/Cr alloying

For a practial application of a new type of MRAM that is controlled by voltage (voltage-torque MRAM), a large perpendicular MAE and large EF effect are needed for the smaller-size magnetic layer element and the accurate dynamic magnetization switching [2]. Among this purpose, many effects were proposed such as a strain effect [84], and an underlayer effect [46]. The underlayer effect becomes important, for example, in the case of alloying during the fabrication of samples. Nozaki *et al* suggested that an Fe/Cr alloying in the Cr/Fe/MgO system possibly happens when an annealing is used during the deposition process [2]. They discussed that the annealing makes a large effect in the quantities of the perpendicular magnetic anisotropy (PMA), saturation magnetization, and voltage control magnetic anisotropy (VCMA). Later, such alloying in the same system was clearly observed by using the conversion electron Mössbauer spectroscopy (CEMS) measurement [85]. Motivated by the experimental results, we systematically investigated EF effect in Fe/MgO interface systems with Cr underlayer by introducing the interchange of Cr and Fe layers [86]. We use slab system, vacuum (0.79 nm)/Cr (6ML)/Fe (1ML)/Cr (1ML)/Fe (3ML)/MgO (5ML)/vacuum
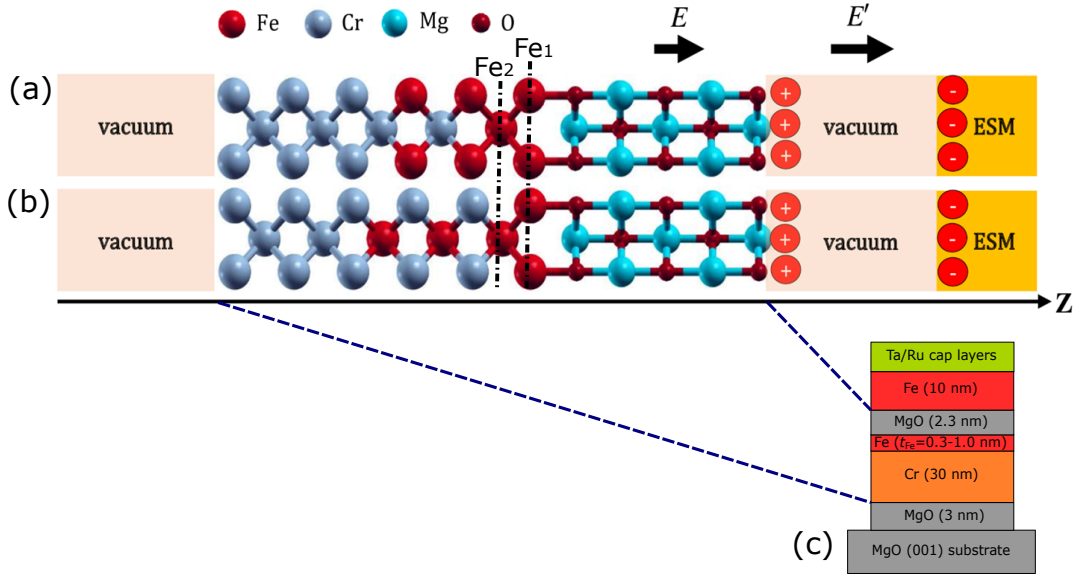
FIGURE 4.1: Schematic diagram of the computational model (a) system-A, (b) system-B, and (c) experimetal structure from ref. [2]. The black arrows with label E and E' indicate the electric field in MgO and the vacuum respectively.

(0.79 nm) (system-A) and vacuum (0.79 nm)/Cr (5ML)/Fe (1ML)/Cr (1ML)/Fe (1ML)/Cr (1ML)/Fe (2ML)/MgO (5ML)/vacuum (0.79 nm) (system-B) as shown in Fig. 4.1. We carried out first-principles electronic structure calculations [69] which employ fully relativistic and scalar relativistic ultrasoft pseudopotentials and a plane wave basis by using the generalized gradient approximation (GGA) for the exchange-correlation energy [71]. The magnetic anisotropy energy (MAE) was evaluated by considering magnetocrystalline anisotropy energy (MCAE) and shape mangetic anisotropy energy (SMAE). The MCAE calculated by using total energy difference (TED) and grand canonical force theorem (GCFT), while SMAE calculated by using discrete approach (DA) and spin density approach (SDA) . We used a 32×32×1 **k**-mesh for both MCAE and EF calculations. Using the scalar-relativistic level computation with a 24×24×1 **k**-mesh, we induced structural relaxation while keeping both the in-plane lattice constant and the atomic coordinates of O(3). To apply an EF, we used the effective screening medium (ESM) method [81]. To obtain the EF inside the MgO layer, we took into account the dielectric constant ε_r (9.8 for MgO) [87].

The total MAE originated from MCAE(SOI) and SMAE for system-A and system-B are summarized in Table 4.1. For the comparison, we also include the data of system without alloying, with structure of Cr(6ML)/Fe(4ML)/MgO(5ML) (structure-I) [88].

TABLE 4.1: The MAE from MCAE and SMAE for Cr(6MLs)/Fe(4MLs)/MgO(5MLs) (structure-I), system-A and system-B. The MCAE evaluated based on total energy (TE). The MDIE evaluated from discrete approach (DA) and spin density approach (SDA).

Structure	a(Å)	MCAE(SOI) mJ/m²	SMAE mJ/m²		MAE (SOI+SMAE) mJ/m²	
			DA	SDA	SOI+DA	SOI+SDA
I	2.88	0.586	-1.353	-1.336	-0.763	-0.750
System-A	2.88	1.280	-1.097	-1.053	0.183	0.227
System-B	2.88	1.483	-0.829	-0.797	0.651	0.686

TABLE 4.2: The MCAE value calculated based on the total energy (TE) and grand canonical force theorem (GCFT)

Structure	MCAE(TE) (mJ/m²)	MCAE(GCFT) (mJ/m²)
I	0.586	0.584
System-A	1.280	1.261
System-B	1.483	1.483

From Table 4.1, the MCAE from SOI contribution is largely enhanced compared to the structure-I [88]. In the structure-I, the MAE becomes negative after combining with the SMAE contribution. This means, the easy axis is along the in-plane. On the other hand, for system-A and system-B, after combining with the MDIE contribution, they have a positive MAE values. Both results have same sign with the experimental value [2]. In the experiment, for t_{Fe}=0.56 nm (corresponding to the 4ML, because 1 ML≈0.14 nm), the MAE value is ≈ 0.5 mJ/m².

In addition to the MCAE from TE, the MCAE was calculated based on the GCFT. The results are shown in Table 4.2. From Table 4.2, we can see that there is a good agreement between these two methods.

Next, in the basis of the GCFT method, we performed the calculation of atom-resolved MCAE as shown in Fig. 4.2. The positive and negative values in the figure indicate a PMCAE and IPMCAE, respectively. We can see clearly that the main positive contribution to the MCAE comes from Fe interfacing with MgO (Fe_1). The MCAE contribution from Fe_1 in structure-I is suppressed compared to the Fe_1 in system-A and system-B. In addition, in structure-I, the Fe inside the layer (Fe_3 and Fe_4) also contribute to the IPMCAE. As a final result, the MCAE in structure-I becomes much suppressed.

To elucidate more the origin of the enhancement of MCAE in system-A and system-B compared to the structure-I, we calculated the *k*-resolved MCAE in the
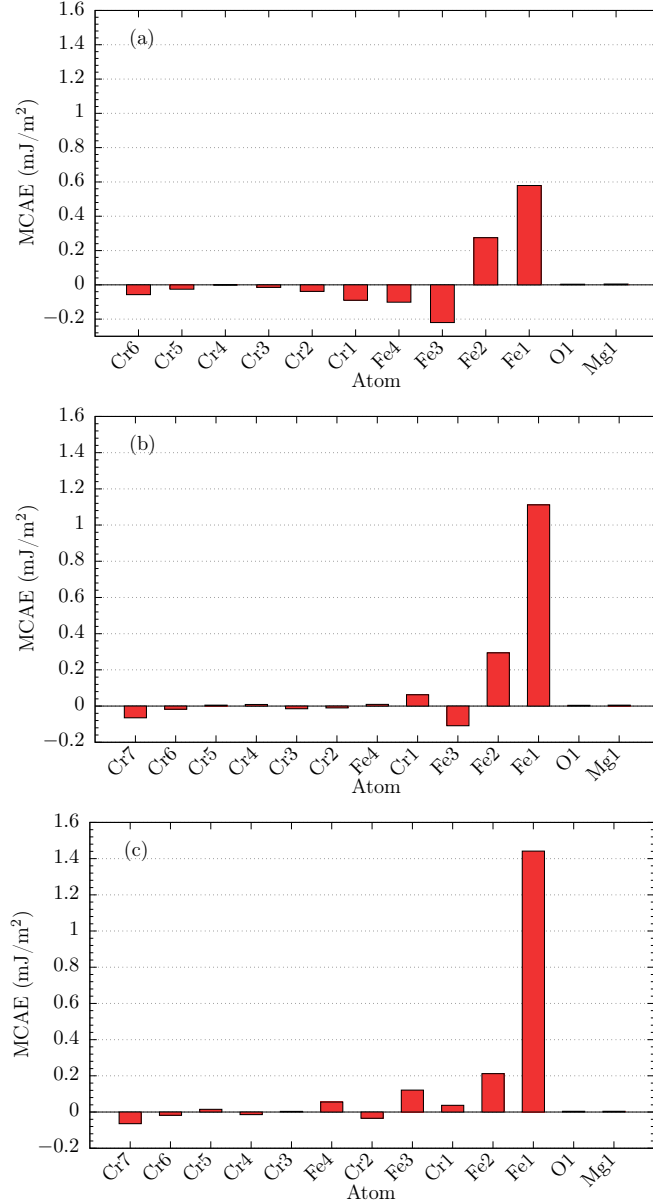
FIGURE 4.2: Atomic resolved MCAE, (a) structure-I, (b) system-A and (c) system-B, respectively.

two dimensional Brillouin zone (2DBZ) for each system. The results are shown in Fig. 4.3. The energy range from red to blue indicates the positive to negative contribution to the MCAE. We can see that, in the 2DBZ, only a certain region contributes to the MCAE (the other regions almost vanish).

By considering the second-order perturbation theory, as discussed in the theoretical section (see. Eq. 2.24 in Sec. 2.2.2), may be the states near the Fermi energy is important to discuss the origin of MCAE. To check the detail of pair coupling near the Fermi energy, we plotted the band dispersion curve of minority $3d$-orbitals of each system as shown in the Fig. 4.6. Here, we focus on the minority spin-states
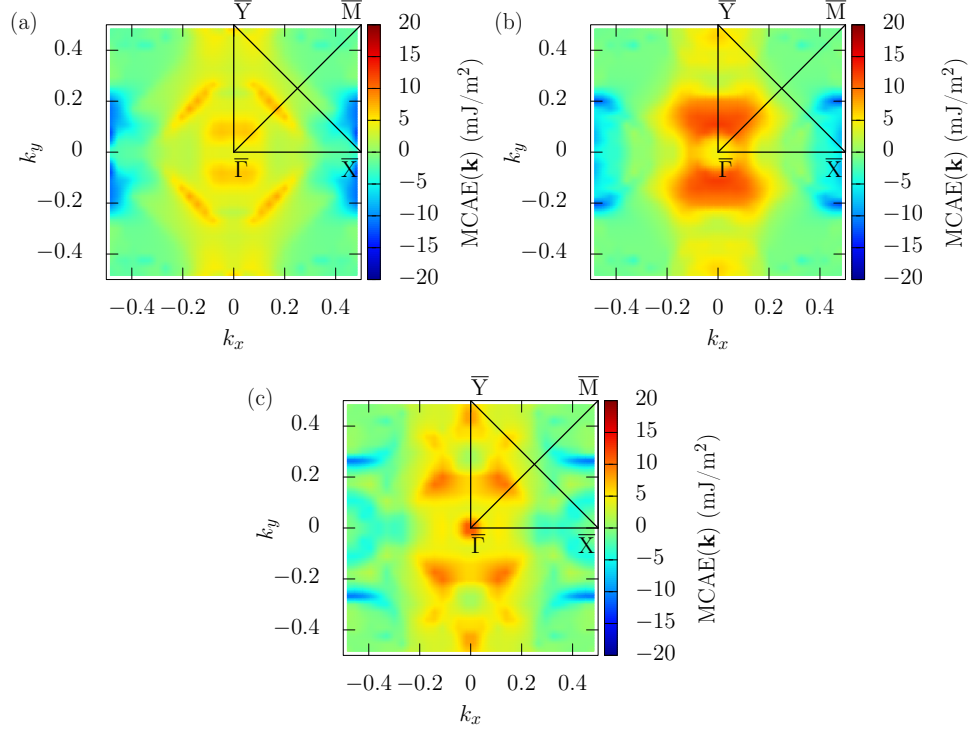
FIGURE 4.3: k-resolved MCAE, (a) structure-I, (b) system-A and (c) system-B, respectively.

TABLE 4.3: Positive and negative contribution to the MCAE in the 2DBZ for the structure-I due to SOCs of d-orbital states. o and u represent occupied and unoccupied states, respectively.

Line in 1st-BZ	Matrix elements
$(3/8)\overline{\Gamma} - \overline{M}$	$\langle o, xy|\hat{\ell}_z|u, x^2 - y^2\rangle$
$(7/8)\overline{Y} - \overline{\Gamma}$	$\langle o, yz|\hat{\ell}_z|u, xz\rangle$
$(5/8)\overline{M} - \overline{X}$	$\langle o, xy|\hat{\ell}_x|u, xz\rangle$
	$\langle u, xy|\hat{\ell}_x|o, xz\rangle$
	$\langle u, xz|\hat{\ell}_x|o, x^2 - y^2\rangle$
	$\langle u, yz|\hat{\ell}_x|o, 3z^2 - r^2\rangle$

contributions, since the majority spin-states are fully occupied (see Fig. 4.11). The summary of the possible spin-orbit couplings (SOCs) of d-orbital states near the Fermi energy is listed in Table 4.3, 4.4, and 4.5 for structure-I, system-A, and system-B, respectively.

TABLE 4.4: Positive and negative contribution to the MCAE in the 2DBZ for the system-A due to SOCs of *d*-orbital states. *o* and *u* represent occupied and unoccupied states, respectively.

Line in 1st-BZ	Matrix elements
$(2/8\text{-}4/8)\overline{\Gamma} - \overline{Y}$	$\langle o, yz|\hat{\ell}_z|u, xz\rangle$
	$\langle u, yz|\hat{\ell}_z|o, xz\rangle$
$(5/8)\overline{M} - \overline{X}$	$\langle o, xy|\hat{\ell}_x|u, xz\rangle$
	$\langle u, xy|\hat{\ell}_x|o, xz\rangle$
	$\langle u, xz|\hat{\ell}_x|o, x^2 - y^2\rangle$

TABLE 4.5: Positive and negative contribution to the MCAE in the 2DBZ for the system-B due to SOCs of *d*-orbital states. *o* and *u* represent occupied and unoccupied states, respectively.

Line in 1st-BZ	Matrix elements
$(2/8\text{-}4/8)\overline{\Gamma} - \overline{Y}$	$\langle o, yz|\hat{\ell}_z|u, xz\rangle$
	$\langle u, yz|\hat{\ell}_z|o, xz\rangle$
	$\langle o, x^2 - y^2|\hat{\ell}_z|u, xy\rangle$
$(2/8)\overline{X} - \overline{Y}$	$\langle o, x^2 - y^2|\hat{\ell}_z|u, xy\rangle$
$(6/8)\overline{X} - \overline{Y}$	$\langle o, x^2 - y^2|\hat{\ell}_z|u, xy\rangle$
$(2/8)\overline{X} - \overline{Y}$	$\langle o, xz|\hat{\ell}_z|u, yz\rangle$
$(6/8)\overline{X} - \overline{Y}$	$\langle o, yz|\hat{\ell}_z|u, xz\rangle$
$(4/8)\overline{M} - \overline{X}$	$\langle u, yz|\hat{\ell}_x|o, 3z^2 - r^2\rangle$
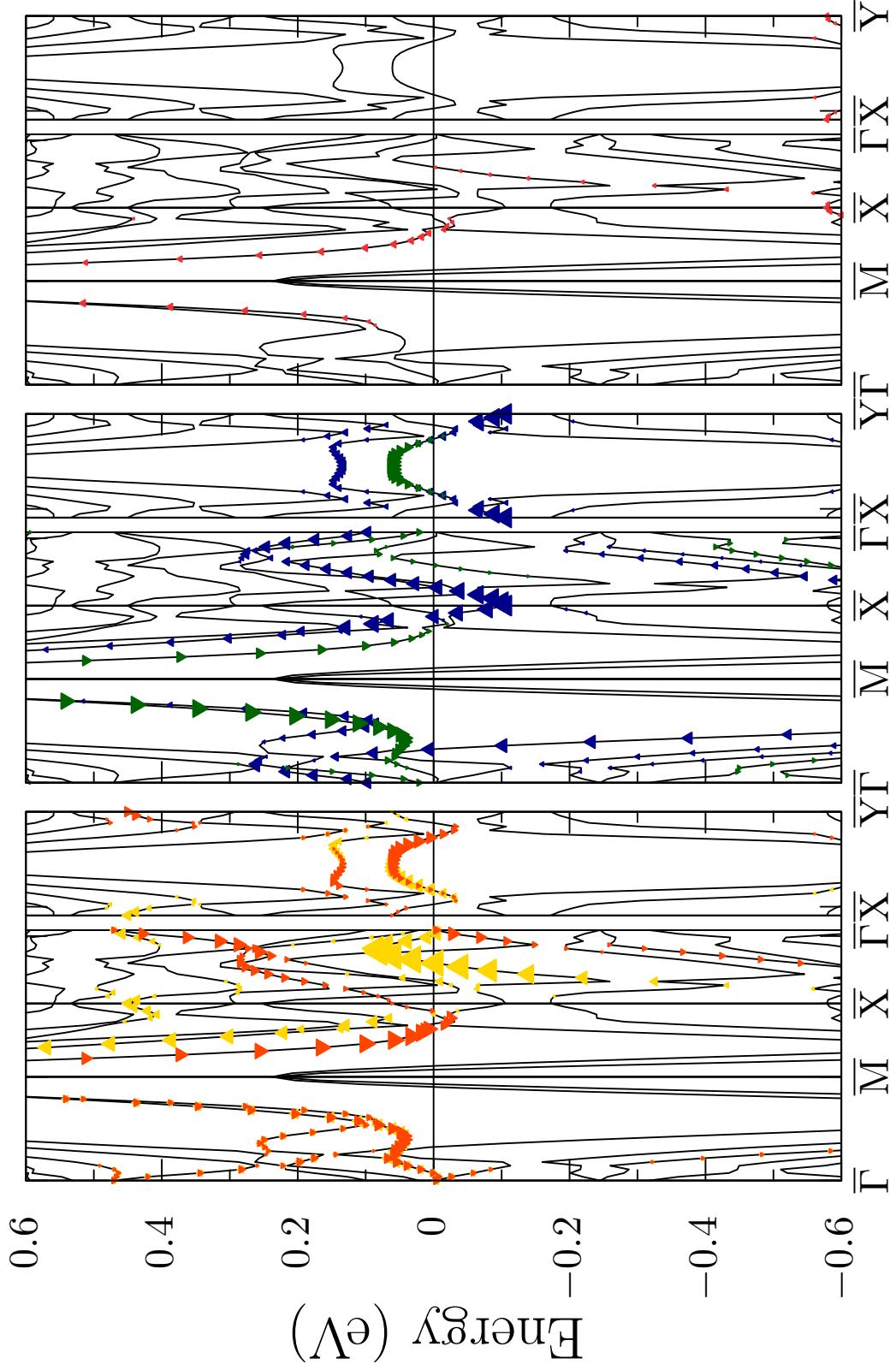
FIGURE 4.4: Partial band dispersions curve of Fe$_1$ for minority spin states in structure-I. The predominant components of Fe 3d orbitals d_{xz}, d_{yz}, $d_{x^2-y^2}$, and d_{xy} are marked as, orange-red filled triangles, gold filled triangles, dark-green filled circles, and dark-blue circles, respectively.
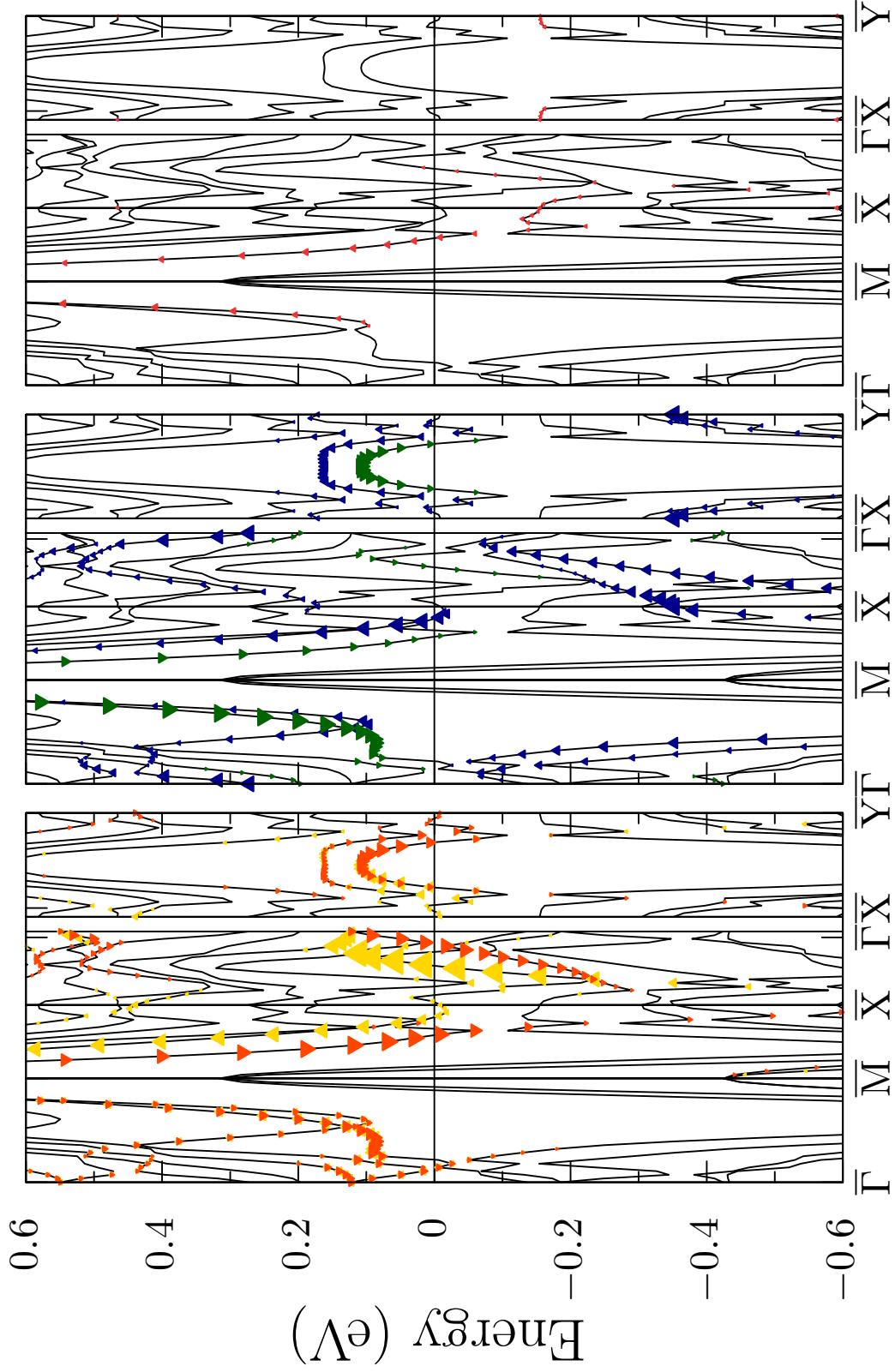
FIGURE 4.5: Partial band dispersions curve of Fe_1 for minority spin states in system-A. The predominant components of Fe $3d$ orbitals d_{xz}, d_{yz}, $d_{x^2-y^2}$, and d_{xy} are marked as, orange-red filled triangles, gold filled circles, dark-green filled triangles, and dark-blue circles, respectively.
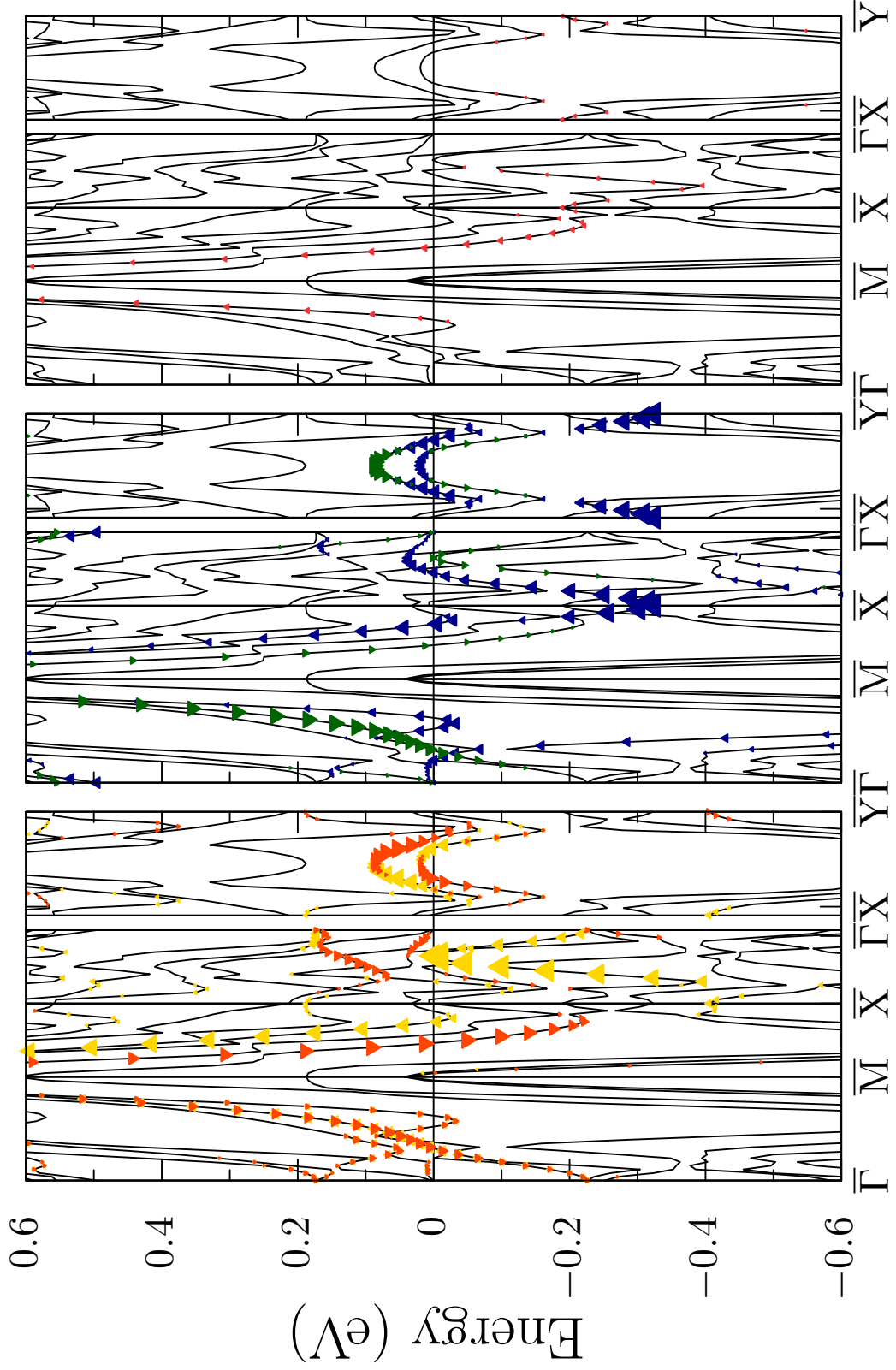
FIGURE 4.6: Partial band dispersions curve of Fe$_1$ for minority spin states in system-B. The predominant components of Fe 3d orbitals d_{xz}, d_{yz}, $d_{x^2-y^2}$, and d_{xy} are marked as, orange-red filled triangles, gold filled circles, dark-green filled triangles, and dark-blue circles, respectively.
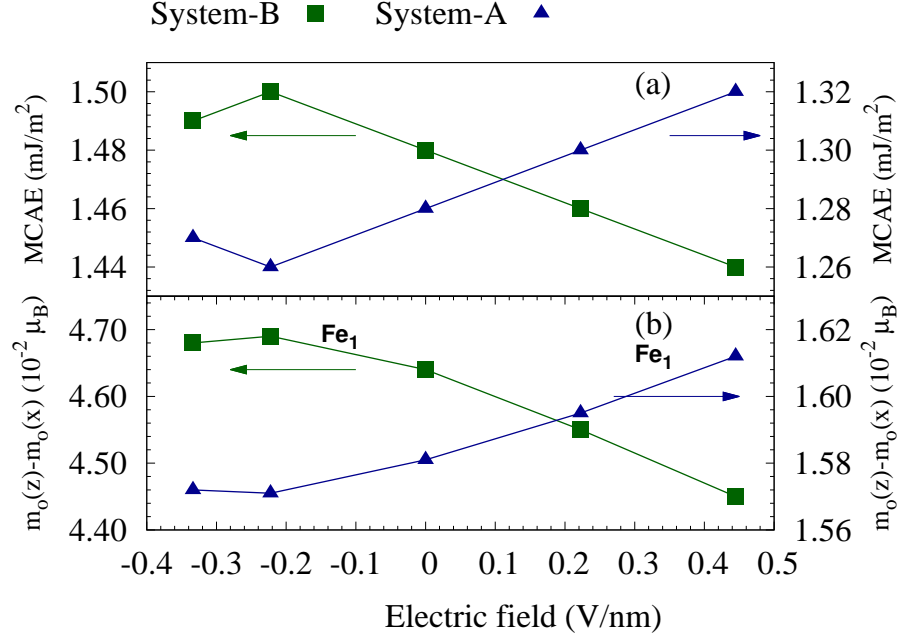
FIGURE 4.7: (a) MCAE and (b) orbital moment differences as EF dependence in system A (blue triangles) and system B (red squares).

Next, we calculated the electric field (EF) effect on MCAE for the system-A and system-B. The results are shown in Fig. 4.7(a). By imposing EF, we observed a different behavior in changes of MCAE. MCAE increases and decreases as EF increases for system A and B, respectively. This behavior leads to an opposite sign in EF coefficient (γ) i.e +89 fJ/Vm and −92 fJ/Vm. This result qualitatively agrees with an orbital moment calculation of Fe/MgO interface (Fe$_1$), as shown in Fig. 4.7(b). MCAE is comparable to the orbital moment as in the Bruno's formula [56], MCAE $= \xi \Delta m_o / 4\mu_B$ where $\Delta m_o = m_o[001] - m_o[100]$ (difference between the out-of-plane and in-plane orbital moments), μ_B is Bohr magneton and ξ is the spin orbit coupling (SOC) constant.

Furthermore, γ value in system-A has the same sign with γ value observed in the experiment [2] , but different sign with system-B. This indicate that, the Cr possible intermix with Fe at the Fe/Cr interface. However, our γ value still underestimated about three times. In the experiment, γ is about 270 fJ/Vm. The possible origin of the difference may come from several factors, such as strain effect, atomic displacement, and complex alloying in the sample.

In order to explain the possible origin of the opposite sign of γ, we investigated the band filling effect for both system-A and system-B. The band filling effect here is refers to the changes of the Fermi level by reducing or increasing the number
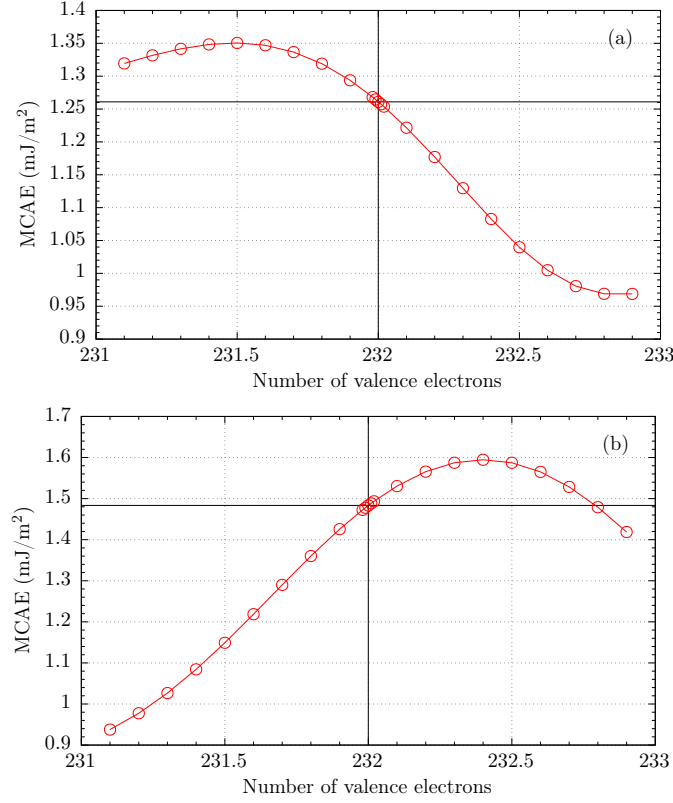
FIGURE 4.8: MCAE as a function of bandfilling. The numbers of valence electrons in the unit cell are indicated by vertical solid lines. (a) system-A and (b) system-B.

of valence electrons (simple rigid-band picture). The results are shown in Fig. 4.8. For the system-A, the MCAE increases with adding the hole to the system, while in the system-B, it decreases. This behavior has a good agreement with the EF effect on MCAE. The behavior in system-A is consistent with the previous calculation [40]. By assuming the number of changes of valence electrons is comparable to the electric field, we estimate the γ from the slope of the curve. By reducing number of valence electron 0.02, the slope estimated to be 16.33 fJ/Vm and -25.48 fJ/Vm for system-A and system-B respectively. The lower γ estimated from the band filling compared to the γ in Fig. 4.7 indicates that EF effect can not fully captured by a simple rigid-band.

To check the change of MCAE for each atom as EF effect, we calculated the atomic MCAE for both zero and under EF. The results are shown in Fig. 4.9. The EF effect almost dominated by Fe_1. This is due to strong screening effect in the surface of metals, so the EF can not deeply penetrate into the bulk of metal [39, 89].
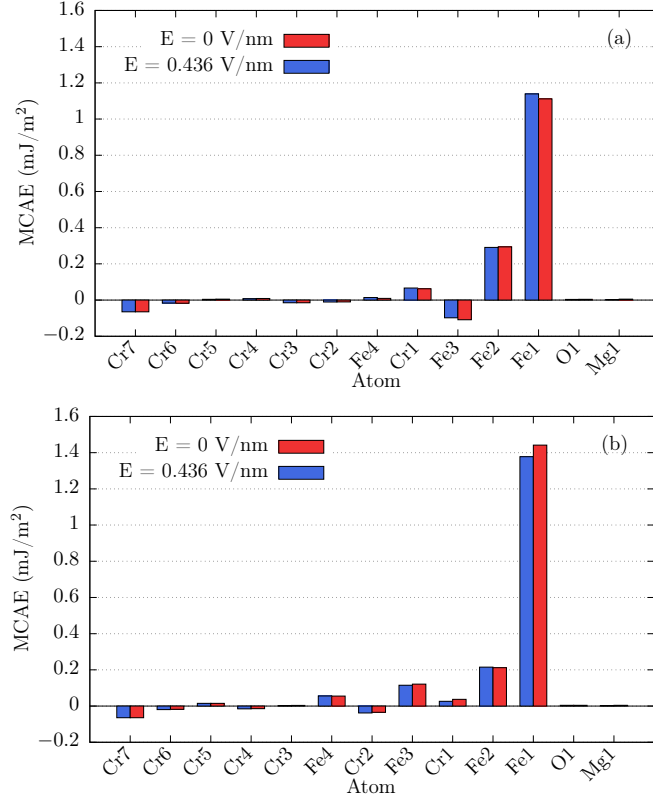
FIGURE 4.9: Atomic resolved MCAE for zero (red bar) and under EF (blue bar), (a) system A and (b) system B.

In addition to the atom resolved MCAE, we also calculate the difference of k-resolved MCAE in zero and under EF. Fig. 4.10(a) and (b) show the k-resolved difference for system-A and system-B, respectively. The discussion of enhancement or suppression of MCAE will be connected to the perturbation analysis in Eq. 2.27 and matrix elements in Table. 2.2 as follows. In system-A, the main enhancement of the MCAE is located at $\overline{\text{M}}$-$\overline{\text{X}}$ line. At zero EF, as in Table 4.4, there is a negative contribution along the $\overline{\text{M}}$-$\overline{\text{X}}$ line. By imposing EF, $d_{x^2-y^2}$ goes up to the higher energy and become unoccupied. This changes may reduce the SOCs of $\langle o, xy|\hat{\ell}_x|u, xz\rangle$, and thus increase the MCAE. On the other hand, for system-B (Fig. 4.10(b)), the reduction of MCAE primarily along the $\overline{\text{X}}$-$\overline{\text{Y}}$ line. We notice that, it can be related to the modulation SOCs of positive contribution as in the Table 4.5. In detail, at the $\overline{\text{X}}$-$\overline{\text{Y}}$ line, after imposing EF, states of $d_{x^2-y^2}$, d_{xz}, and d_{yz} go upward and become unoccupied. This change may decrease the SOCs of $\langle xy||x^2 - y^2\rangle$ and $\langle yz||xz\rangle$) through to $\hat{\ell}_z$ operator and thus decrease the MCAE.

In comparison of the electronic structures of structure-I, system-A and B in Fig. 4.6, we notice that there are three kinds of important characteristics. The first one
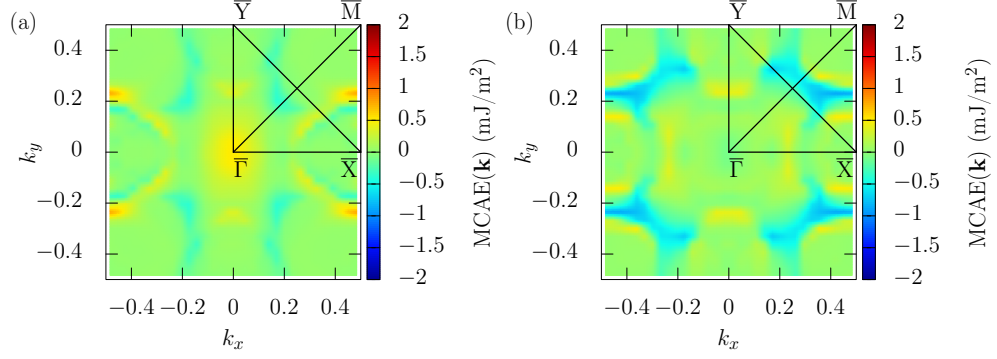
FIGURE 4.10: k-resolved MCAE difference at E=0V/nm and E=0.436V/nm for (a) system A and (b) system B at respectively.

is that the $d_{3z^2-r^2}$ keeps away from the Fermi level. This is due to the orbital hybridization between Fe-$3d_{3z^2-r^2}$ and O-$2p_z$. This hybridization is important origins to get the perpendicular anisotropy [90, 91], since the SOCs $d_{3z^2-r^2}$ contributes to the IPMCAE in the case of large exchange splitting for majority spin state [57]. The second one is, the orbital hybridization between Fe_1 and Fe second layer. As the hybridization raised, the $3d_{xz}$ and $3d_{yz}$ in Fe_1 become split to the lower and higher energies at $\overline{M}$ point. This condition much differ from the case of Fe 1ML, where those states just sit near the Fermi level. The third one is the proximity effect of Fe and Cr. We can see that there is a substantial rearrangement of electronic structure for [Fe/Cr]n (n=1 and 2). Such change can be clearly seen in the partial density of states (PDOS) as shown in Fig. 4.11. d-orbital component of $|m_l| = 2$ and $|m_l| = 1$ which the peak is unoccupied in system-A, become shifted to the lower energy and sit just in the Fermi level for system-B. The proximity effect here is associated with two mechanisms. At first, the hybridization with Cr: Fe d-states are shifted to the lower energy since Cr d-states are located in the higher energy [92]. At second, electrons can transfer from Cr to Fe atoms due to a smaller electronegativity of Cr. Consequently, the number of $3d$ electrons on the Fe of Fe/MgO interface may increase. This increase strongly depends on the vicinity of Cr next to Fe/MgO interface. In addition, we also notice that the number of electrons (NOE) in d-orbital for system-B is increased by 0.052 from that for system-A. This larger NOE may be an origin of sign change in γ. Experimentally, an opposite sign in voltage control magnetic anisotropy (VCMA) was also observed between Ta and Ru underlayers [93]. Discussion of this opposite sign was related to a different spin-orbit coupling in the underlayer, a difference in crystallinity etc., but the origin is still an open question .
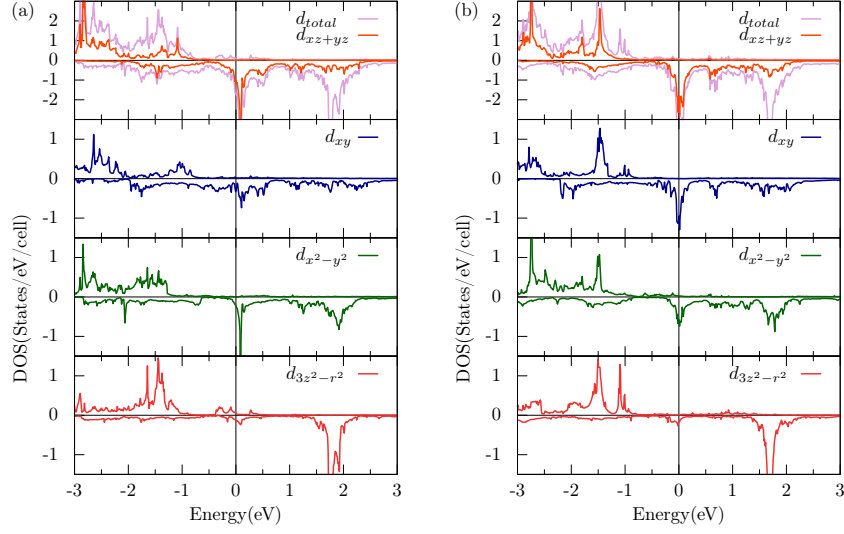
FIGURE 4.11: Projected density of states, (a) system A and (b) system B, respectively.
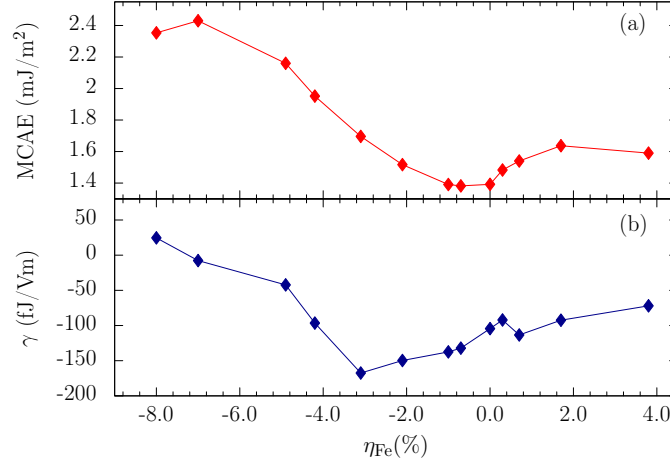
FIGURE 4.12: (a) MCAE and (b) electric-field induced MCAE coefficient (γ) in system B as strain depedence.

4.1.2 MCAE and EF control MCAE in Fe/Cr Intermixing as Strain Dependence

For further exploration at vicinity of the Fermi level, we calculated MCAE as strain dependence for system-B, as shown in Fig. 4.12(a). In this work, the variation of strain is taken in the range of -8.0% to 3.8% for the ratio with respect to Fe lattice constant (2.87Å). As a result, MCAE increases with increasing tensile strain (increase in lattice constant) and increasing compressive strain (reduce in lattice constant) with the maximum value of 2.43 mJ/m^2.
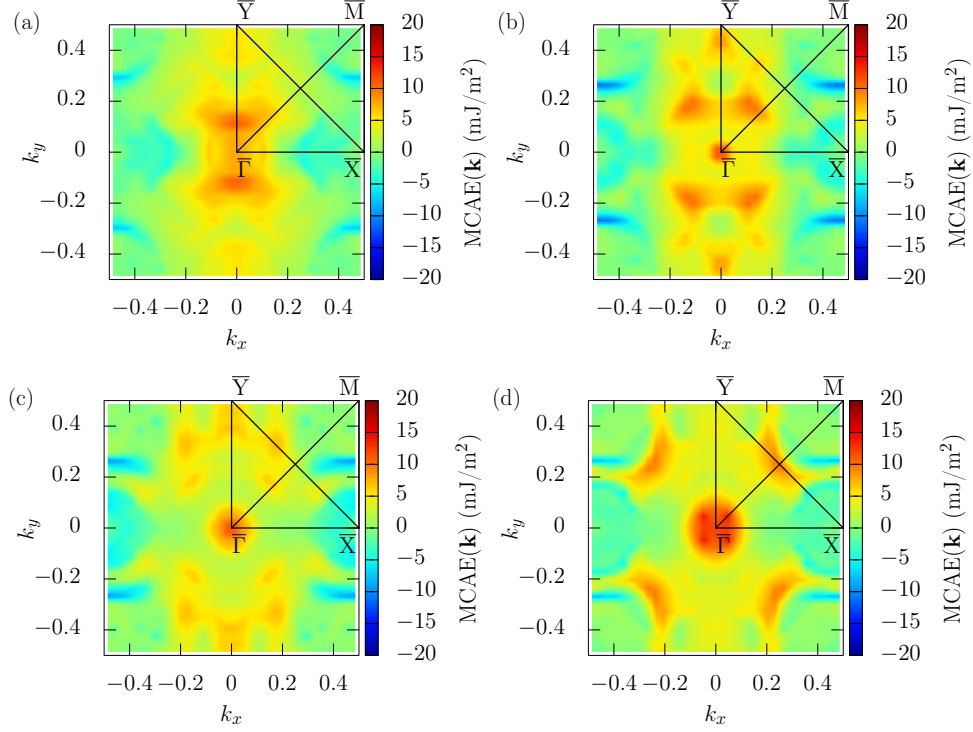
FIGURE 4.13: k-resolved MCAE in system B for (a) η_{Fe}=3.8%, (b) η_{Fe}=0.3%, (c) η_{Fe}=−3.1%, and (d) η_{Fe}=−8%.

To elucidate the mechanism of strain on the enhancement of MCAE at zero EF, we calculate the k-resolved MCAE, as shown in Fig. 4.13. We can see that the main change of MCAE located at $\overline{\Gamma}$ point and along the $\overline{\text{X}}$-$\overline{\text{Y}}$ line. Furthermore, the atom k-resolved MCAE shows that the enhancement at $\overline{\text{X}}$-$\overline{\text{Y}}$ line comes from Fe_1, while the enhancement $\overline{\Gamma}$ point originates from Fe atoms inside (Fe_2, Fe_3, and Fe_4).

This MCAE is strongly related to the SOCs of d-orbital component on the interface Fe, especially those of eigen-states near the Fermi level. The behavior is shown in the partial DOS (Fig. 4.14). By increasing compressive strain, $d_{x^2-y^2}$ and part of d_{xz}, d_{yz} gradually shifted to the lower energy and become below the Fermi level while d_{xy} and part of d_{xz}, d_{yz} stay above the Fermi level (Fig. 4.14(a) and 4.14(b)). This kind of coupling may increase the MAE due to SOC of $\langle xy||x^2-y^2\rangle$ and $\langle yz||xz\rangle$ through to the $\hat{\ell}_z$ operator. On the other hand, by increasing tensile strain such mechanism also appears, but it is a reverse. At $\overline{\text{X}}$-$\overline{\text{Y}}$ line, d_{xy} and part of d_{xz}, d_{yz}, are also push down to the lower energy and become occupied while $d_{x^2-y^2}$ and part of d_{xz}, d_{yz} stay above the Fermi level (Fig. 4.14(d)). Again, such coupling may also increase the MCAE through to $\hat{\ell}_z$ operator as in the previous one. These changes mainly appear at $\overline{\text{X}}$-$\overline{\text{Y}}$ line as shown in the Fig. 4.15.
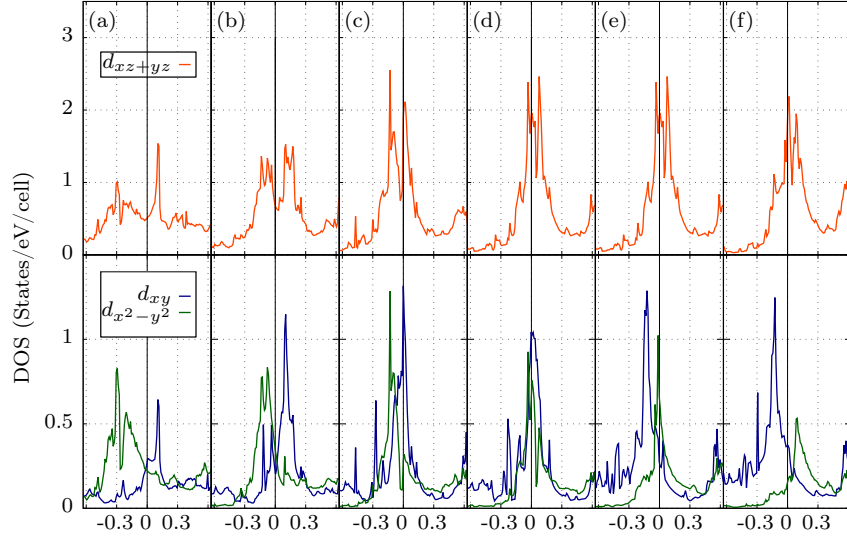
FIGURE 4.14: PDOS in system B for (a) $\eta_{\text{Fe}}=-8\%$, (b) $\eta_{\text{Fe}}=-3.1\%$, (c) $\eta_{\text{Fe}}=1\%$, (d) $\eta_{\text{Fe}}=0.0\%$, (e) $\eta_{\text{Fe}}=1.7\%$, and (f) $\eta_{\text{Fe}}=3.8\%$.
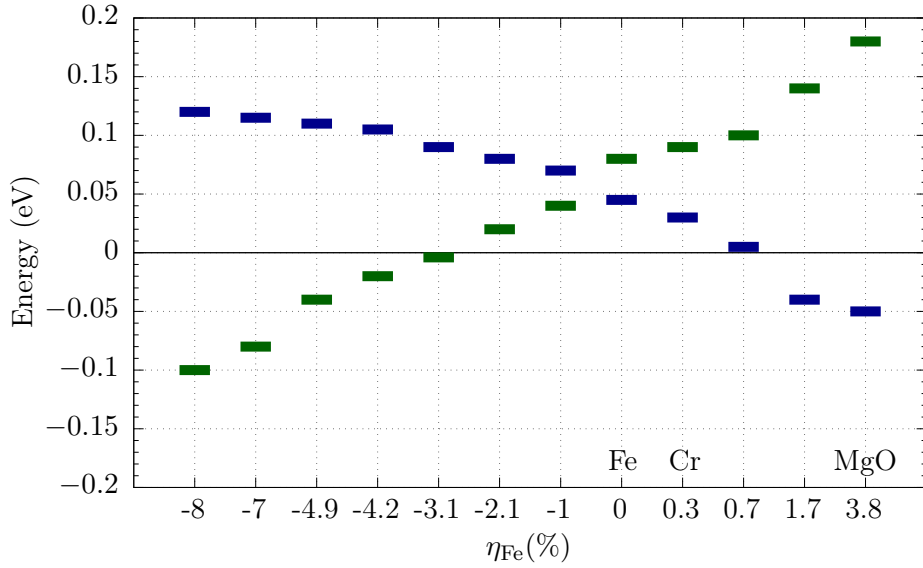
FIGURE 4.15: Energy of orbitals $d_{x^2-y^2}$ (green) and d_{xy} (blue) along the $\overline{\text{X}}$-$\overline{\text{Y}}$ line.

The total number of $3d$ electrons (NOE) as a strain dependence is shown in Fig. 4.14(a). Generally, the total NOE decreases (increases) by increasing tensile (compressive) strain. In more detail, the NOE of each d-orbital component is shown in Fig. 4.14(b). The behavior of total NOE as a strain dependence is related to NOEs of d_{yz+xz} and $d_{x^2-y^2}$. The increase of in-plane lattice constant may reduce the interlayer distance along z-direction. This mechanism may enhance the hybridization between Fe, resulting in a strong bonding which leads to the delocalization of electrons and finally reduces the NOE of d-orbital.
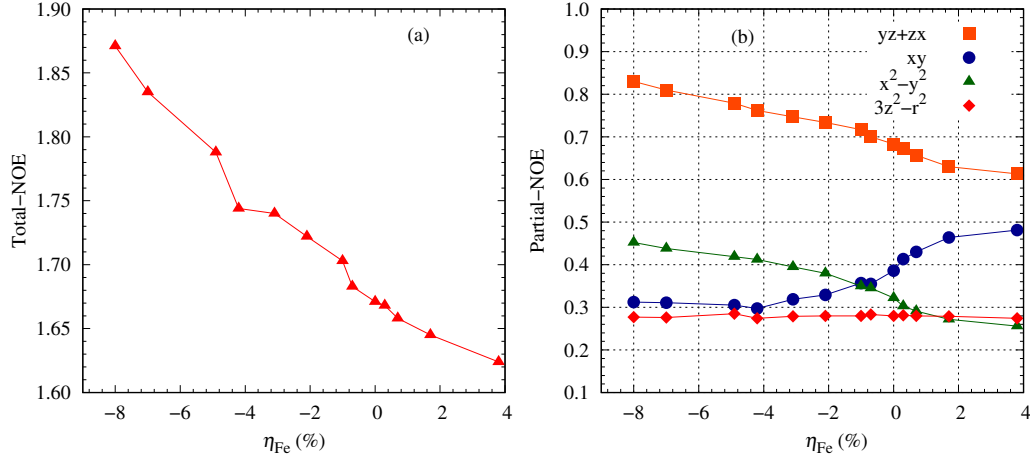
FIGURE 4.16: NOE of 3d on the Fe/MgO interface as a strain dependence. (a) Total-NOE and (b) partial NOE of each orbital.

Furthermore, the electric field (EF) coefficient (γ) as strain dependence is shown in Fig. 4.12(b). The maximum absolute value of γ is 170 fJ/Vm at $\eta_{Fe}=-3.1\%$. To discuss such a maximum value, we calculate the atomic resolved at zero and under EF as shown in Fig. 4.17(a). We found the main change of MCAE induce by EF appear at Fe_1. The behavior of MCAE changes also can captured by band filling calculation as shown in Fig. 4.17(b).

Large γ at $\eta_{Fe}=-3.1\%$ may be related to a large amount of d-orbital states around the Fermi level. As shown in Fig. 4.18(a), at zero EF, $d_{x^2-y^2}$ and part of d_{xz}, d_{yz} occupy and form states just at the Fermi level. After applying EF, these states are shifted to the higher energy and become unoccupied. This change may reduce the SOCs of $\langle xy||x^2-y^2 \rangle$ and $\langle yz||xz \rangle$ through to $\hat{\ell}_z$ operator. Due to this reduction the MCAE may reduce significantly, resulting in a larger MCAE change. Such remarkable changes clearly observed at k-resolved difference (ΔMCAE($\mathbf{k}$)) as shown in the Fig. 4.18(b).

4.2 Shape Magnetic Anisotropy From Spin Density in Nanoscale Slab Systems

Another important contribution to the MAE as well as spin orbit coupling is shape anisotropy. Both contribution should be consider in the design of materials fo the application such as memory or sensor [2, 94], or for emerging new phenomena [95,
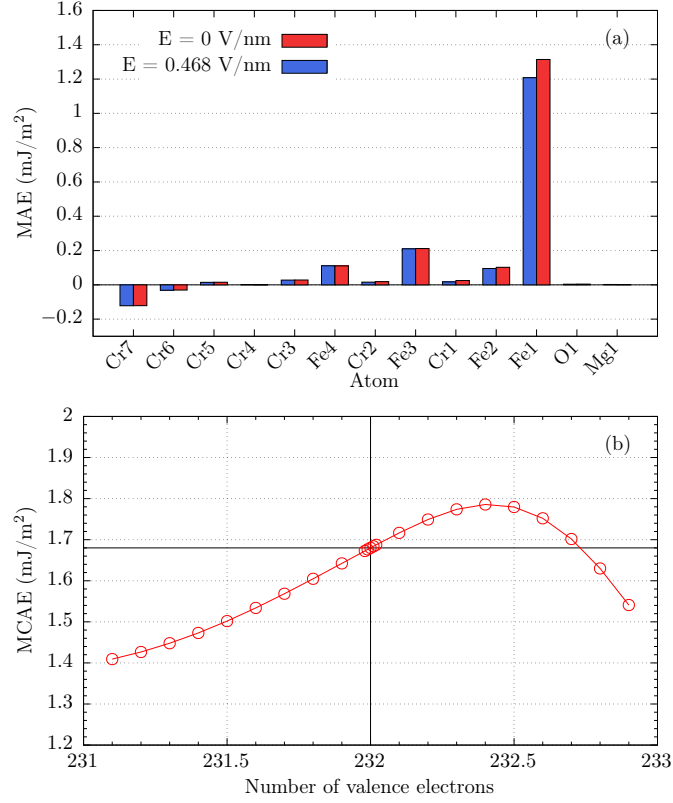
FIGURE 4.17: (a) Atomic resolved MCAE for zero (red bar) and under EF (blue bar) and (b) MCAE as a function of band-filling in system B for η_{Fe}=−3.1%. The numbers of valence electrons in the unit cell are indicated by vertical solid lines.

96]. In this section, we investigate the shape magnetic anisotropy energy (SMAE) using the continuum approach (CA) [80], discrete approach (DA), and soin density approach (SDA) [79]. The CA uses the data of total magnetization and parameter of the slab thickness. The SMAE fron CA given by SMAE(CA)= $\mu_0 M^2/2\Omega$, where μ_0, M, and Ω are the vacuum permeability, total magnetic moment, and slab volume, respectively. The DA uses the data of the atomic magnetic moments extracted from the spin density. The SDA reflects the shape of the general spin density distribution. The formula for DA and SDA are written in the theoretical framework.

4.2.1 SMAE in Ferromagnetic Slabs

We investigated the MAE of MgO(5ML)/Fe(xML)/ MgO(5ML) (x=1–10) slab with the in-plane lattice constant extracted from MgO. This slab has vacuum layers of 0.9 nm thick on both the sides of the layer. The structure is shown in
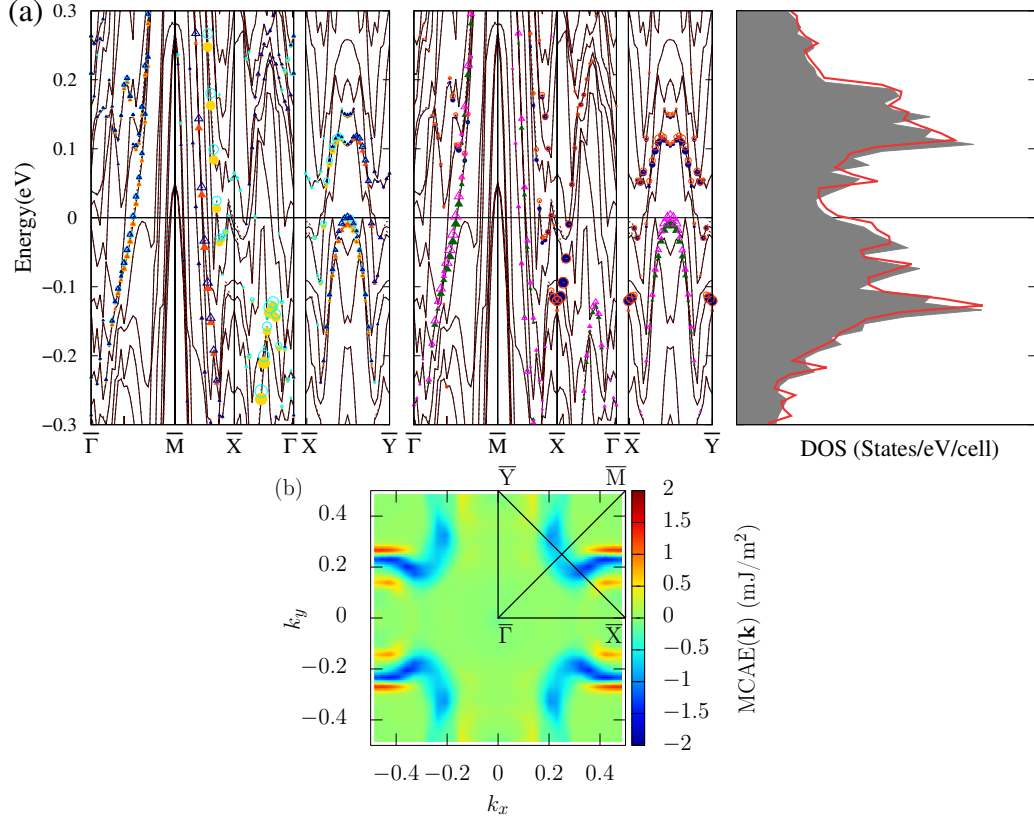
FIGURE 4.18: (a) Band dispersion curve and densities of states (DOS) for η_{Fe}=-3.1% for zero EF (solid curve) and 0.436 V/nm (dotted curve). In the zero EF (0.436 V/nm), the predominant components of Fe 3d orbitals (d_{xz}, d_{yz}, $d_{x^2-y^2}$, d_{xy}) for minority spin-states are marked as, orange-red filled (dark-blue empty) triangels, gold filled (cyan empty) circles, dark-green filled (magenta empty) triangels, and dark-blue (orange-red empty) circles respectively. The shaded (gray) curves and solid (red) lines of DOS indicate zero and under EF respectively. (b) ΔMCAE(**k**) of E=0V/nm and E=0.468V/nm for η_{Fe}=-3.1%.

Fig. 4.19(a). After the relaxation of layer distances, we estimated the SMAEs for CA, DA, and SDA. The midpoint-to-midpoint layer distance between the Fe/MgO interfaces was taken as layer thickness. In order to identify the difference between the surface and interface effects, we also evaluated the MAE of a Fe(xML) slab obtained by deleting the MgO layers from the MgO/Fe(xML)/MgO slab. The structure is shown in Fig. 4.19(b).

The results of SMAEs for CA, DA, and SDA of MgO(5ML)/Fe(xML)/MgO(5ML) (x=1−10) and Fe(xML) (x=1−10) are shown in 4.20(a) and (b), respectively. From Fig. 4.20(a) and (b), we extract the interface/surface effect (intersection of the fitted line) and the bulk-like property (slope of the fitted line). The results are summarize in Table. 4.6 and Table. 4.7, respectively.
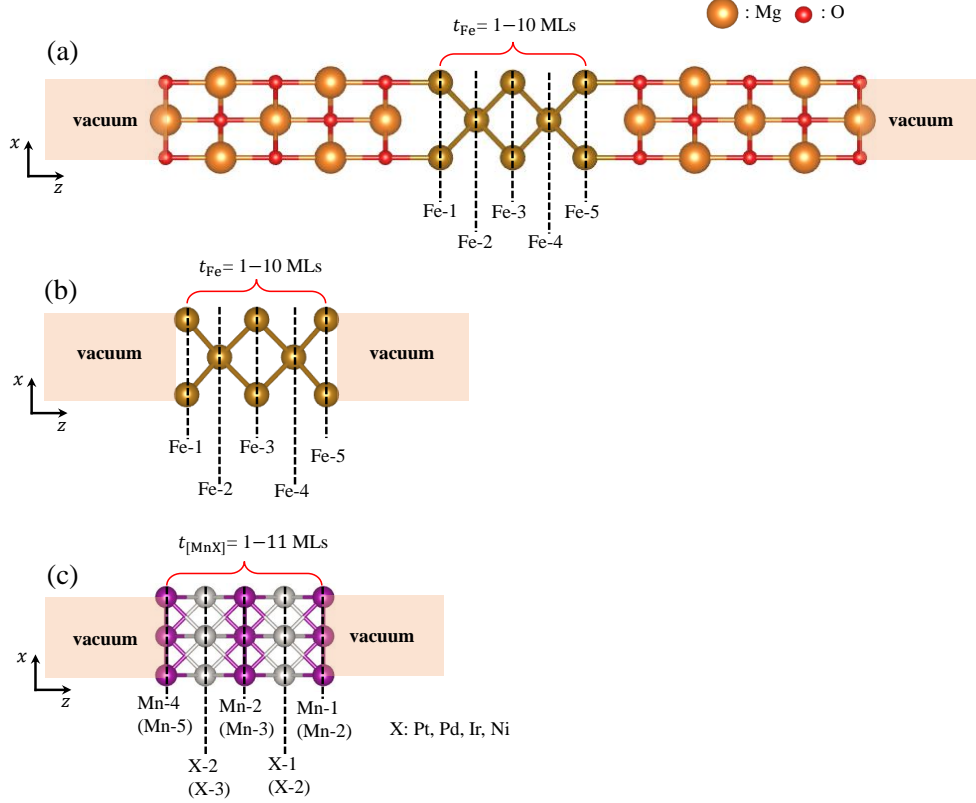
FIGURE 4.19: Model structure for shape anisotropy calculation. (a) MgO/Fe/MgO systems, (b) Fe-systems, and (c) MnX systems (X: Pt, Pd, Ir, and Ni).

TABLE 4.6: Interface/surface effect (intersection of fitted line). CA, DA, and SDA represent continuum approach, discrete approach, and spin density approach. In the case of CA, we use t:exp (Fe thickness extracted from the experiment) and t:theo (Fe thickness from the optimized structure). The experimental data was taken from ref. [2]. CA, DA, and SDA are in the unit of mJ/m^2.

System	CA(t:exp)	CA(t:theo)	DA	SDA
MgO/Fe/MgO	0.220	0.002	0.056	-0.107
Fe	0.278	0.011	0.104	-0.062

Our results are similar to the data of demagnetization energy in the previous work [91]. As shown in Table. 4.20, the CA tends to provide larger values of MAEs (E_{CA}), namely, a stronger in-plane anisotropy. In contrast, E_{SDA} is reduced by the surface/interface effect. This reduction is estimated by the difference between the intersections of linear fitting lines to be 0.163 and 0.166 mJ/m^2 for the slabs of MgO/Fe(xML)/MgO and Fe(xML), respectively. Similarity between these values tends to hide the difference between the interface effect of Fe/MgO and the surface effect of Fe layer. When comparing the intersections of the DA and SDA,

TABLE 4.7: Bulk-like property (slope of the fitted line). CA, DA, and SDA represent continuum approach, discrete approach, and spin density approach. In the case of CA, we use t:exp (Fe thickness extracted from the experiment) and t:theo (Fe thickness from the optimized structure). The experimental data was taken from ref. [2]. CA, DA, and SDA are in the unit of mJ/m^2/Å.

System	CA(t:exp)	CA(t:theo)	DA	SDA
MgO/Fe/MgO	0.238	0.238	0.234	0.233
Fe	0.241	0.238	0.237	0.236
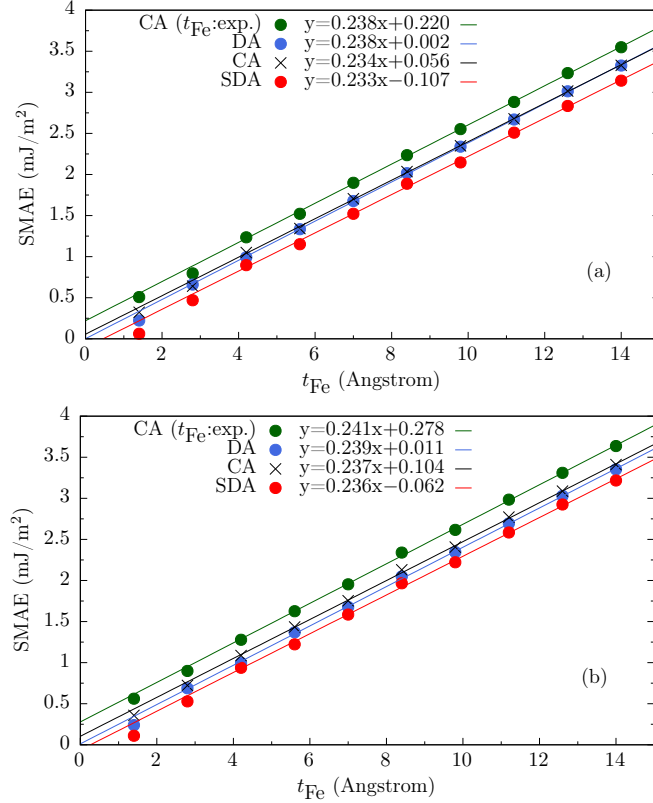
FIGURE 4.20: SMAE of (a) MgO/Fe(xML)/MgO and (b) Fe(xML) (x=1−10) for CA, DA, and SDA. The CA with the experimental thickness (0.14 nm/FeML) is also plotted. The lines are deduced from the least square fitting using the data of x=3−10.

the corresponding differences are 0.109 and 0.073 mJ/m^2, indicating the difference between the interface and surface effects. The increasing rate of MAE with respect to the thickness, namely, the slope of linear fitting line in Fig. 4.20 and summarized in Table. 4.7 does not vary with a large amount among the results of CA, DA, and SDA. This is due to the fact that the spin density distribution on the magnetic atom inside the layer (not at the interface/surface) has few quadrupole components.

Such quadrupole contribution is only observed in the interface layer. In Fig.
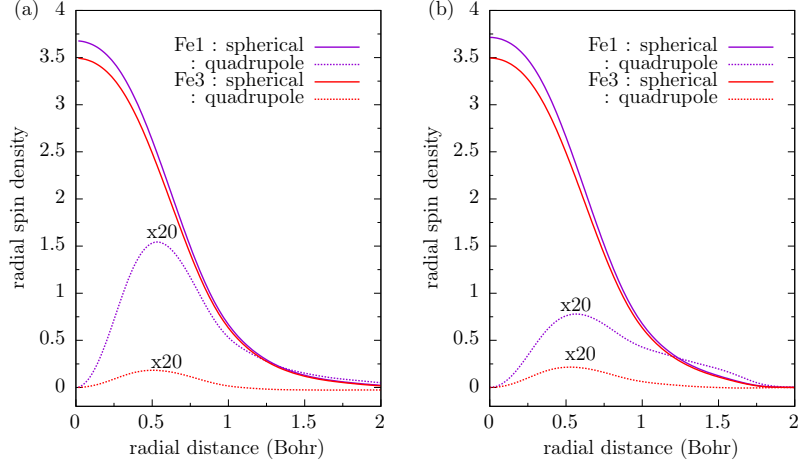
FIGURE 4.21: Radial atomic spin density distribution [in $(\text{Bohr})^{-3}$] in (a) MgO/Fe(5ML)/MgO and (b) Fe(5ML). Fe1 indicate the interface/surface atoms, and Fe3 indicate the atoms inside the layer. All the quadrupole components are magnified 20 times.

4.21(a) and (b) the radial spin density distributions of spherical and quadrupole components are shown for the atoms on the interface and inside the layer. On the inside, the quadrupole component is reduced significantly compared with that on the interface. In addition, from Fig. 4.21(a) and (b), we can see that MgO/Fe(xML)/MgO has larger quadrupole component compared to the Fe(xML). As a result, the reduction of SMAE(SDA) from SMAE(CA) in MgO/Fe(xML)/MgO becomes larger.

4.2.2 SMAE in Antiferromagnetics Slabs

Next, we investigated the MAE originating from the magnetic dipole interaction in a MnX slabs (X=Pt, Ir, Pd, and Ni) extracted from the bulk with L1$_0$ ordered alloy. Assuming that an antiferromagnetic configuration is the same as in the bulk, where the total magnetization in the same Mn-atom layer vanishes and the atomic magnetic moments are parallel to those of the nearest-neighboring Mn layers, the DA and SDA were applied to several thicknesses (tML) with a (001) surface. The structure are shown in the Fig. 4.19(c). The CA provides no contribution of MAE due to no magnetization. In the evaluations of E$_D$A and E$_S$DA, a $\sqrt{2} \times \sqrt{2}$ magnetic unit cell was taken for an in-plane periodicity with the lattice constant of 7.56 Bohr, 7.28 Bohr, 7.69 Bohr, 7.07 Bohr for MnPt, MnIr, MnPd, and MnNi, respectively. These were an experimental bulk value.

TABLE 4.8: Interface/surface effect (intersection of fitted line) for antiferromagnetics MnX systems (X: Pt, Ir, Pd, Ni). DA, and SDA represent discrete approach, and spin density approach. DA, and SDA are in the unit of mJ/m^2.

System	DA	SDA
MnPt (odd)	-0.088	-0.228
MnPt (even)	0.041	-0.012
MnIr (odd)	-0.143	-0.317
MnPd (odd)	-0.068	-0.178
MnNi (odd)	-0.124	-0.295

TABLE 4.9: Bulk-like property (slope of the fitted line) for antiferromagnetics MnX systems (X: Pt, Ir, Pd, Ni). DA, and SDA represent discrete approach and spin density approach. The values are in the unit of $mJ/m^2/ML$.

System	DA	SDA
MnPt (odd)	-0.085	-0.092
MnPt (even)	-0.088	-0.095
MnIr (odd)	-0.069	-0.058
MnPd (odd)	-0.087	-0.103
MnNi (odd)	-0.096	-0.114

The results of SMAE calculation from DA and SDA for each system are shown in the Fig. 4.22. As shown in Fig. 4.22, the negative signs indicate a perpendicular magnetic anisotropy. This perpendicular anisotropy is attributed to the antiferromagnetic spin alignment in each Mn layer. Furthermore, from Fig. 4.22, we extract the interface/surface effect and bulk-like property. The results are summarized in Table. 4.8 and Table. 4.9.

The absolute of E_{SDA} is larger than of E_{DA} for each system. Surface effects on the spin density distribution are clearly shown at the intersections of fitted linear lines between E_{DA} and E_{SDAsho} as listed in Table. 4.8. For all systems, MnIr has the largest intersection constant. The reason why the absolute of E_{SDA} is larger than of E_{DA} is that the quadrupole component of atomic spin density distribution on the surface magnetic atom enhances the MAE. Such quadrupole component of atomic spin density distribution on the surface Mn atom (Mn2) for each system is shown in Fig. 4.23.

In addition, from the Table. 4.9, we can see that, there are a difference between the SDA and DA. In odd case, the differences are 0.007 $mJ/m^2/ML$, 0.011 $mJ/m^2/ML$, 0.016 $mJ/m^2/ML$, and 0.018 $mJ/m^2/ML$ for MnPt, MnIr, MnPd and MnNi, respectively. Those values are small but not negligible, originating from

TABLE 4.10: The MAE of bulk antiferromagnetic MnX systems (X: Pt, Ir, Pd, Ni). The MDIE evaluated from spin density approach (SDA). All the MAE values are in the unit of meV/cell

System	a(Å)	c/a	MAE		MAE(SOI+SDA)	MAE(SOI [97]
			SOI	SDA		
MnPt	3.990	0.918	0.201	0.188	0.389	0.510
MnIr	3.885	0.945	-8.204	0.105	-8.100	-7.050
MnPd	4.070	0.880	-0.419	0.218	-0.202	-0.570
MnNi	3.740	0.941	-0.448	0.202	-0.46	-0.290

TABLE 4.11: The comparison of SDA in AFM MnX systems from the bulk calculation and the bulk-like property estimated from the slope in Fig. 4.22.

System	a(Å)	SDA(Bulk calculation) (meV/ML)	SDA (Bulk-like property) (meV/ML)
MnPt	3.990	0.093	0.094
MnIr	3.885	0.053	0.052
MnPd	4.070	0.103	0.109
MnNi	3.740	0.098	0.101

the quadrupole component on Mn atom inside the layer (not on the surface). Such quadrupole component of Mn inside the layer (Mn4) are shown in Fig. 4.23.

For the comparison, we also calculated the MAE for bulk antiferromagnetic MnX systems (X: Pt, Ir, Pd, Ni) originated from SOI and MDIE. The structure is shown in Fig. 4.24. The MDIE evaluated using the SDA approach. The results are summarized in the Table. 4.10. The SDA in Table. 4.10 has a good agreement with the bulk-like property from the slope summarized in Table. 4.9 and the result is summarized in Table. 4.11.
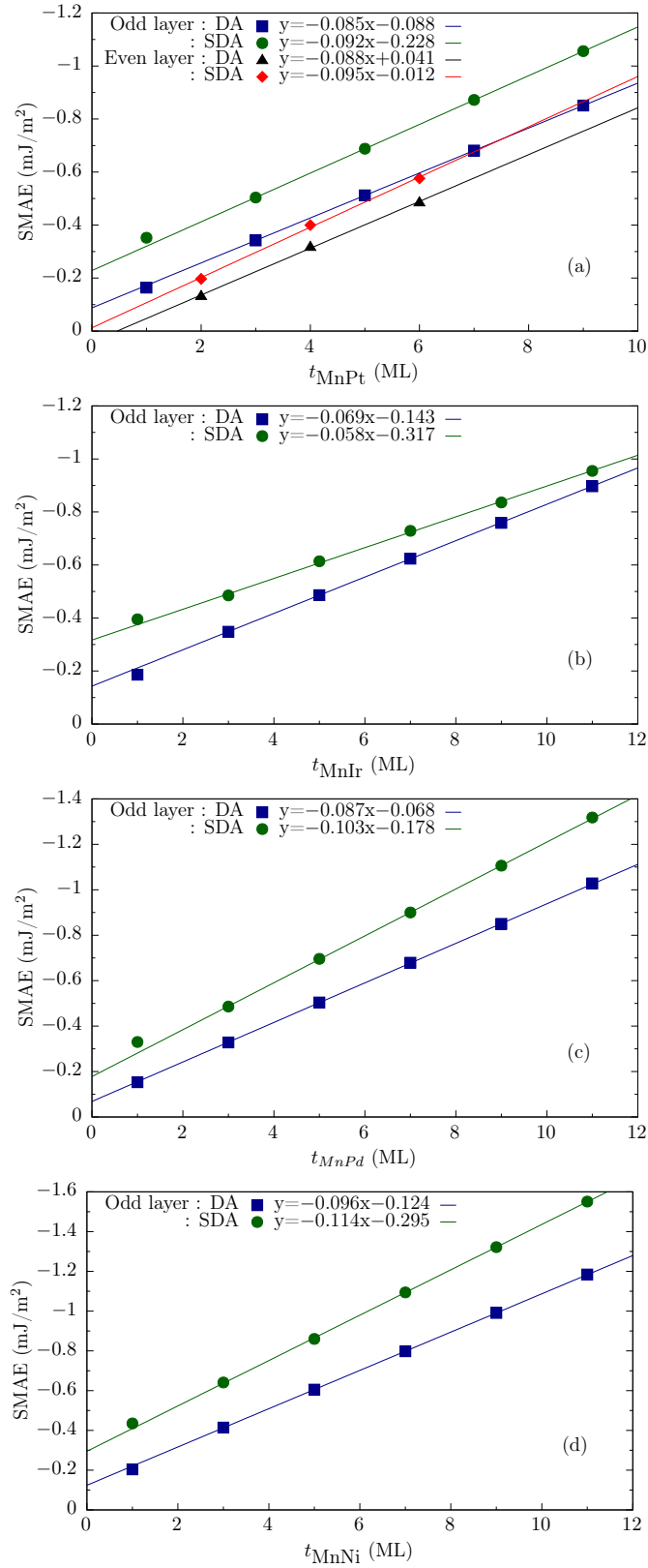
FIGURE 4.22: SMAE of antiferromagnetics MnX slabs (a) X=Pt, (b) X=Ir, (c) X=Pd, and (d) X=Ni. Mn atomic monolayer (t=1), $[MnX]_{(t-1)/2}$/Mn (odd layer), and $[MnX]_{t/2}$ (even layer). The data of t=1 were not used for the linear fitting.
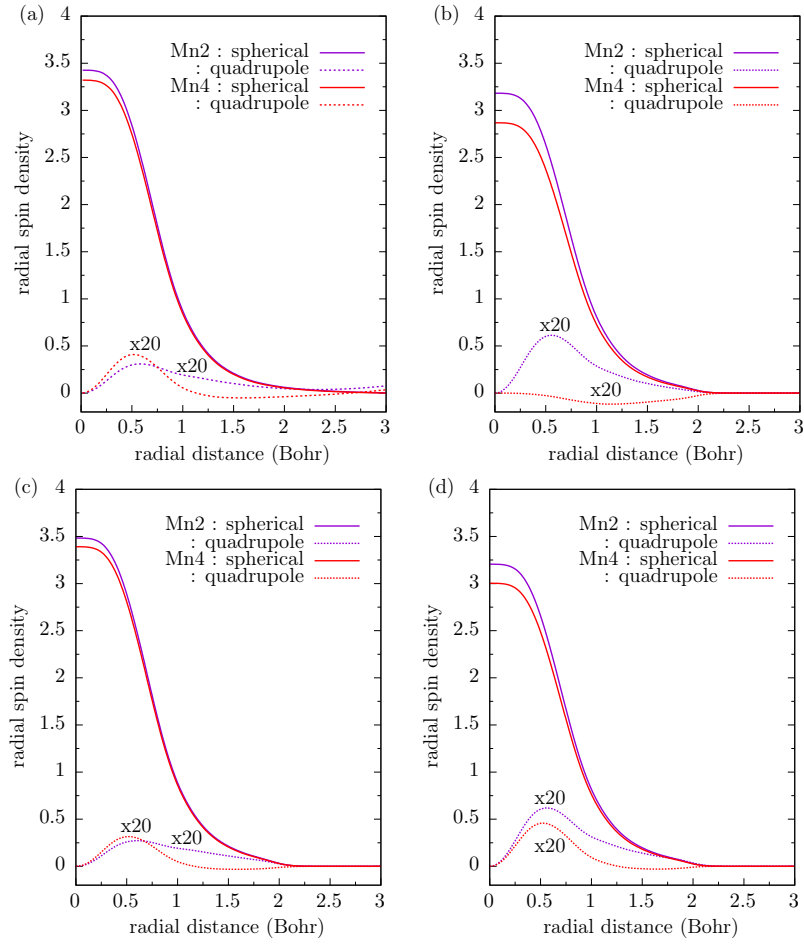
FIGURE 4.23: Radial atomic spin density distribution $[\text{in(Bohr)}^{-3}]$ in antiferromagnetics MnX slabs for t=5MLs (a) X=Pt, (b) X=Ir, (c) X=Pd, and (d) X=Ni.
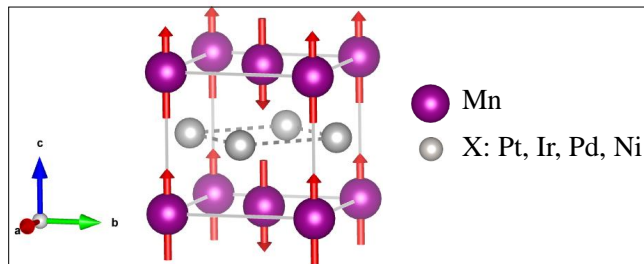
FIGURE 4.24: Model structure bulk antiferromagnetic MnX systems (X: Pt, Ir, Pd, Ni).

Chapter 5

Summary and Outlook

5.1 Summary

As was introduced in Section 1.2, the focus on this dissertation has been on investigation of magnetic properties, such as magnetic anisotropy energy (MAE) based on the spin density functional theory (SDFT) scheme. In particular, two topics have been considered. The first one is effect of alloying, strain, and electric field (EF) on MAE and the second one is MAE contribution from shape magnetic anisotropy in the material which has a ferromagnetic and antiferromagnetic structure.

In the calculation, we considered two kinds of contribution to the MAE, namely magnetocrystalline anisotropy energy (MCAE) originating from spin-orbit coupling (SOC) and shape magnetic anisotropy energy (SMAE) originating from magnetic dipole-dipole interaction (MDI). The MCAE part was calculated in the basis of the total energy (TE) and grand canonical force theorem (GCFT). In the GCFT scheme, we performed the atom-resolved and $k-$resolved contribution the MCAE. For the SMAE contribution, we estimated by using the continuum approach (CA), discrete approach (DA), and spin density approach (SDA). In SDA approach, we evaluated the atomic multipole spin density, such as quadrupole component.

In the first topic, we studied the MAE in the Cr/Fe/MgO structure with introducing the Fe/Cr alloying. Such alloying is based on the suggestion from the experimetal measurement [2]. An alloying of $[\text{Fe}/\text{Cr}]_n$ (n=1,2) has been considered. For n=1 and n=2, we called system-A and system-B, respectively. For a

comparison, a structure without alloying was also considered (structure-I). From the TE calculation, the MCAEs in system-A and system-B were largely enhanced, compared to those of structure-I, as summarized in Table. 4.1, Sec. Section 4.1.1. Next, Combining with the MDIE, the perpendicular MAE (PMAE) was observed for system-A and system-B, respectively, while for structure-I showed in-plane MAE (IMAE). The result in system-A or system-B has a qualitative aggrement with the MAE observed in experiment [2]. To elucidate the possible origin of enhancement of MAE, we systematically analyzed the MCAE in GCFT scheme. At first, we confirm that the MCAE calculated from TE and GCFT has a good agreement, as summarized at Table. 4.2, in Section 4.1.1. This aggrement allows us for further analysis of atom resolved or k-resolved MCAE.

The atom-resolved MCAE showed that the main positive contribution to the MCAE is originated from (Fe_1). Furthermore, from k-resolved MCAE result, we can clearly see the region in two dimensional first Brillouin zone (2DBZ) which contributes to the positive or negative MCAE. In the basis of the analysis in Section 2.2.2, we summarized the list of possible pair coupling of the d-orbitals near the Fermi energy as shown in Tables 4.3, 4.4, and 4.5 for structure-I, system-A, and, system-B, respectively.

Next, we calculated the EF effect for system-A and system-B. We observed an opposite sign of MCAE coefficient (γ), which is positive and negative for system-A and system-B, respectively (Fig. 4.7, section 4.1.1). The orbital moment and band filling calculation also showed the same behavior. From atom resolved analysis, we found that MCAE changes by EF mainly observed at Fe_1. Moreover, from different of k-resolved MCAE at zero and with EF ($\Delta MCA(k)$), we can clearly see that the figure show a positive for system-A, while negative for system-B.

The enhacement of MCAE and opposite sign in γ maybe related to the impact of Fe/Cr alloying whichs make a remarkable change in the electronic structure, especially, Fe interface with MgO (Fe_1). Here, we addres that such changes maybe related to the proximity effect of Fe and Cr. The proximity effect is assosiated with two mechanisms. At first, the hybridization with Cr: Fe d-states are shifted to the lower energy since Cr d-states are located in the higher energy [92]. At second, electrons can transfer from Cr to Fe atoms due to a smaller electronegativity of Cr. Consequently, the number of $3d$ electrons on the Fe of Fe/MgO interface may increase. This increase strongly depends on the vicinity of Cr next to Fe/MgO

interface. In addition, we also notice that the number of electrons (NOE) in d-orbital for system-B is increased by 0.052 from that for system-A. This larger change in NOE may be an origin of sign change in γ.

In the vicinity of the Fermi energy, we calculated the MCAE in system-B as strain dependence with respect to the Fe lattice constant (η_{Fe}). The MCAE increases with the increasing tensile strain (increase in lattice constant) and increasing compressive strain (reduce in lattice constant) with the maximum value of 2.43 mJ/m^2 at $\eta_{\text{Fe}} = 2\%$. (Fig. 4.12(a), section 4.1.2). To elucidate the possible origin, we systematically analyzed the k-resolved MCAE and compared with the electronic structure. We notice that the behavior of MCAE as strain depedence may be related to the pair coupling of $d_{x^2-y^2}$ and d_{xy} along the $\overline{\text{X}}$-$\overline{\text{Y}}$ line, as shown at Fig. 4.15. Furthermore, the larger MCAE at $\eta_{\text{Fe}} = -8\%$ may be related to the large amount of state in the Fermi energy and suitable pair coupling which promotes to the PMCAE. In adition, in the basis of atom resolved MCAE, we found that, by introducing compressive strain, the Fe inside the layer also contributes to the PMCAE. Next, we calculated the EF effect on MCAE for each starin condition. The maximum value of γ=170 fJ/Vm was achieved at $\eta_{\text{Fe}} = -3.1\%$. The Larger γ at $\eta_{\text{Fe}} = -3.1\%$ is related to the large amount of d-orbital states (d_{xz}, d_{yz}, $d_{x^2-y^2}$, d_{xy}) along the $\overline{\text{X}}$-$\overline{\text{Y}}$ (Fig. 4.18(a)). As a result, the small change in orbital occupation induce by EF, may significantly change the MCAE. Such MCAE changes is clearly observed at ΔMCA(k) (Fig. 4.18(b)).

For the second topic, we systematically investigated the SMAE in ferromagnetic (FM) slabs of Fe, Fe/MgO and antiferromagnetic (AFM) slab of MnX L1$_0$ structure (X: Pt, Ir, Pd, Ni). In the case of FM Fe slab or Fe/MgO interface, there is a reduction of E_{CA} compared to the E_{DA} and E_{SDA}. This reduction originates from quadrupole component of Fe at the surface/the interface Fe. Such quadrupole component showed a prolate shape (Fig. 4.21). On the other hand, in the case of AFM slab of MnX (X: Pt, Ir, Pd, Ni), the quadrupole component of Mn at surface contribute to the enhancement of SMAE. The difference between E_{DA} and E_{SDA} originating from the quadrupole component on Mn atom inside the layer (Fig. 4.23). Furthermore, the bulk property of SMAE estimated from the slope of the fitted line of E_{SDA} result has a good agreement with the SDA calculation of bulk structure (Table. 4.11).

5.2 Outlook

The effects of alloying, strain, and electric feld to the magnetic anisotropy energy (MAE) have been calculated and discussed in this thesis. We showed that alloying and strain can make a large impact to promote the perpendicular (PMAE). However, for the EF coefficient (γ), it is still far from the requirement in the real application. We systematically analyzed the mechanism of EF induces MAE by taking the advantage of the current approach based on the grand canonical force theorem (GCFT). In the GCFT scheme, we can clarify the possible origin in terms of the details of the electronic structure. The atomic k-resolved MCAE showed that EF only can modify the interface metal/oxide. But, in this work, we show the interface electronic structure can be changed by introducing the alloying in the underlayer region. In the future, alloying with a heavy element which has large spin-orbit coupling may be effective to enhance γ value [46, 98]. In addition, in the basis of GCFT method, other emerging phenomena at FM/oxide interface such as Rasbha effect is possible to investigated. Rasbha effect at the interface is responsible for generating effective field for the magnetization switching in STT-MRAM device [99, 100] and spin-to-charge conversion [101].

Recently, many reports show that antiferromagnetic (AFM) materials have great potential for the next generation of spintronic applications [96, 102, 103]. Within our current SDFT, we was able to evaluate the MAE in the AFM elements, then, as an emerging one, there may be a combination with AFM whose MAE can be controlled by external perturbation such as strain [104], electric field [51, 95, 105], and magnetic field [106].

Appendix A

Appendix Atom k-resolved MCAE

A.1 Atom k-resolved MCAE in structure-I

Atom k-resolved for structure-I are shown in Fig. A.1.
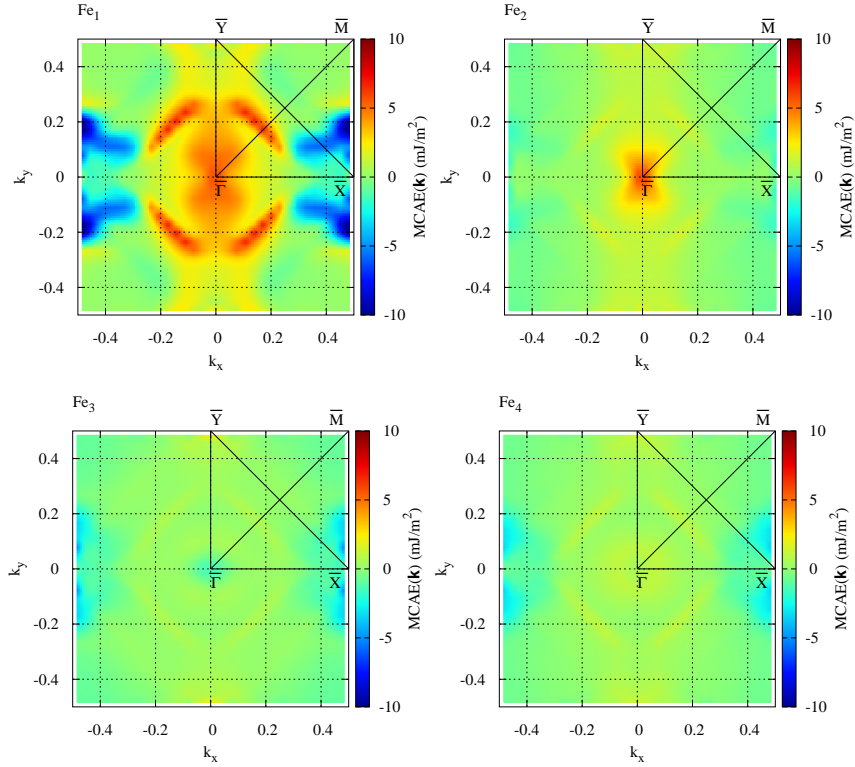
FIGURE A.1: Atomic k-resolved MCAE in structure-I at zero electric field.

A.2 Atom k-resolved MCAE in system-A

Atom k-resolved for system-A are shown in Fig. A.2.
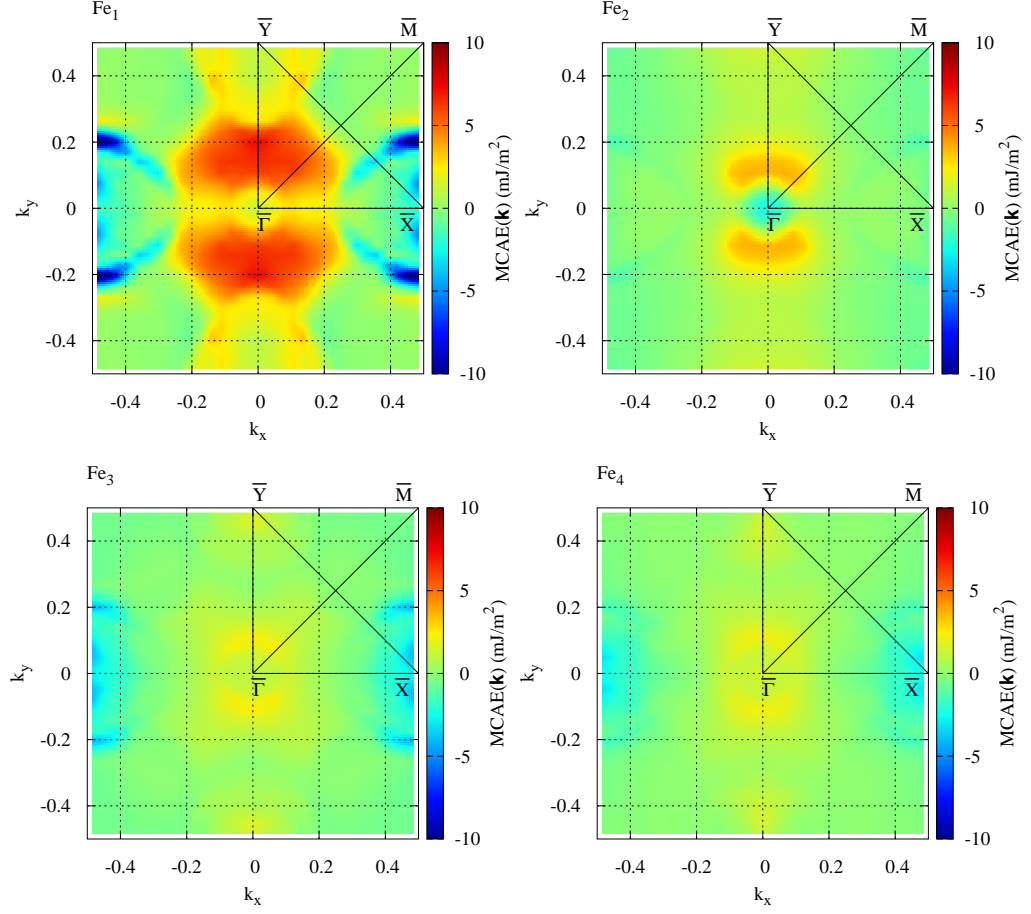
FIGURE A.2: Atomic k-resolved MCAE in system-A at zero electric field.

A.3 Atom *k*-resolved MCAE in system-B

Atom *k*-resolved for system-B are shown in Fig. A.3.
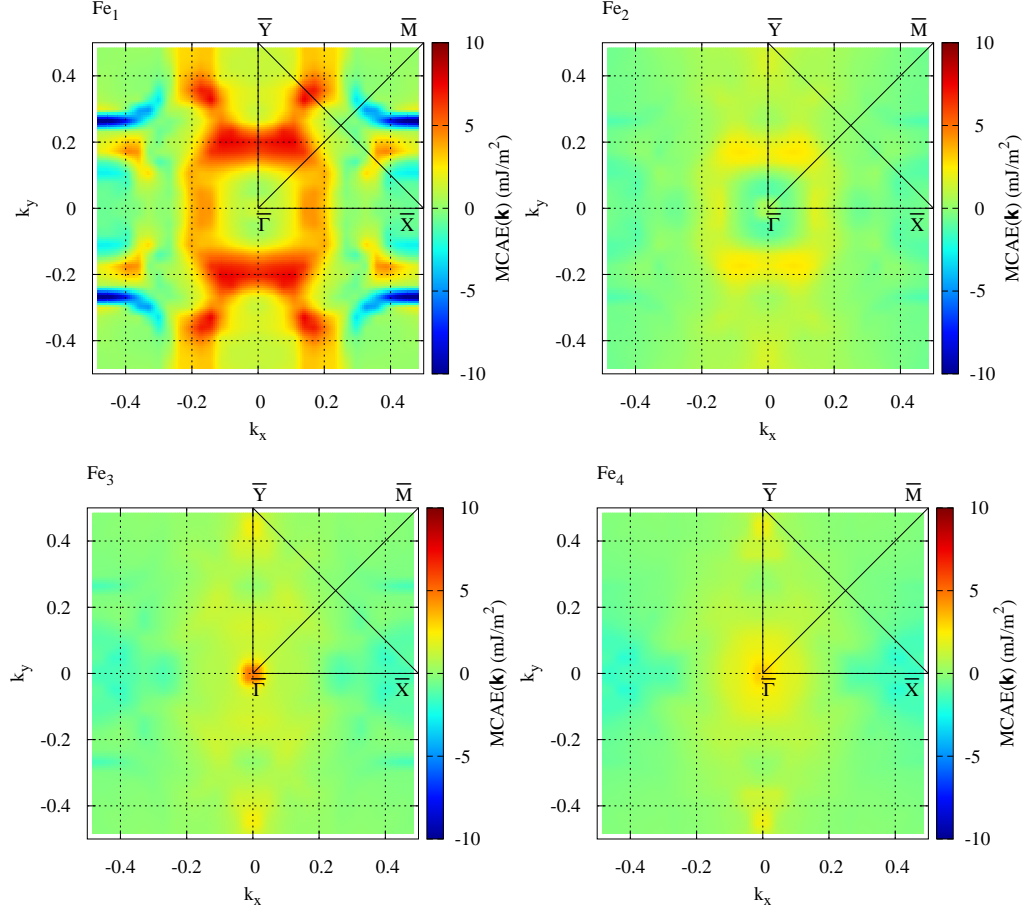
FIGURE A.3: Atomic *k*-resolved MCAE in system-B at zero electric field.

A.4 Atom k-resolved MCAE in system-B for $\eta_{\mathrm{Fe}}=-7\%$

Atom k-resolved in system-B for $\eta_{\mathrm{Fe}}=-7\%$ are shown in Fig. A.5.
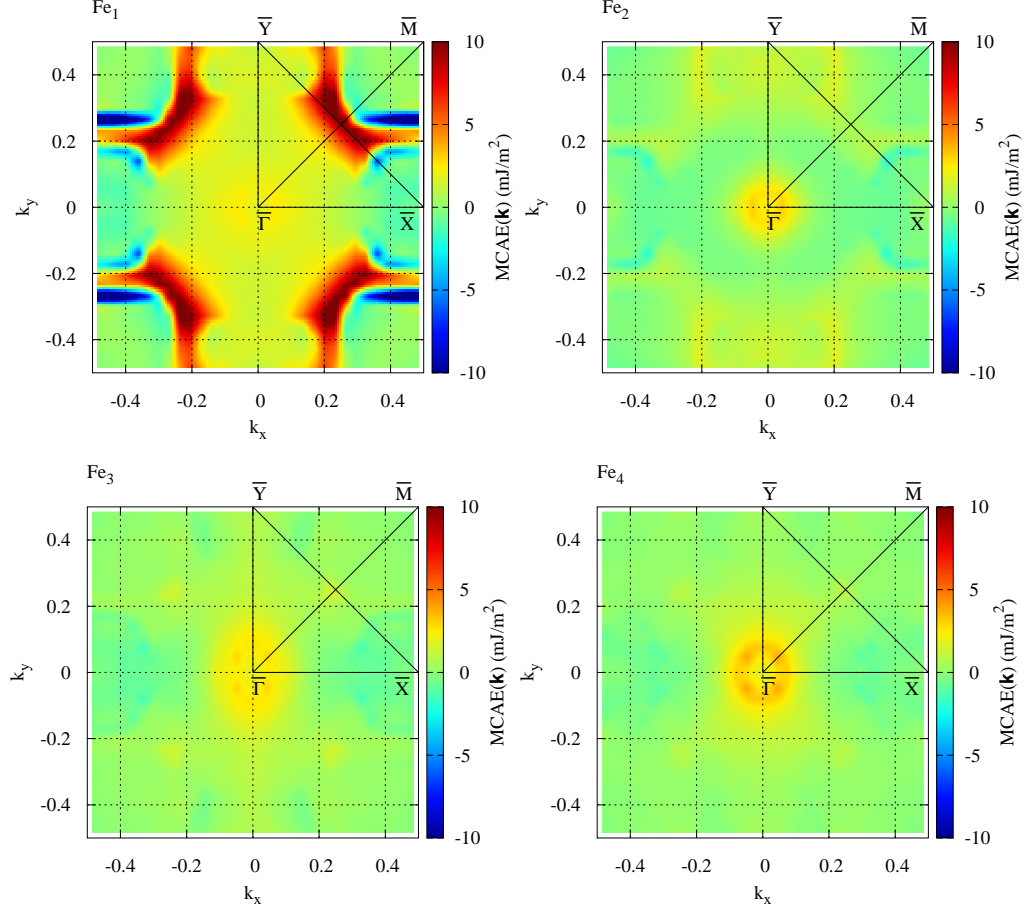
FIGURE A.4: Atom k-resolved MCAE in system-B at zero electric field for $\eta_{\mathrm{Fe}}=-7\%$.

A.5 PBAND as Strain Dependence

Partial band dispersions curve of Fe_1 for minority spin states in system-B as strain dependence are shown in Fig. A.5.
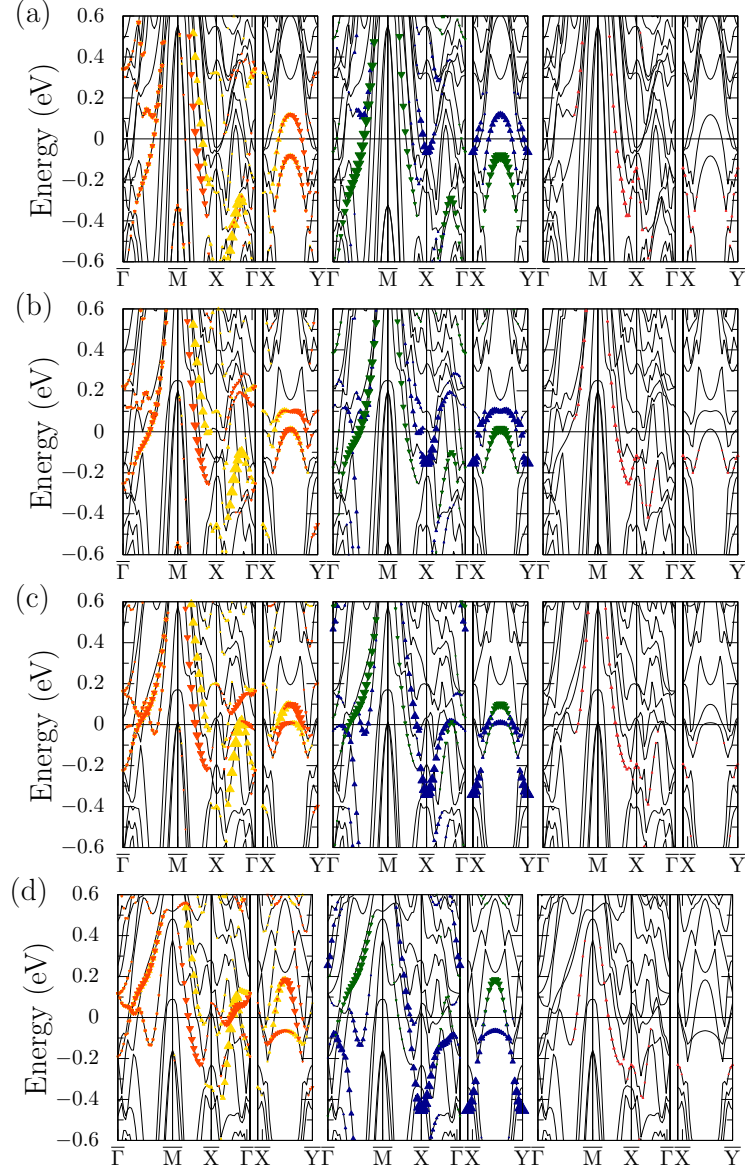
FIGURE A.5: Partial band dispersions curve of Fe_1 for minority spin states in system-B. (a) $\eta_{Fe}=-7\%$, (b) $\eta_{Fe}=-2.1\%$ and (c) $\eta_{Fe}=0.7\%$, and (d) $\eta_{Fe}=3.8\%$, respectively. The predominant components of Fe $3d$ orbitals d_{xz}, d_{yz}, $d_{x^2-y^2}$, and d_{xy} are marked as, orange-red filled triangles, gold filled circles, dark-green filled triangles, and dark-blue circles, respectively.

Bibliography

[1] A.R. Mackintosh and O.K. Andersen. The electronic structure of the transition metals, in: M. springford (ed.), electrons at the fermi surface. pages 149–224, 1980.

[2] T. Nozaki, A. Kozioł-Rachwał, W. Skowroński, V. Zayets, Y. Shiota, S. Tamaru, H. Kubota, A. Fukushima, S. Yuasa, and Y. Suzuki. Large voltage-induced changes in the perpendicular magnetic anisotropy of an mgo-based tunnel junction with an ultrathin fe layer. *Phys. Rev. Applied*, 5: 044006, Apr 2016.

[3] E. Abate and M. Asdente. Tight-binding calculation of $3d$ bands of fe with and without spin-orbit coupling. *Phys. Rev.*, 140:A1303–A1308, Nov 1965.

[4] H. Takayama, Klaus-Peter Bohnen, and Peter Fulde. Magnetic surface anisotropy of transition metals. *Phys. Rev. B*, 14:2287–2295, Sep 1976.

[5] J. A.C. Bland and B. Heinrich. *Ultrathin magnetic structures I: An introduction to the electronic, magnetic and structural properties.* 2005.

[6] M. N. Baibich, J. M. Broto, A. Fert, F. Nguyen Van Dau, F. Petroff, P. Etienne, G. Creuzet, A. Friederich, and J. Chazelas. Giant magnetoresistance of (001)fe/(001)cr magnetic superlattices. *Phys. Rev. Lett.*, 61:2472–2475, Nov 1988.

[7] G. Binasch, P. Grünberg, F. Saurenbach, and W. Zinn. Enhanced magnetoresistance in layered magnetic structures with antiferromagnetic interlayer exchange. *Phys. Rev. B*, 39:4828–4830, Mar 1989.

[8] C. Chappert, A. Fert, and F. N. Van Dau. The emergence of spin electronics in data storage. *Nature Materials*, 6(11):813–823, 2007.

[9] D. A. Thompson and J. S. Best. The future of magnetic data storage techology. *IBM Journal of Research and Development*, 44(3):311–322, 2010.

[10] B. Dieny and M. Chshiev. Perpendicular magnetic anisotropy at transition metal/oxide interfaces and applications. *Rev. Mod. Phys.*, 89:025008, Jun 2017.

[11] T. Miyazaki and N. Tezuka. Giant Magnetic Tunneling Effect in Fe/Al$_2$O$_3$/Fe Junction. *Journal of Magnetism and Magnetic Materials*, 139: L231–L234, 1995.

[12] J. S. Moodera, Lisa R. Kinder, Terrilyn M. Wong, and R. Meservey. Large magnetoresistance at room temperature in ferromagnetic thin film tunnel junctions. *Phys. Rev. Lett.*, 74:3273–3276, Apr 1995.

[13] M Julliere. Tunneling between ferromagnetic films. *Physics Letters*, 54(3): 225–226, 1975.

[14] W. H. Butler, X.-G. Zhang, T. C. Schulthess, and J. M. MacLaren. Spin-dependent tunneling conductance of fe|mgo|fe sandwiches. *Phys. Rev. B*, 63: 054416, Jan 2001.

[15] J. Mathon and A. Umerski. Theory of tunneling magnetoresistance of an epitaxial fe/mgo/fe(001) junction. *Phys. Rev. B*, 63:220403, May 2001.

[16] S. S. P. Parkin, C. Kaiser, A. Panchula, P. M. Rice, B. Hughes, M. Samant, and S. H. Yang. Giant tunnelling magnetoresistance at room temperature with MgO (100) tunnel barriers. *Nature Materials*, 3(12):862–867, 2004.

[17] S. Yuasa, T. Nagahama, A. Fukushima, Y. Suzuki, and K. Ando. Giant room-temperature magnetoresistance in single-crystal Fe/MgO/Fe magnetic tunnel junctions. *Nature Materials*, 3(12):868–871, 2004.

[18] S. Mangin, D. Ravelosona, J. A. Katine, and E. E. Fullerton. Current-induced magnetization reversal in nanopillars with perpendicular anisotropy. *Nature Materials*, 5(March):5–5, 2006.

[19] A. Brataas, A. D. Kent, and H. Ohno. Current-induced torques in magnetic materials. *Nature Materials*, 11(5):372–381, 2012.

[20] J. S. Meena, S. M. Sze, U. Chand, and T. Y. Tseng. Overview of emerging nonvolatile memory technologies. *Nanoscale Research Letters*, 9(1):1–33, 2014.

[21] S. Bhatti, R. Sbiaa, A. Hirohata, H. Ohno, S. Fukami, and S. N. Piramanayagam. Spintronics based random access memory: a review. *Materials Today*, 20(9):530–548, 2017.

[22] L. Liu, T. Moriyama, D. C. Ralph, and R. A. Buhrman. Spin-torque ferromagnetic resonance induced by the spin hall effect. *Phys. Rev. Lett.*, 106: 036601, Jan 2011.

[23] I. M. Miron, K. Garello, G. Gaudin, P. J. Zermatten, M. V. Costache, S. Auffret, S. Bandiera, A. Rodmacq, B.and Schuhl, and P. Gambardella. Perpendicular switching of a single ferromagnetic layer induced by in-plane current injection. *Nature*, 476(7359):189–193, 2011.

[24] V. E. Demidov, S. Urazhdin, H. Ulrichs, V. Tiberkevich, A. Slavin, D. Baither, G. Schmitz, and S. O. Demokritov. Magnetic nano-oscillator driven by pure spin current. *Nature Materials*, 11(12):1028–1031, 2012.

[25] L. Liu, C. Pai, Y Li, H W Tseng, D C Ralph, and R A Buhrman. Spin-torque switching with the giant spin Hall effect of tantalum. *Science (New York, N.Y.)*, 555(May):555–559, 2012.

[26] Y. Fan, P. Upadhyaya, X. Kou, M. Lang, S. Takei, Z. Wang, J. Tang, L. He, L. T. Chang, M. Montazeri, G. Yu, W. Jiang, T. Nie, R. N. Schwartz, Y. Tserkovnyak, and K. L. Wang. Magnetization switching through giant spin-orbit torque in a magnetically doped topological insulator heterostructure. *Nature Materials*, 13(7):699–704, 2014.

[27] S. Fukami, C. Zhang, S. Duttagupta, A. Kurenkov, and H. Ohno. Magnetization switching by spin-orbit torque in an antiferromagnet-ferromagnet bilayer system. *Nature Materials*, 15(5):535–541, 2016.

[28] S. Fukami, T. Anekawa, C. Zhang, and H. Ohno. A spin-orbit torque switching scheme with collinear magnetic easy axis and current configuration. *Nature Nanotechnology*, 11(7):621–625, 2016.

[29] H. Ohno, D. Chiba, F. Matsukura, T. Omiya, E. Abe, T. Dietl, Y. Ohno, and K. Ohtani. Electric-field control of ferromagnetism. *Nature*, 408(6815): 944–946, 2000.

[30] D Chiba, M Yamanouchi, F Matsukura, and H Ohno. Electrical Manipulation of Magnetization Reversal in a. *Science*, 301(August):943–945, 2003.

[31] M. Weisheit, S. Fähler, A. Marty, Y. Souche, C. Poinsignon, and D. Givord. Electric field-induced modification of magnetism in thin-film ferromagnets. *Science*, 315(5810):349–351, 2007.

[32] T. Maruyama, Y. Shiota, T. Nozaki, K. Ohta, N. Toda, M. Mizuguchi, A. A. Tulapurkar, T. Shinjo, M. Shiraishi, S. Mizukami, Y. Ando, and Y. Suzuki. Large voltage-induced magnetic anisotropy change in a few atomic layers of iron. *Nature Nanotechnology*, 4(3):158–161, 2009.

[33] T. Nozaki, Y. Shiota, M. Shiraishi, T. Shinjo, and Y. Suzuki. Voltage-induced perpendicular magnetic anisotropy change in magnetic tunnel junctions. *Applied Physics Letters*, 96(2), 2010.

[34] Y. Shiota, S. Murakami, F. Bonell, T. Nozaki, T. Shinjo, and Y. Suzuki. Quantitative evaluation of voltage-induced magnetic anisotropy change by magnetoresistance measurement. *Applied Physics Express*, 4(4):2–5, 2011.

[35] Yoichi Shiota, Takayuki Nozaki, Frédéric Bonell, Shinichi Murakami, Teruya Shinjo, and Yoshishige Suzuki. Induction of coherent magnetization switching in a few atomic layers of FeCo using voltage pulses. *Nature Materials*, 11(1):39–43, 2012.

[36] T. Nozaki, Y. Shiota, S. Miwa, S. Murakami, F. Bonell, S. Ishibashi, H. Kubota, K. Yakushiji, T. Saruya, A. Fukushima, S. Yuasa, T. Shinjo, and Y. Suzuki. Electric-field-induced ferromagnetic resonance excitation in an ultrathin ferromagnetic metal layer. *Nature Physics*, 8(6):491–496, 2012.

[37] W. G. Wang, M. Li, S. Hageman, and C. L. Chien. Electric-field-assisted switching in magnetic tunneljunctions. *Nature Materials*, 11(1):64–68, 2012.

[38] S. Kanai, M. Yamanouchi, S. Ikeda, Y. Nakatani, F. Matsukura, and H. Ohno. Electric field-induced magnetization reversal in a perpendicular-anisotropy CoFeB-MgO magnetic tunnel junction. *Applied Physics Letters*, 101(12):2010–2013, 2012.

[39] C. Duan, J. P. Velev, R. F. Sabirianov, Z. Zhu, J. Chu, S. S. Jaswal, and E. Y. Tsymbal. Surface magnetoelectric effect in ferromagnetic metal films. *Phys. Rev. Lett.*, 101:137201, Sep 2008.

[40] K. Nakamura, R. Shimabukuro, Y. Fujiwara, T. Akiyama, T. Ito, and A. J. Freeman. Giant modification of the magnetocrystalline anisotropy in transition-metal monolayers by an external electric field. *Phys. Rev. Lett.*, 102:187201, May 2009.

[41] M. Tsujikawa and T. Oda. Finite electric field effects in the large perpendicular magnetic anisotropy surface Pt/Fe/Pt(001): A first-principles study. *Phys. Rev. Lett.*, 102:247203, Jun 2009.

[42] L. Xu and S. Zhang. Electric field control of interface magnetic anisotropy. *Journal of Applied Physics*, 111(7):2012–2015, 2012.

[43] S. E. Barnes, J. Ieda, and S. Maekawa. Rashba Spin-Orbit Anisotropy and the Electric Field Control of Magnetism. *Scientific Reports*, 4:1–5, 2014.

[44] F. Ibrahim, H. X. Yang, A. Hallal, B. Dieny, and M. Chshiev. Anatomy of electric field control of perpendicular magnetic anisotropy at Fe/MgO interfaces. *Physical Review B*, 93(1):1–5, 2016.

[45] T. Nozaki, A. Kozioł-Rachwał, M. Tsujikawa, Y. Shiota, X. Xu, T. Ohkubo, T. Tsukahara, S. Miwa, M. Suzuki, S. Tamaru, H. Kubota, A. Fukushima, K. Hono, M. Shirai, Y. Suzuki, and S. Yuasa. Underlayer material influence on electric-field controlled perpendicular magnetic anisotropy in CoFeB/MgO magnetic tunnel junctions. *Npg Asia Materials*, 9, 2017.

[46] W. Skowroński, T. Nozaki, D. D. Lam, Y. Shiota, K. Yakushiji, H. Kubota, A. Fukushima, S. Yuasa, and Y. Suzuki. Underlayer material influence on electric-field controlled perpendicular magnetic anisotropy in CoFeB/MgO magnetic tunnel junctions. *Physical Review B - Condensed Matter and Materials Physics*, 91(18):1–6, 2015.

[47] S. Miwa, J. Fujimoto, P. Risius, K. Nawaoka, M. Goto, and Y. Suzuki. Strong bias effect on Voltage-driven torque at epitaxial Fe-MgO interface. *Physical Review X*, 7(3):1–9, 2017.

[48] P. V. Ong, N. Kioussis, D. Odkhuu, A. P. Khalili, K. L. Wang, and G. P. Carman. Giant voltage modulation of magnetic anisotropy in strained heavy metal/magnet/insulator heterostructures. *Phys. Rev. B*, 92:020407, Jul 2015.

[49] K. Yushi, Hiroaki. Y., S. Yoshiak, O. Soichi, F Keiko, Y. Masahiko, K. Katsuhiko, S. Hideyuki, I. Mizue, I. Tomoaki, S. Naoharu, S. Mariko, S. Satoshi, A. Buyandalai, O. Yuichi, I. Kazutaka, T. Ajay, and K. Atsushim. Giant voltage-controlled magnetic anisotropy effect in a crystallographically strained CoFe system. *Applied Physics Express*, 11(5):053007, apr 2018.

[50] S. Miwa, M. Suzuki, M. Tsujikawa, K. Matsuda, T. Nozaki, K. Tanaka, T. Tsukahara, K. Nawaoka, M. Goto, Y. Kotani, T. Ohkubo, F. Bonell, E. Tamura, K. Hono, T. Nakamura, M. Shirai, S. Yuasa, and Y. Suzuki. Voltage controlled interfacial magnetism through platinum orbits. *Nature Communications*, 8(May), 2017.

[51] G. Minori, N Kohei, M Shinji, H. Shohei, M. Norikazu, and Yoshishige. S. Electric field modulation of tunneling anisotropic magnetoresistance in tunnel junctions with antiferromagnetic electrodes. *Japanese Journal of Applied Physics*, 55(8):080304, 2016.

[52] Y. Wang, X. Zhou, C. Song, Y. Yan, S. Zhou, G. Wang, C. Chen, F. Zeng, and F. Pan. Electrical control of the exchange spring in antiferromagnetic metals. *Advanced Materials*, 27(20):3196–3201, 2015.

[53] S. Loth, S. Baumann, C. P. Lutz, D. M. Eigler, and A. J. Heinrich. Bistability in atomic-scale antiferromagnets. *Science*, 335(6065):196–199, 2012. ISSN 0036-8075.

[54] H. Brooks. Ferromagnetic anisotropy and the itinerant electron model. *Phys. Rev.*, 58:909–918, Nov 1940.

[55] E I Kondorskii and E Straube. Magnetic anisotropy of nickel. *Journal of Experimental and Theoretical Physics*, 63(1):188–193, 1973.

[56] P. Bruno. Tight-binding approach to the orbital magnetic moment and magnetocrystalline anisotropy of transition-metal monolayers. *Phys. Rev. B*, 39:865–868, Jan 1989.

[57] D. Wang, R. Wu, and A. J. Freeman. First-principles theory of surface magnetocrystalline anisotropy and the diatomic-pair model. *Phys. Rev. B*, 47:14932–14947, Jun 1993.

[58] W. Kohn and L. J. Sham. Self-consistent equations including exchange and correlation effects. *Phys. Rev.*, 140:A1133–A1138, Nov 1965.

[59] P. Hohenberg and W. Kohn. Inhomogeneous electron gas. *Phys. Rev.*, 136: B864–B871, Nov 1964.

[60] D. M. Ceperley and B. J. Alder. Ground state of the electron gas by a stochastic method. *Phys. Rev. Lett.*, 45:566–569, Aug 1980.

[61] J. P. Perdew and Alex Zunger. Self-interaction correction to density-functional approximations for many-electron systems. *Phys. Rev. B*, 23: 5048–5079, May 1981.

[62] M. A. Korotin, V. I. Anisimov, D. I. Khomskii, and G. A. Sawatzky. CrO 2 : A self-doped double exchange ferromagnet. *Physical Review Letters*, 80 (19):4305–4308, 1998. ISSN 10797114. doi: 10.1103/PhysRevLett.80.4305.

[63] J. P. Perdew and Y. Wang. Accurate and simple analytic representation of the electron-gas correlation energy. *Phys. Rev. B*, 45:13244–13249, Jun 1992.

[64] J. P. Perdew, K. Burke, and M. Ernzerhof. Generalized gradient approximation made simple. *Phys. Rev. Lett.*, 77:3865–3868, Oct 1996.

[65] F. Tran, R. Laskowski, P. Blaha, and K. Schwarz. Performance on molecules, surfaces, and solids of the wu-cohen gga exchange-correlation energy functional. *Phys. Rev. B*, 75:115131, Mar 2007.

[66] V. Ozoliņš and M. Körling. Full-potential calculations using the generalized gradient approximation: Structural properties of transition metals. *Phys. Rev. B*, 48:18304–18307, Dec 1993.

[67] P. Bagno, O. Jepsen, and O. Gunnarsson. Ground-state properties of third-row elements with nonlocal density functionals. *Phys. Rev. B*, 40:1997–2000, Jul 1989.

[68] P. Haas, F. Tran, and P. Blaha. Calculation of the lattice constant of solids with semilocal functionals. *Phys. Rev. B*, 79:085104, Feb 2009.

[69] T. Oda, A. Pasquarello, and R. Car. Fully Unconstrained Approach to Noncollinear Magnetism: Application to Small Fe Clusters. *Physical Review Letters*, 80(16):3622–3625, 1998.

[70] K. Laasonen, A. Pasquarello, R. Car, C. Lee, and D. Vanderbilt. Carparrinello molecular dynamics with vanderbilt ultrasoft pseudopotentials. *Phys. Rev. B*, 47:10142–10153, Apr 1993.

[71] T. Oda and A. Hosokawa. Fully relativistic two-component-spinor approach in the ultrasoft-pseudopotential plane-wave method. *Phys. Rev. B*, 72: 224428, Dec 2005.

[72] J. P. Perdew, J. A. Chevary, S. H. Vosko, Koblar A. Jackson, Mark R. Pederson, D. J. Singh, and Carlos Fiolhais. Atoms, molecules, solids, and surfaces: Applications of the generalized gradient approximation for exchange and correlation. *Phys. Rev. B*, 46:6671–6687, Sep 1992.

[73] G. Theurich and N. A. Hill. Self-consistent treatment of spin-orbit coupling in solids using relativistic fully separable ab initio pseudopotentials. *Phys. Rev. B*, 64:073106, Jul 2001.

[74] A. D. Corso and A. M. Conte. Spin-orbit coupling with ultrasoft pseudopotentials: Application to au and pt. *Phys. Rev. B*, 71:115106, Mar 2005.

[75] U. von Barth and L. Hedin. A local exchange-correlation potential for the spin polarized case. *Journal of Physics C: Solid State Physics*, 5(13):1629–1642, jul 1972.

[76] G. H. O. Daalderop, P. J. Kelly, and M. F. H. Schuurmans. First-principles calculation of the magnetocrystalline anisotropy energy of iron, cobalt, and nickel. *Phys. Rev. B*, 41:11919–11937, Jun 1990.

[77] D. Li, A.r Smogunov, C. Barreteau, F. Ducastelle, and D. Spanjaard. Magnetocrystalline anisotropy energy of Fe(001) and Fe(110) slabs and nanoclusters: A detailed local analysis within a tight-binding model. *Phys. Rev. B*, 88:214413, Dec 2013.

[78] P. Bruno. Lecture notes of iff ferienkurs magnetismus von festkörpern und grenzächen, ed. p. h. dederichs, p. grünberg, and w. zinn (jülich. 24:24.1, 1993.

[79] T. Oda and M. Obata. Implementation of magnetic dipole interaction in the planewave-basis approach for slab systems. *Journal of the Physical Society of Japan*, 87(6):064803, 2018.

[80] H. J G Draaisma and W. J M De Jonge. Surface and volume anisotropy from dipole-dipole interactions in ultrathin ferromagnetic films. *Journal of Applied Physics*, 64(7):3610–3613, 1988.

[81] M. Otani and O. Sugino. First-principles calculations of charged surfaces and interfaces: A plane-wave nonrepeated slab approach. *Physical Review B - Condensed Matter and Materials Physics*, 73(11):1–11, 2006.

[82] M. Tsujikawa and T. Oda. Electronic structure and magnetic anisotropy of a constrained Fe chain in an electric field. *Journal of Physics Condensed Matter*, 21(6), 2009.

[83] S. Haraguchi, M. Tsujikawa, J. Gotou, and T. Oda. Electric-field effects on magnetic anisotropy in Pd/Fe/Pd(0 0 1) surface. *Journal of Physics D: Applied Physics*, 44(6):0–8, 2011.

[84] P. V. Ong, N Kioussis, P. Khalili Amiri, and K. L. Wang. Electric-field-driven magnetization switching and nonlinear magnetoelasticity in Au/FeCo/MgO heterostructures. *Scientific Reports*, 6(April):1–8, 2016.

[85] A. Kozioł-Rachwał, T. Nozaki, K. Freindl, J. Korecki, S. Yuasa, and Y. Suzuki. Enhancement of perpendicular magnetic anisotropy and its electric field-induced change through interface engineering in Cr/Fe/MgO. *Scientific Reports*, 7(1):1–3, 2017.

[86] Indra Pardede, Tomosato Kanagawa, Nurul Ikhsan, Itsuki Murata, Daiki Yoshikawa, Masao Obata, and Tatsuki Oda. A comprehensive study of sign change in electric field control perpendicular magnetic anisotropy energy at Fe/MgO Interface: First principles calculation. *IEEE Transactions on Magnetics*, 55(2):1–4, 2019. ISSN 00189464. doi: 10.1109/TMAG.2018. 2860581.

[87] D. Yoshikawa, M. Obata, Y. Taguchi, S. Haraguchi, and T. Oda. Possible origin of nonlinear magnetic anisotropy variation in electric field effect in a double interface system. *Applied Physics Express*, 7(11):113005, 2014.

[88] N. Ikhsan, T. Kanagawa, I. Pardede, D. Yoshikawa, M. Obata, and T. Oda. Perpendicular and in-plane magnetic anisotropies in Cr-buffered Fe(x)/MgO interface from first-principles approach. *Scince Reports of Kanazawa University*, 62:23–35, 2018.

[89] S. Zhang. Spin-dependent surface screening in ferromagnets and magnetic tunnel junctions. *Phys. Rev. Lett.*, 83:640–643, Jul 1999.

[90] R. Shimabukuro, K. Nakamura, T. Akiyama, and T. Ito. Electric field effects on magnetocrystalline anisotropy in ferromagnetic Fe monolayers. *Physica E: Low-Dimensional Systems and Nanostructures*, 42(4):1014–1017, 2010.

[91] A. Hallal, H. X. Yang, B. Dieny, and M. Chshiev. Anatomy of perpendicular magnetic anisotropy in fe/mgo magnetic tunnel junctions: First-principles insight. *Phys. Rev. B*, 88:184423, Nov 2013.

[92] M. Ogura, H. Akai, and J. Kanamori. Enhancement of magnetism of Fe by Cr and V. *Journal of the Physical Society of Japan*, 80(10):1–6, 2011.

[93] Y. Shiota, F. Bonell, S. Miwa, N. Mizuochi, T. Shinjo, and Y. Suzuki. Opposite signs of voltage-induced perpendicular magnetic anisotropy change in CoFeB|MgO junctions with different underlayers. *Applied Physics Letters*, 103(8), 2013.

[94] M. Gottwald, S. Andrieu, F. Gimbert, E. Shipton, L. Calmels, C. Magen, E. Snoeck, M. Liberati, T. Hauet, E. Arenholz, S. Mangin, and E. E. Fullerton. Co/Ni(111) superlattices studied by microscopy, x-ray absorption, and ab initio calculations. *Physical Review B - Condensed Matter and Materials Physics*, 86(1):1–15, 2012.

[95] N. Tomohiro, S. Yohei, K. Yukie, K. Yohei, I. Hiroshi, Muftah A., P. P. Satya, Y. Shujun, Y. Syougo, S. Tatsuo, and M. Masashi. Large perpendicular exchange bias and high blocking temperature in al-doped cr2o3/co thin film systems. *Applied Physics Express*, 10(7):073003, jun 2017.

[96] T. Jungwirth, X. Marti, P. Wadley, and J. Wunderlich. Antiferromagnetic spintronics. *Nature Nanotechnology*, 11(3):231–241, 2016.

[97] R. Y. Umetsu, A. Sakuma, and K. Fukamichi. Magnetic anisotropy energy of antiferromagnetic L10-type equiatomic Mn alloys. *Applied Physics Letters*, 89(5), 2006.

[98] J. Suwardy, K. Nawaoka, J. Cho, M. Goto, Y. Suzuki, and S. Miwa. Voltage-controlled magnetic anisotropy and voltage-induced Dzyaloshinskii-Moriya interaction change at the epitaxial Fe(001)/MgO(001) interface engineered by Co and Pd atomic-layer insertion. *Physical Review B*, 94(14):1–8, 2018.

[99] M. I. Miron, G. Gaudin, S. Auffret, B. Rodmacq, A. Schuhl, S. Pizzini, J. Vogel, and P. Gambardella. Current-driven spin torque induced by the Rashba effect in a ferromagnetic metal layer. *Nature Materials*, 9(3):230–234, 2010. ISSN 1476-4660. doi: 10.1038/nmat2613.

[100] Junyeon Kim, Jaivardhan Sinha, Masamitsu Hayashi, Michihiko Yamanouchi, Shunsuke Fukami, Tetsuhiro Suzuki, Seiji Mitani, and Hideo Ohno. Layer thickness dependence of the current-induced effective field vector in Ta|CoFeB|MgO. *Nature Materials*, 12(3):240–245, 2013. ISSN 14761122. doi: 10.1038/nmat3522.

[101] E. Lesne, Yu Fu, S. Oyarzun, J. C. Rojas-Sánchez, D. C. Vaz, H. Naganuma, G. Sicoli, J. P. Attané, M. Jamet, E. Jacquet, J. M. George, A. Barthélémy, H. Jaffrès, A. Fert, M. Bibes, and L. Vila. Highly efficient and tunable spin-to-charge conversion through Rashba coupling at oxide interfaces. *Nature Materials*, 15(12):1261–1266, 2016. ISSN 14764660. doi: 10.1038/nmat4726.

[102] V. Baltz, A. Manchon, M. Tsoi, T. Moriyama, T. Ono, and Y. Tserkovnyak. Antiferromagnetic spintronics. *Rev. Mod. Phys.*, 90:015005, Feb 2018.

[103] Cheng Song, Yunfeng You, Xianzhe Chen, Xiaofeng Zhou, Yuyan Wang, and Feng Pan. How to manipulate magnetic states of antiferromagnets. *Nanotechnology*, 29(11):112001, mar 2018. doi: 10.1088/1361-6528/aaa812.

[104] Han Yan, Zexin Feng, Shunli Shang, Xiaoning Wang, Zexiang Hu, Jinhua Wang, Zengwei Zhu, Hui Wang, Zuhuang Chen, Hui Hua, Wenkuo Lu, Jingmin Wang, Peixin Qin, Huixin Guo, Xiaorong Zhou, Zhaoguogang Leng, Zikui Liu, Chengbao Jiang, Michael Coey, and Zhiqi Liu. A piezoelectric, strain-controlled antiferromagnetic memory insensitive to magnetic fields. *Nature Nanotechnology*, 14(2):131–136, 2019. ISSN 17483395. doi: 10.1038/s41565-018-0339-0.

[105] Tobias Kosub, Martin Kopte, Ruben Hühne, Patrick Appel, Brendan Shields, Patrick Maletinsky, René Hübner, Maciej Oskar Liedke, Jürgen

Fassbender, Oliver G. Schmidt, and Denys Makarov. Purely antiferromagnetic magnetoelectric random access memory. *Nature Communications*, 8: 1–7, 2017. ISSN 20411723. doi: 10.1038/ncomms13985.

[106] A. A. Sapozhnik, R. Abrudan, Yu Skourski, M. Jourdan, H. Zabel, M. Kläui, and H. J. Elmers. Manipulation of antiferromagnetic domain distribution in Mn2Au by ultrahigh magnetic fields and by strain. *Physica Status Solidi - Rapid Research Letters*, 11(4):9–12, 2017. ISSN 18626270. doi: 10.1002/pssr.201600438.

List of publications:

1. **I. Pardede**, T. Kanagawa, N. Ikhsan, D. Yoshikawa and M. Obata, and T. Oda, A comprehensive study of sign change in electric field control perpendicular magnetic anisotropy energy at Fe/MgO interface: first principles calculation, *IEEE Transaction on Magnetics* 55, 2, 1700104, August 2018. DOI: 10.1109/TMAG.2018.2860581.

2. T. Oda, **I. Pardede**, T. Kanagawa, N. Ikhsan, D. Yoshikawa, and M. Obata, Shape magnetic anisotropy from spin density in nano slab systems, *IEEE Transaction on Magnetics 55*, 2, 1300104, September 2018. DOI: 10.1109/T-MAG.2018.2868843.

3. N. Ikhsan, T. Kanagawa, **I. Pardede**, D. Yoshikawa, and T. Oda, Perpendicular and in-plane magnetic anisotropies in Cr-buffered Fe(x)/MgO interface from first-principles approach, *Sci. Rep. Kanazawa Univ.* Vol. 62. pp. 23-35, 2018.

4. N. Ikhsan, **I. Pardede**, T. Kanagawa, D. Yoshikawa, and T. Oda, Fermi level smearing effect in the perpendicular interface Fe/MgO magnetic anisotropy, *Sci. Rep. Kanazawa Univ.* Vol. 62. pp. 37-49, 2018

List of scientific presentation:

1. **I. Pardede**, T. Kanagawa, N. Ikhsan, I. Murata, D. Yoshikawa, M. Obata, and T. Oda, Anatomy of Large Perpendicular Magnetic Anisotropy Energy in Co/Ni (111) Multilayer, **The 66th Japan Society of Applied Physics (JSAP), Spring Meeting,** 2019 (March, 9-12, 2019) Tokyo Institute of Technology, Ookayama Campus (oral presentation, Presentation No. 10a-M101-2).

2. **I. Pardede**, T. Kanagawa, N. Ikhsan, D. Yoshikawa, M. Obata, and T. Oda, Perpendicular magnetic anisotropy in free standing Co/Ni (111) thin film, **Spin-RNJ 2019,** (February, 20, 2019) Institute for Material Research, Tohoku University (poster presentation, Presentation No. OSK-01).

3. **I. Pardede**, T. Kanagawa, N. Ikhsan, I. Murata, D. Yoshikawa, M. Obata, and T. Oda, A comprehensive Study of Sign Change in Electric Field Control Perpendicular Magnetic Anisotropy Energy at Fe/MgO Interface: First Principles Calculation, **21ST International Conference on Magnetism 2018 (ICM2018)** (July, 16-20, 2018) Moscone Center, San Francisco,USA (Poster presentation, N2-01).

4. **I. Pardede**, T. Kanagawa, N. Ikhsan, M. Obata, and T. Oda, Electric Field control magnetic anisotropy of Fe/MgO from first principles: Role of strain and strain engineering, **Physics and Applications of Spin-related in Semiconductors, (PASPS-22)** (December, 4-5, 2017) Osaka University Toyonaka campus SIGMA Hall, Japan (Poster presentation, P-37).

5. **I. Pardede**, T. Kanagawa, N. Ikhsan, M. Obata, and T. Oda, The Fe/Cr interchange induces sign change in voltage-control magnetic anisotropy, **The 28th Magnetic Recording Conference (TMRC 2017)**(August 2 - 4, 2017) Tsukuba International Congress Center (EPOCHAL TSUKUBA), Tsukuba, Japan (Poster presentation, DP23, 3th 2017).(2017/08/03).

6. **I. Pardede**, T. Kanagawa, N. Ikhsan, I. Murata, M. Obata, and T. Oda, Electric-field effects on perpendicular magnetic anisotropy in the strained Fe/MgO interface of V element underlayer, **International symposium on computational science 2017 (ISCS2017),** (July 27, 2017) Kanazawa University (Short presentation and Poster presentation) (Poster presentation, No.16).